UNIVERSITY OF FERRARA

MATHEMATICAL PHYSICAL AND NATURAL SCIENCES FACULTY

Research Doctorate in Physics

Course of studies: Atmospheric Physics

STUDY OF THE IMPACT OF MODELLING SEA SURFACE TEMPERATURE IN A MONTHLY ATMOSPHERIC ENSEMBLE PREDICTION SYSTEM

Research Doctorate Thesis of

Cristian Rendina

Tutors:

Prof. Federico Porcú

Dott. Andrea Buzzi

XXIV CYCLE

Università degli Studi di Ferrara

DOTTORATO DI RICERCA IN FISICA

CICLO XXIV

COORDINATORE Prof. Frontera Filippo

STUDY OF THE IMPACT OF MODELLING SEA SURFACE TEMPERATURE IN A MONTHLY ATMOSPHERIC ENSEMBLE PREDICTION SYSTEM

Settore Scientifico Disciplinare FIS/06

Dottorando

Dott. Rendina Cristian

Tutore interno

Prof. Porcù Federico

Tutore esterno

Dott. Buzzi Andrea

Anni 2009/2011

Ringraziamenti

Questo corso di dottorato è stato molto importante per la mia crescita personale e professionale. Desidero innanzitutto ringraziare la mia famiglia, per il supporto morale durante tutti questi anni di studio, soprattutto nei momenti di difficoltà. Poiché non sono molto portato a scrivere parole troppo dolci e smielate, mi limito a dire GRAZIE! a tutti coloro che mi hanno aiutato o contribuito alle mie ricerche. Grazie ad Andrea Buzzi, che mi ha sopportato ma anche spronato in qualità di mio tutore, aiutandomi con consigli preziosi. Grazie anche al mio tutore "ufficiale" Federico Porcù per il suo aiuto. Grazie ai referees Valentina Pavan ed Ennio Tosi, per i loro utili commenti riguardo l'elaborazione della tesi. Grazie a Piero Malguzzi, Oxana Drofa e Daniele Mastrangelo che mi hanno aiutato a lavorare con il modello GLOBO e l'elaborazione grafica dei risultati. Grazie anche a tutti i ricercatori con cui ho avuto piacevoli conversazioni e discussioni sia per quanto riguarda gli argomenti trattati in questa tesi, sia per divertimento e intrattenimento in tutti questi anni. In particolare ringrazio Frederic Vitart, Paola Cessi, Susanna Corti, Laura Ferranti, Anna Trevisan, Felicita Russo e tutti coloro che ho conosciuto durante la mia permanenza all'istituto ISAC. Infine grazie anche all'ISAC-CNR di Bologna per avermi messo a disposizione i mezzi necessari a condurre le mie ricerche e all'università di Ferrara per avermi dato l'opportunità di seguire questo corso di dottorato. Questo lavoro è stato realizzato grazie al supporto economico del progetto ASI "Protezione civile dalle alluvioni: il nowcasting - PROSA" e del progetto "Intesa Operativa tra il Dipartimento della Protezione Civile Nazionale e il CNR-ISAC".

Contents

Introduction

The chaotic nature of the climate system was recognized first by Lorenz (1969, 1975). As mentioned in Giorgi (2005), he defined two types of predictability problems:

1) Predictability of the first kind, which is a problem related to the prediction of the evolution of the atmosphere or the climate system knowing its initial state. It is an initial value problem, and numerical weather prediction constitutes a typical example. Lorenz found that the theoretical limit of predictability for numerical weather prediction is about fifteen days.

2) Predictability of the second kind, which is related to a boundary value problem, since it deals with the evolution of the statistical properties of the climate system in response to changes in external forcings. An example is the seasonal forecast, in which the probability distributions of the mean fields values or of the anomalies with respect to the climatology are predicted.

Monthly forecast is part of extended–range prediction systems directed to predict the atmospheric circulation in the time range from a week to a month. Therefore it is somewhere between the predictability of the first and the second kind. Several attemps of extended-range forecasting up to one month have been made in the past. They showed some moderate skill for the forecast beyond day ten compared to climatology (Miyakoda et al., 1983, 1986). Many of the world's operational prediction centres started to produce different experiments on extended-range forecasting, even if there were studies stating that it was difficult to

beat the persistence of medium-range operational forecasts (Molteni et al., 1986) and that apparent good results in extended range forecasts could just occur by chance (Anderson and Van den Dool, 1994). However the predictive skill of the monthly forecasting was found to be dependent on the geographical area. Newman et al. (2003) found some strong predictability in week 2 and week 3 averages in some regions of the Northern Hemisphere.

Most of the national meteorological/climatic centres apply numerical weather prediction systems that produce "medium range" forecasts up to 10-15 days. There are also well developed seasonal prediction systems, that produce forecasts in probabilistic terms up to the next 3-6 months. However, the operational monthly forecasting, intermediate between the medium-range and the seasonal forecasting, is not so diffused. Only recently monthly forecasting systems have been developed in some national and international centres: the European Centre for Medium-Range Forecast (ECMWF, UK), the National Centers for Enviromental Prediction (NCEP,USA), the Japan Meteorological Agency (JMA, Japan), the Bureau of Meteorology (BOM, Australia), and a few more.

A skillfull prediction of atmospheric circulation patterns beyond the first ten days would be very useful for many application, including civil protection services (fires, draughts, floods), agricultural purposes and other economical activities. The main reason of this late diffusion of the monthly forecasting relies on the fact that it is due to a combination of initial condition and boundary condition problems. A time scale of 30-40 days is too long for the atmosphere to keep internal memory of the initial state, while probably it is too short for the boundary conditions forcings (mainly the sea surface temperature) to have a strong impact on the atmospheric circulation. The monthly prediction is thus a forecast of a "mixed" kind. It predicts the circulation anomalies with respect to the climatology on time scales from a week to a month in a statistical sense (eg. ranked probabilities).

Different modelling solutions are adopted to produce monthly forecasts: coupled

atmosphere–ocean general circulation models (Vitart, 2004; Vitart et al., 2008; Hudson et al., 2011a,b; Saha et al., 2011) and atmosphere–only models, in which SST is either already predicted by means of statistical or dynamical models (called 2-Tier systems, at Korea Meteorological Administration and Beijing Climate Centre) or simulated coupling with simple slab mixed layer models (ISAC-CNR). Other centres use purely statistical models based on various atmospheric and oceanic indices to issue monthly predictions (Pasqui et al., 2007).

Generally, the ensemble technique is applied to the numerical modelling solutions to produce monthly forecasts. This technique was introduced since the '60 in the context of numerical weather prediction (Craddock et al., 1962; Epstein, 1969; Leith, 1974). It consists of inserting some perturbations in the initial conditions to simulate the initial analysis errors. Then a number of model runs is produced using these different initial conditions to construct the ensemble forecast. High computational resources are required to run models for the number of ensemble members needed to produce the forecasts. This problem is reduced in part using a lower resolution than the resolutions used to produce deterministic forecasts. The final products are predicted weekly to monthly atmospheric anomalies from the ensemble forecast mean or probability distributions related to these anomalies.

The predicted anomaly patterns could help in identifying the weather "regimes" associated with large–scale patterns (eg. Northern Atlantic Oscillation, Arctic Oscillation) that are occurring/will occur. These patterns correspond to the firsts Empirical Ortogonal Functions (EOF) that explain the largest part of atmospheric circulation variability on a planetary scale (Corti et al., 2003). They represent a persistent and/or recurrent large scale atmospheric circulation patterns associated with specific weather conditions on a regional scale. Weather "regimes" correspond to different phases of these patterns (eg. NAO+, NAO−, AO+, AO−). The ensemble members can be clustered and projected on these characteristic regimes

in order to predict the most probable weather conditions over particular regions.

The "weather regimes" that influence European climate have been found to be influenced by one of the recognized source of predictability in the monthly/subseasonal time scales, the Madden-Julian Oscillation (Cassou, 2008; Ferranti et al., 1990; Vitart and Molteni, 2010). This is an atmospheric kind of "oscillation" located in the equatorial belt (principally in the Pacific and Indian oceans), with a period of 40-50 days, in which the "active" phase is related to the tropical convection. Other minor sources of predictability are the stratospheric initial state (Baldwin et al., 2003), the snow cover and the soil moisture (Koster et al., 2010). The SST and sea ice cover impact on the atmosphere is still uncertain in the monthly time scale. Some studies show that SST strong gradients have a positive feedback on the close troposphere and on the storm tracks (Minobe et al., 2008). Woolnough et al. (2007) and Takaya et al. (2010) found that a better simulation of the SST can improve the MJO prediction skill and thus, through the teleconnections, the prediction skill over Europe.

The ocean modelling is a main issue in the framework of building a monthly forecasting system. There are several possible solutions, related to the ratio between the available computational resources and the skill of modelling methods adopted, as a function of the influence of the SST on the atmospheric circulation.

Actually a monthly forecasting system is operational at the ISAC-CNR in Bologna since May 2009. It is built using the atmospheric model GLOBO with the oceanic contribution simulated by a simple slab mixed layer model. The ensemble method is applied to issue the anomaly forecasts on 15-day and 30-day periods averages and the number of ensemble forecast members is 32. The calibration of the anomalies probability density functions is obtained using a model climate or "reforecast", which is composed by 42 members produced using initial conditions covering the period 1989-2009. A systematic, yet still only indicative, verification of the potentiality of the system, is carried out by means of anomaly correlations

and forecast errors evaluation. The principal aim of the present work is to find a new suitable and simple ocean model to be coupled with atmospheric global circulation model GLOBO in the monthly forecasting system, searching within different modelling solutions explored. Then the new model will be tested in order to verify if it produces realistic sea surface temperatures. Moreover it will be evaluated which is the impact of this new model on the atmospheric fields commonly used to issue forecasts with respect to the operational one.

The thesis is organized as follows: chapter 1 shows the problems of SST variability in a time scale of a month and the possible solutions to be adopted for the prediction of SST in this time range; chapter 2 describes in detail the atmospheric model GLOBO, developed at ISAC-CNR in Bologna, and the tests made in climatic mode to evaluate the systematic errors and the performance of the model to produce extended-range forecasts; chapter 3 describes the actual monthly forecasting system at ISAC-CNR; chapter 4 shows the applied changes to the ocean model and the results of the experiments with the new ocean model against the operational. Conclusions will focus on the summary and discussion of the principal results and will give a short overview of research perspectives.

Chapter 1

The extended-range forecast: different possible solutions for the ocean simulation

The main problem of monthly forecasting is to achieve a better prediction skill than persistence or climatology beyond the deterministic predictability limit of about 10 days. It is important, therefore, to simulate in the best way the source of predictability that are dominant in the time range of 10 to 30-40 days. As mentioned in the introduction, there are very few real or potential sources of predictability on the monthly time scale: one of the most important is the Madden-Julian Oscillation (Madden and Julian, 1971, 1972, 1994; Zhang, 2005) that links the atmosphere to the sea surface temperature through tropical convection. Other minor sources are represented by the SST global anomalies, the sea ice concentration, the soil moisture (Koster et al., 2010), the snow cover and the stratospheric initial state (Baldwin et al., 2003; Jung and Barkmeijer, 2006). Koster et al. (2010) found that a more realistic soil moisture initialization increases the skill of the surface temperature forecast but not so much that of the

precipitation. The stratospheric polar vortex varies relatively slowly compared to the tropospheric circulation. In many cases there is a propagation of stratospheric forcing to the lowest levels of the troposphere beyond 10 days, suggesting that there is predictability in this time scale. But the MJO has the most important role in the predictability for many areas of the world.

As found by Madden and Julian (1971, 1972), the MJO is a 40-50 day-period atmospheric oscillation. It is a near-global scale, eastward moving disturbance in surface pressure, tropospheric temperature and zonal winds over the equatorial belt. It represents the dominant mode of variability in the tropics (mainly in the Indian Ocean - Pacific sector), with time scales between one week and one season. It is associated with tropical convection (and, as a consequence, with SST) and it has its peak activity in the Northern Hemispere winter and spring. It has significant impact on the Indian Monsoon (Yasunari, 1979), on the Australian monsoon (Hendon and Liebmann, 1990) and on West African rainfall (Matthews, 2004). It can have an impact also on the onset of El-Nino events. Cassou (2008) found that there is some impact of the MJO on the weather regimes over Europe. He analysed the occurrence of the most important weather regimes in the North Atlantic sector (NAO+, NAO-, Atlantic Ridge, Scandinavian Blocking) with respect to every single MJO phase with a certain lag time (fig. 1.1). He found that, for example, in phases 3 and 4 of MJO there is an increase of occurrence of NAO+ regime with a lag of 10 days. The same happens for NAO- but for phases 7 and 8.

The correct simulation of the MJO in the numerical atmospheric models could help in improving monthly/submonthly forecasting skill in many areas of the globe. It is directly related to the SSTs, since tropical convection is associated with the active phase of MJO. The surface heat fluxes can influence the behaviour of convective systems and modify the propagation of the oscillation. Yao et al. (2011) found that tropical convection produces a lagged response of surface air temperature over the Northern America of about 2 weeks.

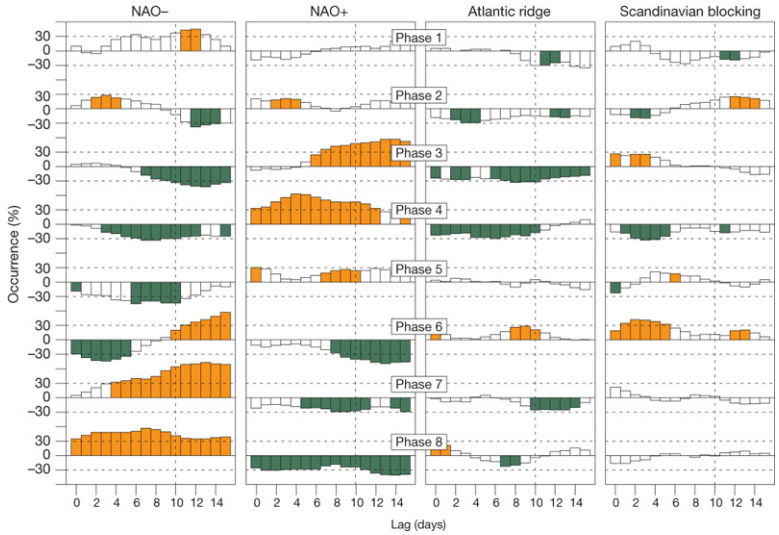

Figure 1.1: Percentage variation of occurrence of four weather regimes over Europe as a function of MJO phase and time lag (from Cassou, 2008.)

The influence of SST on the atmosphere on this and shorter time scales is quite difficult to quantify. The equatorial ocean surely has a large influence, overall in the seasonal time scale with the El-Nino events. The extratropical SST does not seem to have any detectable influence, even if some studies (Minobe et al., 2008) show that in regions where there are strong SST gradients there is some feedback on the atmosphere. Therefore a correct representation of surface sea temperature can help in improving the prediction skill of a monthly forecasting system. The question is how accurately should the SST be simulated. In other words, which kind of ocean model we need to use in order to have a significant impact of the SSTs on the atmospheric evolution with low computational resources and sufficiently high complexity level. Some modelling solutions have been analyzed to verify if they are suitable to this task.

A first simple method is to keep the initial SST constant throughout the simulation, i.e. persistence. The verification of this method has been carried out by computing autocorrelation in time of the SST in all the oceans. The data that were

used for this analysis are monthly SST means from dataset GODAS (Global Ocean Data Assimilation System, from National Centers for Environmental Prediction [NCEP],Behringer and Xue, 2004), that covers time range from 1979 to present. Figure 1.2 shows the global distribution of SST autocorrelation at lag 1 month for the period 1980-2008. In many areas autocorrelation values are above 0.7, with the equatorial Pacific area and some zones of southern midlatitudes having values above 0.9. This is due mainly to ocean dynamics with very long time scales, such as El-Nino. Areas with values below 0.7 are located along the western boundaries currents, in the Indian Ocean and in the Guinea Gulf, in which the SST are subject to larger and faster variability due to the ocean internal dynamics.

Apparently it seems that using persistence in a monthly forecasting system could be a good method to simulate ocean conditions. However the large errors tha can arise in the regions with low autocorrelation values (in particular in the western boundaries currents where there are strong horizontal SST gradients) can affect the atmosphere for example in the evolution of the storm tracks, as found by Palmer and Sun (1985) and Minobe et al. (2008).

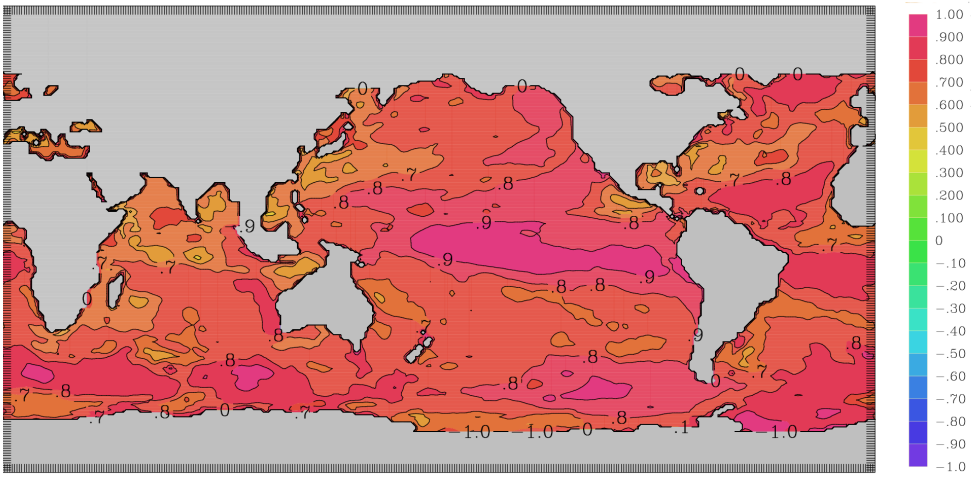

Figure 1.2: SST autocorrelation at lag 1 month for the period 1980-2008, derived from the GODAS dataset.

Another possible modelling solution is to modify the mixed layer depth as a function of the SST initial anomaly with a simultaneous feedback on the simulation of the SST, in order to introduce more variability in the surface heat fluxes. The formulation of the simple mixed layer model used to simulate the SST in the ISAC monthly forecasting system is the basis of this choice. The model contains a climatological annual cycle of mixed layer depth variable in space, for details see chapter 3.

A correlation analysis has been computed between the mixed layer depth and the SST, using the monthly data from GODAS dataset. Figure 1.3 shows as example the global distribution of the cross-correlation values for two months, January and July. As it possible to observe, the cross-correlation values are extremely variable in space and time, with negative values that are more diffused, especially in the midlatitudes of both the hemispheres. The tendency to have a prevalence of negative cross-correlation can be explained by the fact that when SST anomaly is positive the surface water is often less denser than the deep water, and therefore the internal vertical mixing is lower (altough salinity can change the density profile). High positive correlation values are found over the equatorial Pacific and all those areas where the internal ocean dynamics are the most prominent source of SST variability. In general the values of the cross-correlation are in the range -0.5 - $+0.5$, showing that there is not a clear and direct relationship between mixed layer depth and SST. Therefore a solution as described at the beginning of this paragraph in this case may result in large errors in the predicted SST field.

The third possibility explored deals with the simulation of the evolution of SST only in response to the surface heat fluxes. In this case the datasets used to check the validity of this assumption are ERA-Interim, for the period 1989-2008, and OAFlux (Objectively Analyzed air-sea Fluxes for the Global Oceans, (Yu et al., 2008) from Woods Hole Oceanographic Institute (WHOI), for the period 1985-2007. The contribution of surface net heat fluxes to the total SST climatological tendency have been analyzed using 10-day means. This choice is also due to the formulation of the model described in detail in chapter 3, since it simulates the SST as function of the net surface heat fluxes. The two datasets have been chosen to take into account different heat fluxes formulations. The ERA-Interim heat fluxes are modelled based only on its own fluxes-related variable analyses (surface wind, temperature and specific humidity, SST) and radiation parameterization scheme. The OAFlux dataset is obtained synthetizing satellite measurements and different numerical weather prediction analyses to minimize the error variance and improve accuracy.

A parameter ϵ has been defined and analyzed for both the datasets, whose expression is:

$$\epsilon = \frac{|\Delta SST_{CLIM}| - |\Delta SST_{FLUX}|}{|\Delta SST_{CLIM}| + |\Delta SST_{FLUX}|}, \tag{1.1}$$

where ΔSST_{CLIM} represents the total climatological mean tencency of the SST averaged over 10 days and ΔSST_{FLUX} represents the climatological mean tencency of the SST averaged over 10 days as obtained only by surface net heat fluxes. This parameter has been defined in order to evaluate the possible linear relationship of the SST from the net heat surface fluxes and to quantify the amount of the contribution of heat fluxes to the SST tendency. Values of $\epsilon \approx 0$ mean that, regardless for the sign, the net heat fluxes contribute entirely to climatological tendency, allowing to neglect other dynamical terms contributing to SST evolution. If $\epsilon \approx \pm 1$ it means that the contribution of the net heat fluxes is either too small

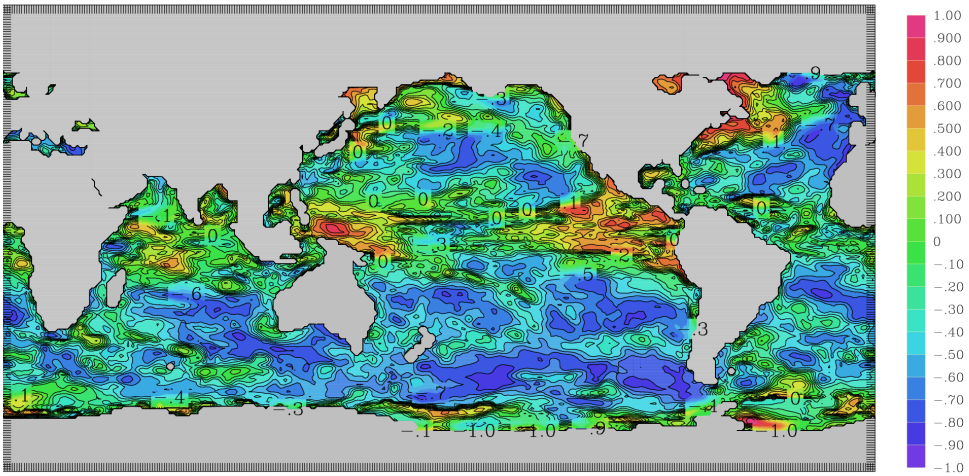

(a) January

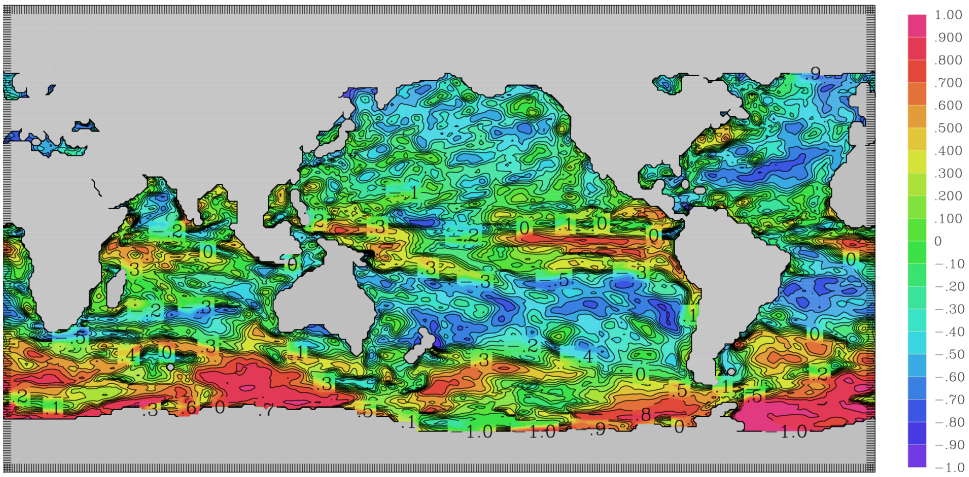

(b) July

Figure 1.3: Cross-correlation values between SST and mixed layer depth (monthly means) for the period 1980-2008, derived from the GODAS dataset. a) in January, b) in July.

or is balanced by other sources/sinks of heat. Figure 1.4 shows an example of the values of this parameter: there is a large spatial and time variability in sign and magnitude and the patterns are similar between the two datasets (not shown). Therefore the same conclusion found with the SST–mixed layer depth correlation analysis is achieved. There is not a uniform and linear relationship between SST and surface net heat fluxes. Hence predicting the SST only as a function of the surface net heat fluxes may also produce large errors.

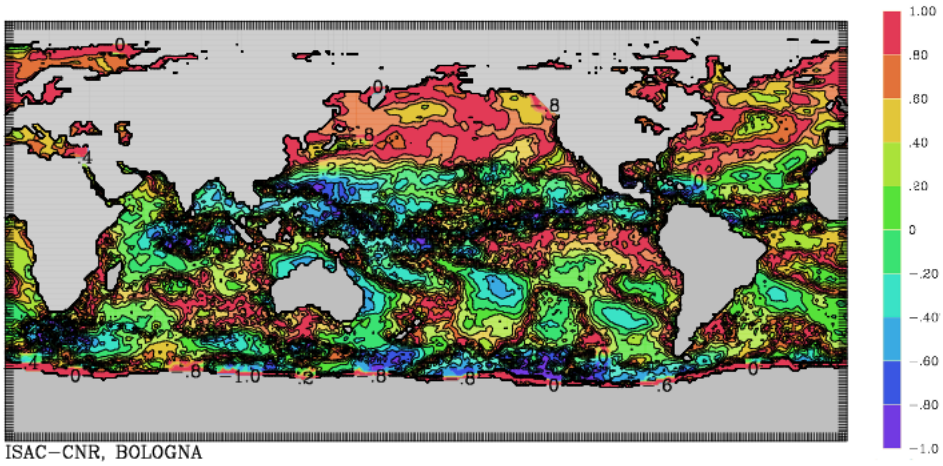

Figure 1.4: ϵ values for the third dekad of June, derived from OAFlux dataset.

Another possibility is the use of some statistical methods to infer the SST and then use this "prediction" to force an atmospheric model. In this research the statistical model used as example is the Pattern Projection Model (PPM; Kug et al., 2007). This model predicts the SST in a single grid point using the SST observed pattern in a certain domain. The model equation is as follows:

$$SST_i(t_f) = \alpha P_i(t_f),$$

where

$$\alpha = \frac{\frac{1}{T}\sum_t^T SST(t)P_i(t)}{\frac{1}{T}\sum_t^T P_i^2(t)},$$

$$P_i(t) = \sum_{x,y}^{D_i} \mathrm{cov}(x,y)\Psi(x,y,t-lag),$$

with

$$\mathrm{cov}(x, y) = \frac{1}{T} \sum_{t}^{T} SST(t)\Psi(x, y, t - lag),$$

where x, y and t denote longitude, latitude, and time grid respectively. Here P_i indicated a time series projected by the covariance pattern between predictand, SST(t), and predictor field, $\Psi(x, y, t - lag)$, in a certain domain D_i. The SST$_i$ is a prediction corresponding to the domain D_i, and α is a regression coefficient of the projected time series P_i, on the predictand SST during a training period T of at least 20 years from the date of prediction t_f. In the original study cited above the scheme was built to predict monthly SST values using monthly SST mean observed patterns. In our case it has been adapted to predict 10-day mean SST values using 10-day SST mean observed patterns. The reason of this shorter temporal mean is associated to the idea to produce monthly internal variability. The test consisted in evaluating a prediction of the SST for a whole annual cycle of a year of the past, using the previous 20 years of SST observed data, compared to the observed annual cycle of SST for the same year. The test has been reproduced varying the lag time from 1 to 4 dekads (i.e. 10-day means) and using the global oceans as predictor field. SST data used are from ERA-Interim dataset for the period 1989 – 2008. The year 2009 has been used as a year target for the prediction. The results show that the model worked very well in predicting SST in some areas of the global oceans. In other areas it shows unreliable predictions, for example in the El-Nino area (fig. 1.5). Similar results are obtained with different lag time. The model is capable to reproduce the SST annual cycle and the prediction has good skill when the observed annual cycle is similar to the climatological one, but it fails when there are strong anomalies or oscillations with a time scale of order of about 10-20 days. Therefore the use of this method presents similar issues encountered in the previous exposed methods, i.e. this model can develop large errors in the predicted SST.

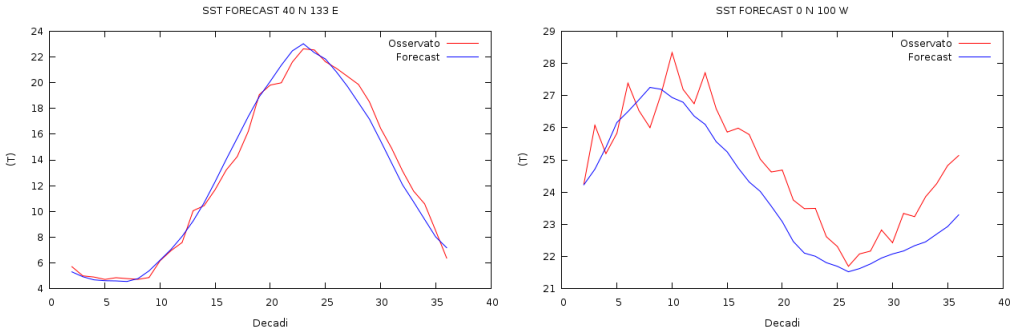

(a) Japan Sea (b) Eastern Equatorial Pacific

Figure 1.5: SST predicted by Pattern Projection Model (PPM) with a 1 dekad lag (blue line) and observed (red line) in a) the Japan Sea, b) the eastern equatorial Pacific, for the year 2009. Values in y-axis are in degree Celsius.

The next modelling solutions of the SST considered have a higher level of complexity. The first method analyzed is based on the possible use of mixed layer or columnar models, as suggested by a previous work of Takaya et al. (2010). They implemented an ocean mixed layer model, based on the non-local K profile parameterization (KPP; Large et al., 1994), in the IFS (Integrated Forecasting System) atmospheric model of the ECMWF in the context of the medium range and the monthly forecasting system. In the study of Takaya et al. (2010), it is shown that this mixed layer model helps in improving the prediction skill for the MJO and the Indian Monsoon adding small computational time with respect to the operational system. On the other hand, there is no improvement in the predictive skill of the atmospheric variables over the northern and southern extratropics. A systematic bias in the SST is found in the areas where the ocean dynamics are very dominant (El-Nino and western boundaries currents). However an improvement in the forecast skill of the SST in the summer hemisphere and a better representation of the diurnal cycle of the SST are found, suggesting the possibility to use this kind of model in the operational system.

One of the issues arising from the utilization of a mixed layer model is that it

requires the initial conditions non only for the surface but also for all the vertical levels that should be used, with the necessity to find reliable ocean analysis. It is necessary also to take into account the salinity, doubling the number of initial conditions to be provided to the model.

Similar problems arise also for the last possible solution considered, i.e. the use of a full 3D ocean model. Other problems are also due to the drift that this kind of model suffers and to the initialization shock. This refers to the adjustment process that takes place when the ocean and atmosphere initial conditions are not a solution of the coupled model (Balmaseda et al., 2009). As common technical problem, too high computational cost is required to run a coupled model. This constrains the ocean model to have a coarse horizontal and vertical resolution, with the latter being very important in the first meters of the ocean to reproduce SST diurnal cycle. The full 3D ocean model is in principle the best possible representation of the global ocean. However the forecast skill could be even worse than using persistence, unless a very high resolution is achieved that allows to resolve the very small ocean spatial scales that are important for the monthly–scale dynamical evolutions. The implementation of such a model should imply, as a consequence, a considerable additional computational cost.

Chapter 2

The GLOBO model

The GLOBO model (GLObal BOlogna) is a grid-point atmospheric global circulation model (Malguzzi et al., 2011) developed at ISAC (Institute of Atmospheric Science and Climate) of CNR (National Research Council) in Bologna. It is an extension to the global atmosphere of the meteorological model BOLAM (BOlogna Limited Area Model) developed at the same institute. Currently it is used to produce operational daily medium range weather forecast (up to 6 days) and, once a month, extended range atmospheric forecast (up to 35 days) by means of an ensemble prediction system.

2.1 Description of the model

2.1.1 Dynamical formulation

The GLOBO model has a split-explicit time scheme, that generally requires shorter time steps than semi-implicit and semi-Lagrangian method, but it is more simple to implement and more accurate in the description of the phase speed of gravity waves. It is also more suitable to the implementation on high-performance parallel-computing architectures. The polar singularities are dealt with by the

application of a simple polar average, consisting in a smooth low-pass filter.

GLOBO integrates in time the hydrostatic primitive equations in horizontal coordinates of latitude and longitude (λ, θ). The main prognostic variables are the horizontal component of velocity (u,v), the surface pressure P_S and the virtual temperature T_v.

It uses a hybrid vertical coordinate system in which the terrain-following coordinate σ ($0 < \sigma < 1$) smoothly tends to a pressure coordinate P with increasing heigh above the ground by means of the following formula:

$$P = P_0\sigma - (P_0 - P_S)\,\sigma^\alpha \tag{2.1}$$

where P_0 is a reference pressure and α is a costant chosen as

$$\alpha < \frac{P_0}{P_0 - min\,(P_S)}$$

.

$\alpha = 1$ implies that the coordinate is reduced to classical σ. The horizontal momentum equations in this type of coordinate become

$$\frac{\partial u}{\partial t} - uv\frac{\tan\theta}{a} - 2\Omega\sin\theta \times v = \frac{-R_d T_V}{a\cos\theta}\frac{P_S\sigma^\alpha}{P_0\sigma - (P_0 - P_S)\sigma^\alpha}\frac{\partial \ln P_S}{\partial\lambda} - \frac{1}{a\cos\theta}\frac{\partial\Phi}{\partial\lambda} \tag{2.2}$$

$$\frac{\partial v}{\partial t} - u^2\frac{\tan\theta}{a} - 2\Omega\sin\theta \times u = \frac{-R_d T_V}{a}\frac{P_S\sigma^\alpha}{P_0\sigma - (P_0 - P_S)\sigma^\alpha}\frac{\partial \ln P_S}{\partial\theta} - \frac{1}{a}\frac{\partial\Phi}{\partial\theta} \tag{2.3}$$

where R_d is the perfect gas constant for dry air, a is the earth's radius, Ω is the earth's angular velocity, and Φ is the geopotential height. The last parameter is computed by vertical integration of the hydrostatic equation:

$$\frac{\partial\Phi}{\partial \ln\sigma} = -R_d T_V \frac{P_0 - \alpha(P_0 - P_S)\sigma^{\alpha-1}}{P_0 - (P_0 - P_S)\sigma^{\alpha-1}}. \tag{2.4}$$

The equations for surface pressure and the generalized vertical velocity $\dot{\sigma}$ are derived from the integration of the continuity equation, which assumes the following general form:

$$\frac{\partial}{\partial t}\left(\frac{\partial P}{\partial \sigma}\right) + \frac{\partial}{\partial x}\left(u\frac{\partial P}{\partial \sigma}\right) + \frac{\partial}{\partial y}\left(v\frac{\partial P}{\partial \sigma}\right) + \frac{\partial}{\partial \sigma}\left(\dot{\sigma}\frac{\partial P}{\partial \sigma}\right) = 0.$$

The results are

$$\frac{\partial P_S}{\partial t} = -\int_0^1 D\, d\sigma \tag{2.5}$$

and

$$\dot{\sigma}\frac{\partial P_S}{\partial \sigma} = -\sigma^\alpha \frac{\partial P_S}{\partial t} - \int_0^\sigma D d\sigma \tag{2.6}$$

where

$$D = P_0(1-\alpha\sigma^{\alpha-1})D_1 + \alpha\sigma^{\alpha-1}D_2(P_S)$$

$$D_1 = \frac{1}{a\cos\theta}\left[\frac{\partial u}{\partial \lambda} + \frac{\partial (v\cos\theta)}{\partial \theta}\right]$$

$$D_2(P_S) = \frac{1}{a\cos\theta}\left[\frac{\partial u P_S}{\partial \lambda} + \frac{\partial v P_S\cos\theta}{\partial \theta}\right] \tag{2.7}$$

and where the derivative of 2.1 has been used. The thermodynamic equation is:

$$\frac{\partial T_V}{\partial t} = \frac{R_d T_v}{C_P}\frac{\omega}{P} \tag{2.8}$$

(where C_P is the specific heat at constant pressure) in which the so-called omega-alpha term can be written in terms of the quantities 2.7 as

$$\frac{\omega}{P} = \frac{1}{P_0\sigma - (P_0 - P_S)\sigma^\alpha} \times \left\{\sigma^2[D_2(P_S) - P_S D_1] - int_0^\sigma D\, d\sigma\right\}. \tag{2.9}$$

Equations 2.2 - 2.9 togheter with the conservation laws of specific humidity q and of the other water species (cloud water and ice, rain, snow and graupel-hail) constitute the dynamical core of the model.

2.1.2 Numerical discretization on the sphere

The model prognostic variables are distributed in the vertical on a regular Lorenz grid, while the horizontal discretization is based on a staggered Arakawa C grid. The grid points located at the North and South Poles carry T points only (see stencil in fig. 2.1).

The shaded region in figure 2.1 is treated as a single volume and tendencies are computed by averaging over that area. In particular, the divergences D_1 and D_2 at the poles are discretized by computing the net flux across the boundary of the polar grid box divided by the area, according to Gauss's theorem. The same approximation is made for the horizontal advection of T variables at the poles, which can be written in flux form as follows:

$$u\frac{\partial T}{\partial x} + v\frac{\partial T}{\partial y} = D_2(T) - TD_1 \tag{2.10}$$

The advection scheme presently implemented is the accurate, nondispersive flux-form weighted-average flux scheme (WAF; Billet and Toro, 1997). To prevent Courant–Friedrichs–Lewy (CFL) instability due to the convergence of meridians near the poles, multiple swaps are performed in the longitudinal direction to keep the Courant number smaller than one, as described in Hubbard and Nikiforakis (2003). The implementation of the WAF scheme to compute the D_2 terms appearing in the advection expressions, like in 2.10, is extended here also to the computation of D_2 (P_S) (see Eq. 2.7), in place of the usual centered approximation. This is a novel feature of GLOBO (and BOLAM), which allows a better estimate of the mass flux divergence. To avoid the collapse of the time step near the poles

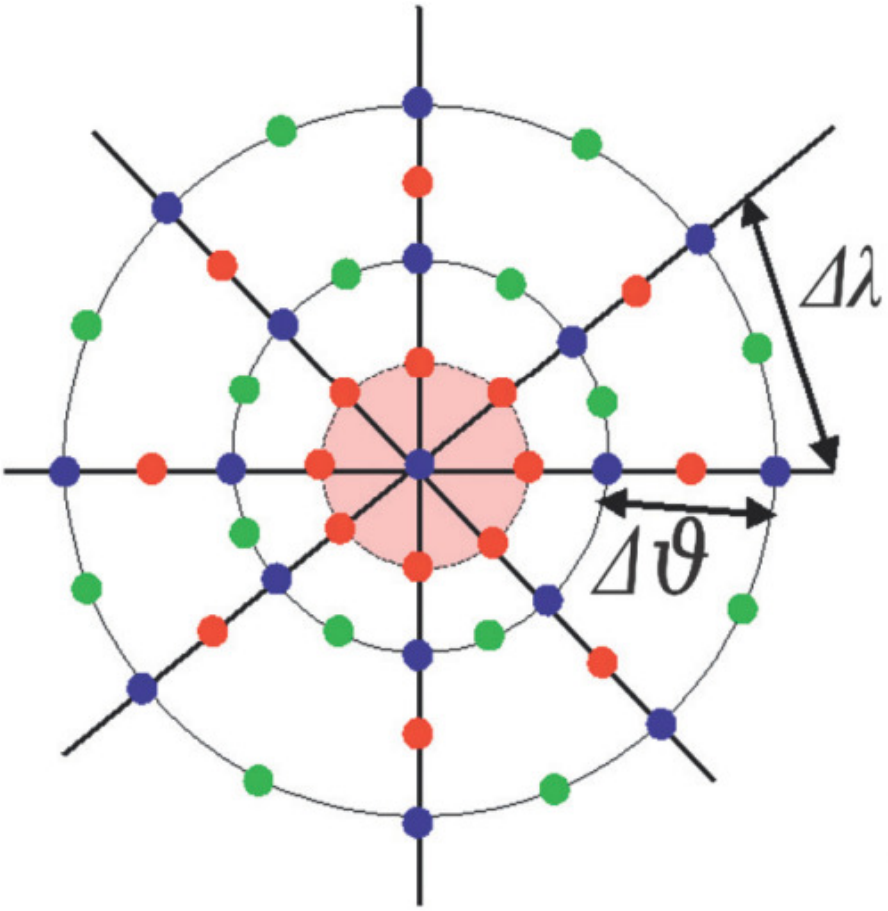

Figure 2.1: Arakawa C grid at the poles. Blue, red, and green dots are for T, V, and U points, respectively. The red-shaded area is the polar volume.

in the time integration of the gravity modes, it is sufficient to operate a zonal average of the divergences D_1 and D_2 appearing in Eq. 2.7. This is accomplished by iterating the simple three-point digital filter:

$$f_j^{\tau+\nu} = (1-\nu)f_j^\tau + \nu(0.25f_{j-1}^\tau + 0.5f_j^\tau + 0.25f_{j+1}^\tau), \quad \nu \leq 1, \tag{2.11}$$

where j denotes the grid point along the longitude and τ represents the iteration. The asymptotic behavior of large τ can be expressed as the convolution with the Green function of the heat diffusion problem:

$$f_j^\tau = \sum_i \left[\frac{1}{\sqrt{\tau\pi}} e^{-(j-i)^2/\tau} f_i \right]. \tag{2.12}$$

Hence, by the convolution theorem, the nth component of the zonal Fourier transform of $f(\lambda)$ averaged t times is the nth component of f itself multiplied by the Gaussian weight

$$e^{-(n/n_T)^2}, \tag{2.13}$$

where

$$\tau = \frac{4}{n_T^2 \Delta\lambda^2}. \tag{2.14}$$

Expression 2.14 tells how many times the digital filter 2.11 should be iterated to get the smooth spectral damping around wavenumber n_T defined by 2.13. If $2N$ denotes the number of grid points along longitude, in order to have the same effective zonal resolution at all latitudes above a given latitude θ_0, it must be set to $n_T = N\cos\theta/\cos\theta_0$. Coding of 2.12 would be too expensive in terms of computer time. Hence, a hybrid filtering approach is adopted: the zonal average is performed by iterating 2.11 over those latitudes for which $\tau < 100$ and by applying the low-pass spectral filter 2.13 at the remaining latitudes closer to the poles, with $\theta_0 = \pi/4$. Diffusion and filters help maintaining the numerical stability

and are always needed to prevent a buildup of energy at the smallest scales due to a truncated energy cascade. To prevent the insurgence of nonlinear instability and small-scale noise, a second-order Shapiro (Shapiro, 1970) digital filter that efficiently removes mesh- scale noise without affecting the physical structures of a field is applied at the end of each time step on both velocity and temperature tendencies. The filter is obtained by extending 2.11 with $\tau = 0$ to the meridional direction. For similar reasons, polar averages must be performed on velocity and temperature tendencies generated by the physical parameterizations. In addition, a divergence damping term, defined by the following u and v tendencies

$$\frac{\partial u}{\partial t} = \frac{\mu}{a\cos\theta}\frac{\partial D_1}{\partial \lambda}, \quad \frac{\partial v}{\partial t} = \frac{\mu}{a}\frac{\partial D_1}{\partial \theta} \tag{2.15}$$

is applied at each gravity time step to diffuse the divergent part of the flow, preventing the accumulation of energy at small scales, especially in subtropical regions. The damping coefficient is evaluated as follows:

$$\mu = 0.15 \times \frac{1}{8}\frac{dy^2}{dt} \tag{2.16}$$

2.1.3 Physical parameterizations

The GLOBO physical scheme consists of the parameterizations of the surface layer (SL), of the planetary boundary layer (PBL), of the vertical diffusion in the "free" atmosphere, of the microphysical processes related to slantwise precipitation (both solid and liquid), of the convective precipitation, of the soil water and thermal balance (including vegetation), of the atmospheric radiation, and of the gravity wave drag related to excitation of orographic waves. The SL is modeled accordingly to classical Monin–Obukhov similarity theory (Monin and Obukhov, 1955). The Businger (see Feagle and Businger, 1980) stability functions are used in the unstable SL, while Holtslag (Beljaars and Holtslag, 1991) functions apply

to the stable case. The roughness length over land, initially defined depending on the vegetation and subgrid orographic variance, is also modified as a function of snow coverage conditions. Over the sea, a Charnock roughness representation is introduced for computing momentum fluxes. It takes into account the dependence of wave height on the surface wind speed, while roughness lengths for temperature and humidity in stable and unstable conditions are defined according to Large and Pond (1981).

The mixed layer (ML)-based turbulence closure, widely used to compute the PBL fluxes for atmospheric modeling (see, e.g., Cuxart et al. 2006), is applied to model the turbulent vertical diffusion of momentum, potential temperature, and specific humidity in the free atmosphere. The turbulence closure is of order 1.5, in which the turbulent kinetic energy (TKE) equation is integrated in time (Zampieri et al., 2005). However, given the relatively low resolution employed in GLOBO, advection of TKE is not computed because it is usually negligible with respect to local sources and sinks. To take into account buoyancy effects in cases of a saturated atmosphere, the ML definition depends on the Richardson number based on the equivalent potential temperature. In the unstable case, a modified version of the nonlocal ML (Bougeault and Lacarrere, 1989) is applied while, in the stable case, a modified Blackadar (Blackadar, 1962) formulation is used. Finally, the TKE dissipated is fed back into resolved temperature in the form of "frictional heating".

GLOBO includes an original soil model that implements three prognostic and one "climatological" layers, with depths ranging from a few centimeters to more than 1 m, increasing downward. The soil model computes the heat and water vertical transfer and vegetation effects at the surface (transpiration and interception of precipitation) and in the soil (extraction of water by roots depending on wilting conditions), taking into account different soil types and physical parameters. The soil model includes a treatment of freezing and melting processes of the water

content. At the surface, the evolution of the snow cover is computed, taking into account snow accumulation and melting, with a single- layer, snow mantle model. A surface skin temperature is defined by imposing no net flux divergence of heat at the soil-atmosphere interface. The water balance at the surface (including runoff and pond formation) is calculated. Albedo and emissivity variations are also computed as a function of the uppermost soil water content. The sea surface temperature is predicted using a slab- ocean model, where latent and sensible heat fluxes, and radiation contributions, are taken into account. The same kind of model is adopted over the sea ice fraction, which is assumed to remain constant during the forecast period. The large-scale stratiform precipitation and microphysical processes are treated with a simplified approach, suitable for non-convection-resolving models, and similar to that proposed by Schultz (1995). Schultz compares the results of his scheme against both the results of a well-documented research microphysics algorithm and observations, finding generally skillful precipitation forecasts with the advantage of low computational costs. The scheme includes five water categories: cloud ice, cloud water, rain, snow, and graupel-hail. Horizontal and vertical advection is applied only to cloud water and ice-specific quantities; and is neglected for other hydrometeors. The fall of hydrometeors is computed by means of the conservative (and dispersive) backward-upstream integration scheme. The subgrid-scale precipitation is treated in GLOBO following the Kain–Fritsch (KF) convective parameterization scheme (Kain and Fritsch, 1990; Kain, 2004). The KF scheme has shown considerable success in simulating the development and evolution of convection under a variety of convective and synoptic environments (Kuo et al., 1996; Wang and Seaman, 1997; Ferretti et al., 2000). The KF scheme is based on the Fritsch–Chappel triggering algorithm, with improvements on the detrainment effect and the cloud model. It has been developed for mesoscale models with a grid size of a few tens of kilometers. In this scheme, convection is triggered by lifting a lower-level slab layer with an impetus heating as a function of the grid-scale vertical

motion at the lifting condensation level. The convective adjustment is based on convective available potential energy (CAPE) and, once convection is triggered, CAPE is assumed to be removed in a grid column within a convective time scale. This time scale is in the range of 30–40 min, depending on the averaged wind speed between the lifting condensation level and 500 hPa. The triggering vertical velocity is automatically adjusted to the grid spacing. The KF parameterization used in GLOBO has been completely recoded, using liquid water static energy (instead of a Bolton approximation of the equivalent potential temperature) as the thermodynamic conserved quantity. Moreover, additional modifications have been introduced with respect to the Kain (2004) version regarding the dependency of the downdraft on ambient relative humidity (the downdraft mass flux has been increased at low humidity) and the precipitation rate (the fraction of total condensate converted into precipitation has been made to increase with height above the cloud base). The cloud-depth threshold establishing the onset of shallow convection has been increased. The above changes tend to diminish slightly, on average, the temperature at lower-tropospheric levels around and below cloud base, hence stabilizing a little more efficiently the lower troposphere. This has also the effect of reducing to some extent the intensity of small-scale cyclogenesis in the presence of convection.

Radiation fluxes are computed with a combined application of the Geleyn scheme (Ritter and Geleyn, 1992) and the European Centre for Medium-Range Weather Forecasts (ECMWF) scheme [cycle 26; Morcrette (1991); Mlawer et al. (1997)], with the Tegen et al. (1997) aerosol climatology. The Geleyn scheme, with the option of maximum cloud coverage, is called approximately every 0.5 h, and has been modified to take into account explicit cloud concentration. The ECMWF scheme is used to correct the surface and internal radiative fluxes of the Geleyn scheme. It is computed every 1.5 h at alternate horizontal grid points to reduce the computational time. Surface fluxes of visible and infrared radiation are

then converted into one-timestep increments to obtain a smooth time evolution of surface temperature and turbulent fluxes of heat and moisture. Local cloud fraction is parameterized by a linear function of explicit cloud water/ice content, corrected with a linear function of relative humidity to account for subgrid fluctuations leading to cloud formation close to saturation.

Finally, a simple gravity orographic wave drag parameterization has been introduced, which basically follows the formulation used by Baines (1995), with some modifications. The drag vector is computed starting from the wave momentum flux near the surface, assumed proportional to the near-surface wind speed perpendicular to the local orographic relief, to the moist Brunt–Vaisala frequency, and to a function of the orographic profile along the direction of the wind vector that identifies topographic crests. The gravity wave momentum fluxes (upward and downward) are computed in a layer from the surface up to a critical level, defined as the first level, starting from below, where the scalar product between the local wind vector and the orographic drag vector becomes null or positive. In the case where a critical level is not encountered, the wave momentum flux is assumed to remain constant up to the first layer where the Richardson number becomes lower than a critical value (set to 0.25). Momentum flux divergence is modeled as a function of the local Richardson number, while partial reflection is assumed to occur at critical levels. The result is that wave drag can act in deep or shallow atmospheric layers above topography crests (no attempt has been made to spread it horizontally), depending on the stratification and shear. Application of the orographic drag reduces the error in the climatological westerly flow at midlatitudes, especially in the Northern Hemisphere. A positive impact has been also observed on the planetary wave dynamics at short time scales.

2.2 Evaluation of systematic error

The systematic and forecast errors of GLOBO for medium range forecasts has been assessed and compared with those of ECMWF model with the same resolution as in a previous study (Malguzzi et al., 2007). However, to develop an extended–range prediction system it was necessary to evaluate its performance and systematic errors for long term or climatic integrations. Therefore, a climatology of several atmospheric parameters has been created and compared with observed climatology. The last one has been obtained from the ERA-Interim dataset which at time was composed by 10 years of 6h-data covering years 1989 to 1998, with a horizontal resolution of 1.5 degrees. The GLOBO climatology was composed also by 10 years integrations. In evaluating the model climate, the first month of integration is not considered, because during this period the model atmosphere preserved some "memory" of the arbitrary initial condition, implying that the model "trajectory" may lie out of the model "attractor". The boundary forcing from land and ocean was set up as follows: the ocean was represented by an annual cycle of long term 10-day SST, ice temperature and ice cover averages; in the same way the temperature and the soil moisture of the deep climatological soil model level were defined. The same climatological quantities were extracted from the ERA-Interim dataset too. The horizontal resolution of the model was set to 1 °lon × 0.93 °lat, with 40 vertical levels. As first result, the model was capable to achieve a 10-years integration without any numerical problem.

2.2.1 Evaluation of long-term annual means

The most common atmospheric parameters have been analyzed through their climatological annual mean as 2D fields (mean sea level pressure, 2 meters temperature, precipitation, geopotential height at 500 hPa) and zonal mean fields (temperature, zonal wind, relative humidity). They have been compared with their

observed counterparts. Starting from the precipitation field (fig. 2.2), we can notice that it is in good agreement with observations, expecially in the storm–tracks and in the equatorial maxima, with the correct split of InterTropical Convergence Zone (ITCZ) in the Pacific Ocean. However the GLOBO model tends to overestimate convective precipitation in tropical areas of western Pacific and in the region of the Sahel. It is also evident the common climatic model error about the precipitation in the northern part of the Indian Ocean. Other minor differences are found in South America, East Africa and North Atlantic area. As for the mean sea level pressure (MSLP), we have a good agreement in the patterns, but the model tends to produce more intense subtropical highs and mid-latitude low pressures in both the hemispheres, indicating a stronger zonal circulation than in reality (fig. 2.3). Also a southern shift of MSLP in northern Europe and Asia is found. The 2 meter temperature generally presents a satisfactory match between model and observations, but the model tends to produce colder temperatures (about 1-2 °C) over the equatorial oceans (fig. 2.4). This bias in temperature extends to the whole trophosphere, impacting also the geopotential height at high levels through hydrostatic law. The geopotential height at 500 hPa has been analyzed only for the Northern Hemisphere. For the temperature bias previously explained, this parameter has generally lower values than the obervations. Nevertheless, the mean pattern is very similar to the observed one. The maximum error is located in the central sector of the North Pacific area. It has a positive bias as opposed to the rest of the NH, due to a excessively intense Hadley cell. However in the Euro-Atlantic region, the model climatology is quite correct (fig. 2.5).

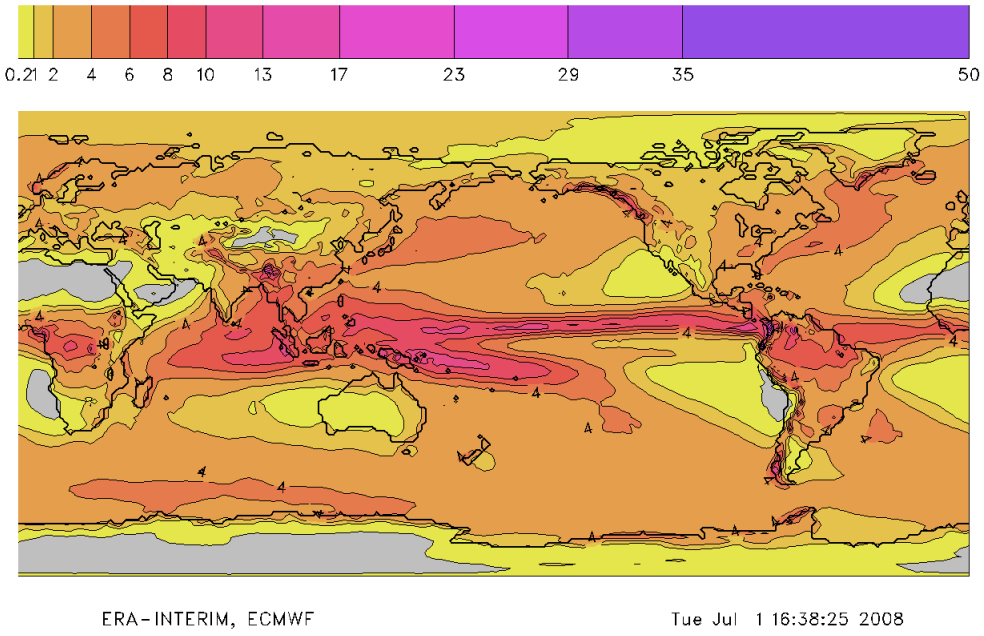

(a) ERA-Interim

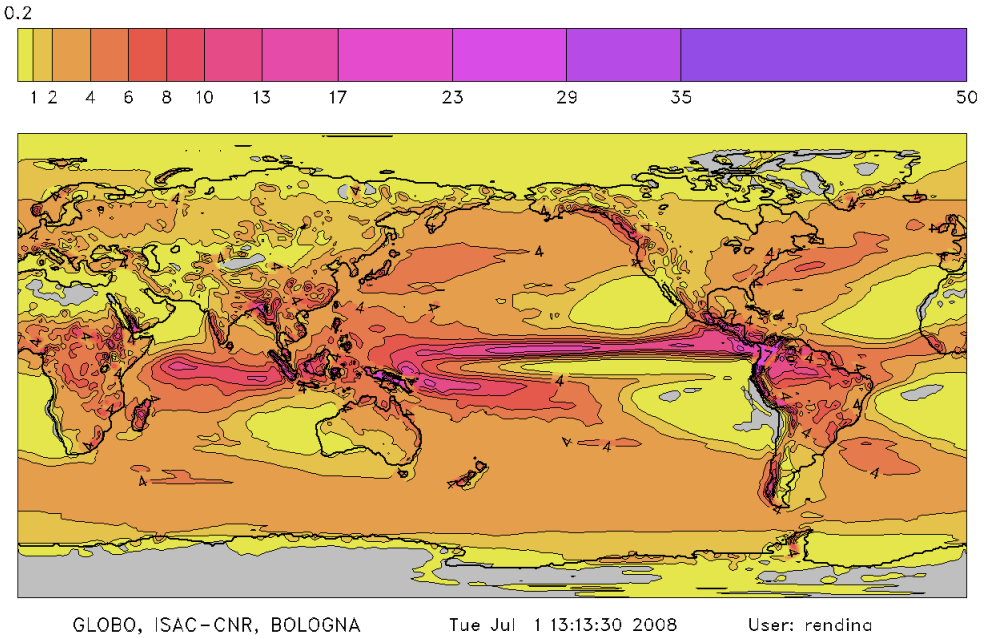

(b) GLOBO

Figure 2.2: Global precipitation, long-term annual mean, in mm/day. a) ERA-Interim, b) GLOBO

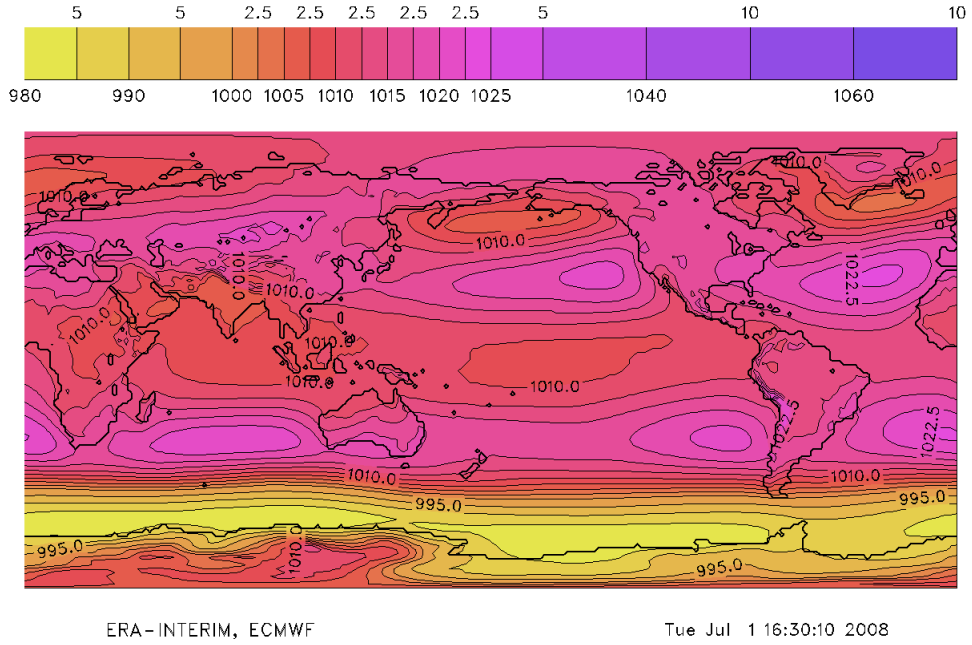

(a) ERA-Interim

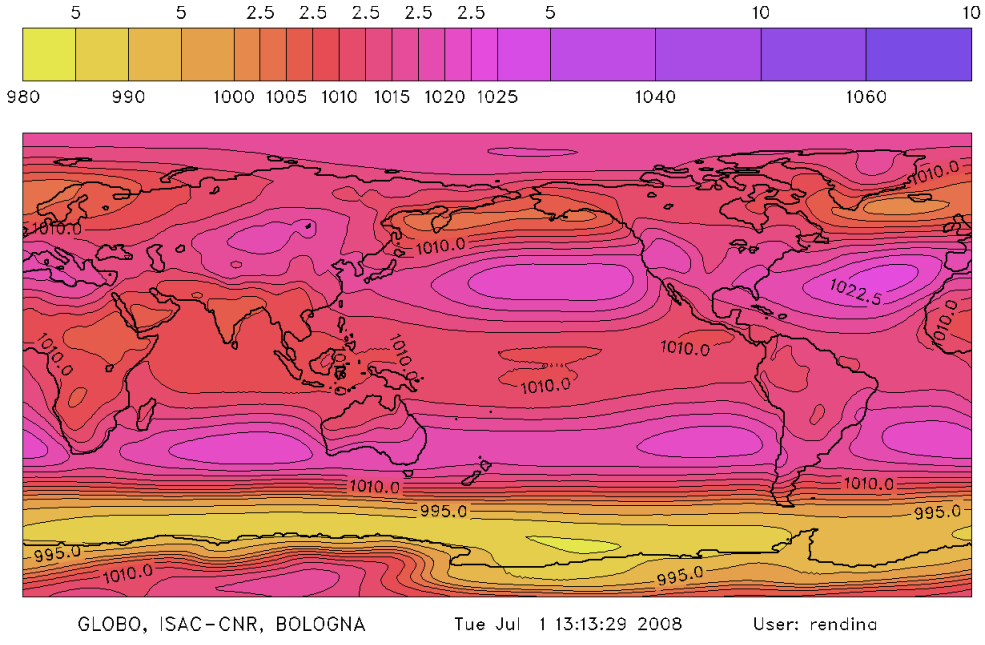

(b) GLOBO

Figure 2.3: Global mean sea level pressure, long-term annual mean, in hPa. a) ERA-Interim, b) GLOBO

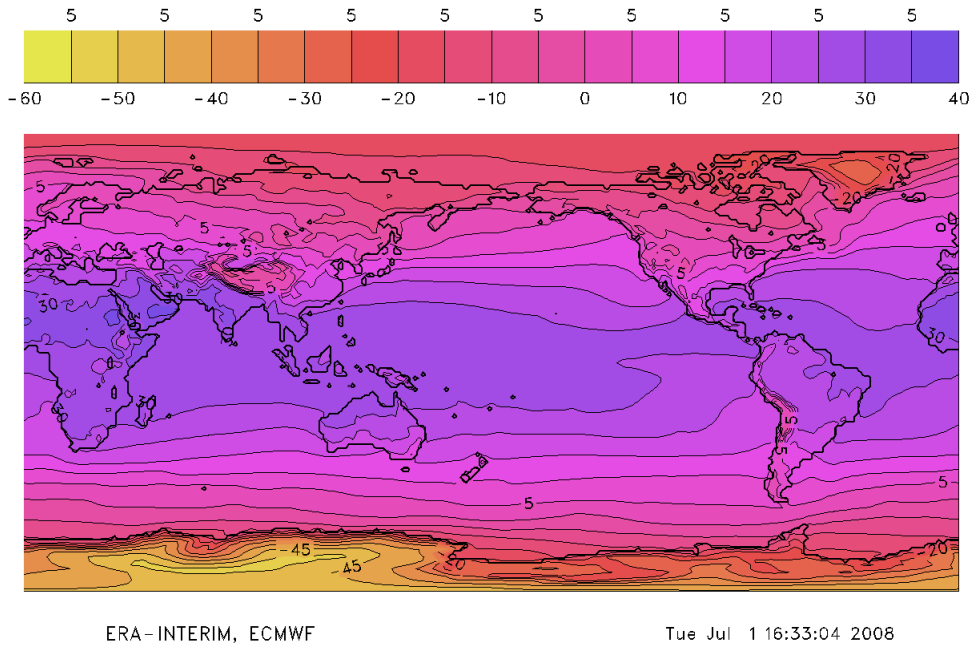

(a) ERA-Interim

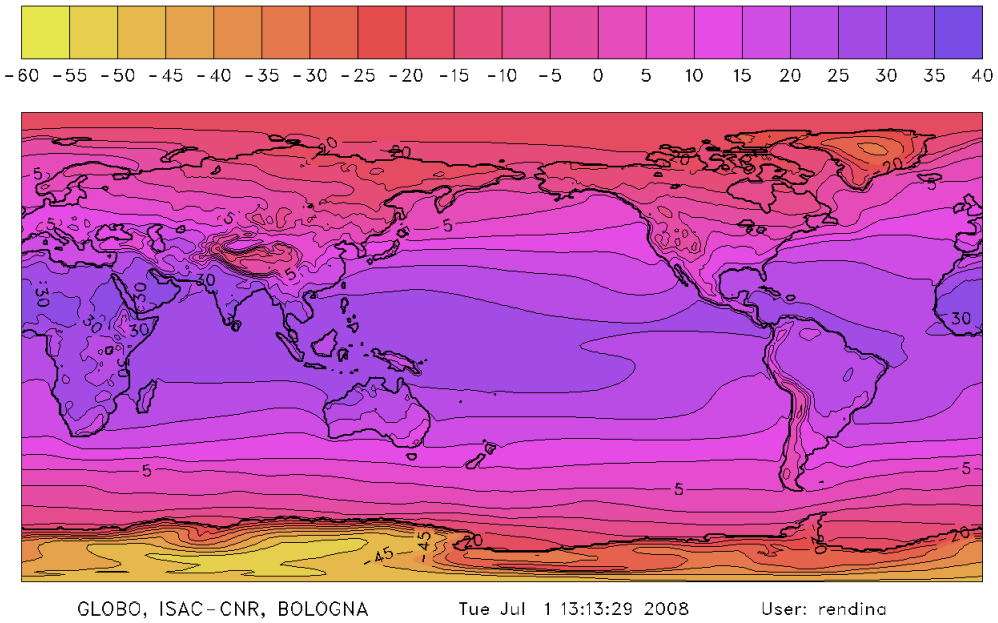

(b) GLOBO

Figure 2.4: Global temperature at 2 meters, long-term annual mean, in °C. a) ERA-Interim, b) GLOBO.

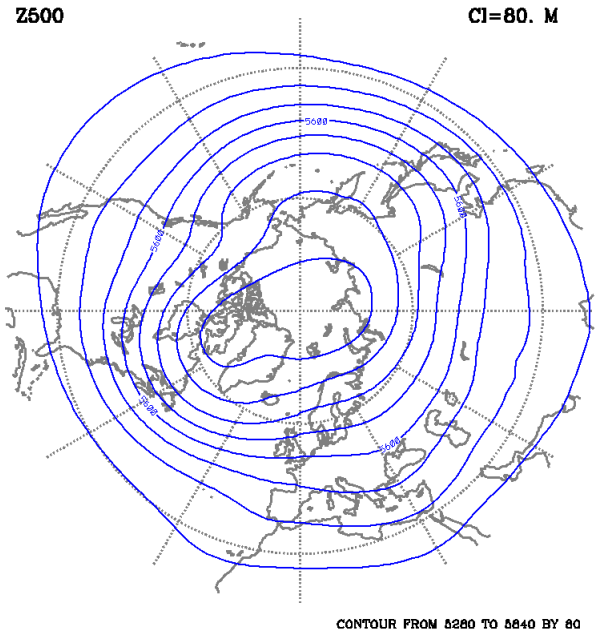

(a) ERA-Interim

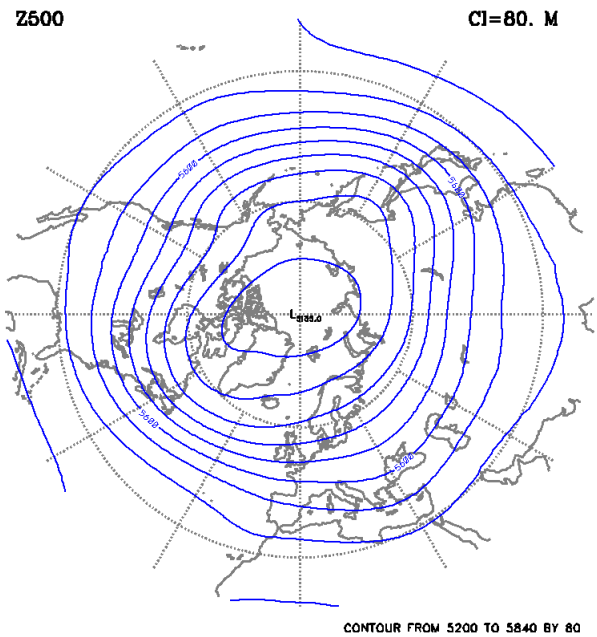

(b) GLOBO

Figure 2.5: Geopotential height at 500 hPa in the Northern Hemisphere, long-term annual mean, in meters. a) ERA-Interim, b) GLOBO

From the geopotential height field, using the algorithm described in Tibaldi and Molteni (1990), the longitudinal distribution of the blocking events frequency has been assessed for the GLOBO model in the winter season for the Northern Hemisphere (fig. 2.6). As a consequence of the more zonal circulation of the model with respect to the observed one, the frequency of blocking events simulated by GLOBO is quite underestimated, with the Atlantic maximum displaced further east, altough the pattern is similar to the observed. The frequency of blocking highs rises a lot after correcting the geopotential values by the monthly biases, but the western sides of the frequency maxima are still underestimated. Nevertheless, the systematic errors showed here are similar to those of others climatic models with similar characteristics (Gates et al., 1998; Jung and Tompinks, 2003; Martin et al., 2005).

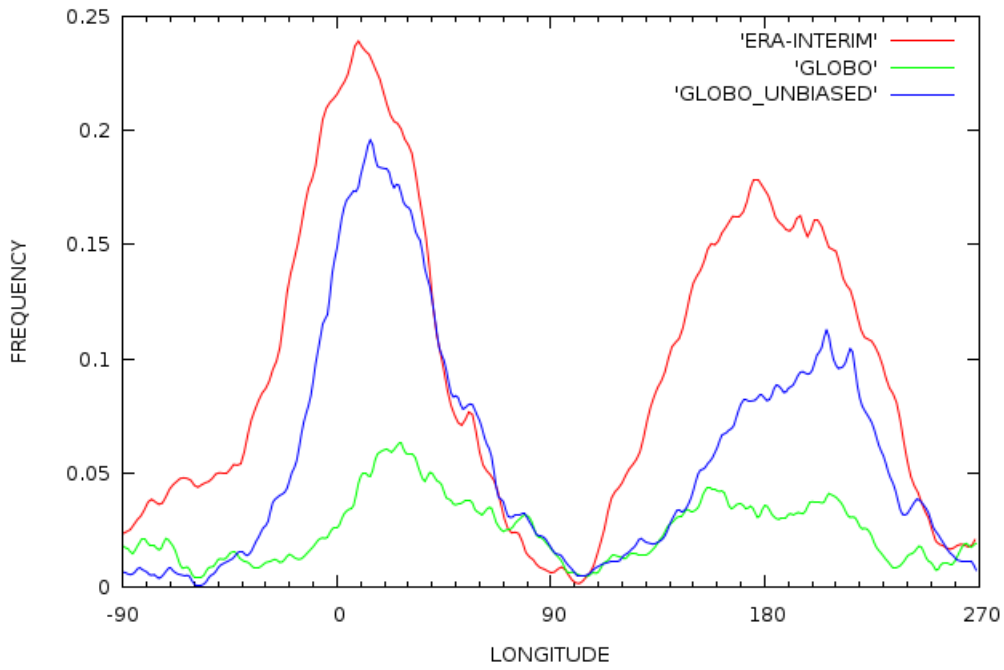

Figure 2.6: Instantaneus blocking frequency as function of longitude: observed from ERA-Interim (red line), simulated by GLOBO (green line) and simulated by GLOBO with bias correction (blue line).

2.2.2 Zonal means

A comparison of three parameters, averaged in time and zonally, has been made in order to verify sistematic errors at all vertical levels. As previously discussed, temperature shows a generally satisfactory model performance against observations. However observing directly the difference field (GLOBO minus ERA-Interim), the model shows a cold bias of about 2 °C in almost all the troposphere, with a warm bias only in the lower stratosphere (fig. 2.7). Also the zonal mean of the zonal wind component shows good agreement with the observations, with the two jet streams located at the correct height. The main differences are the stronger zonal wind component in both the hemispheres and the poleward displacement of the two maxima with respect to the observed ones. There are also more intense

trade winds, reflecting the tendency of the model to have a more zonal circulation than in the observed climate. Finally, regarding the relative humidity field, it shows a little dry bias in the tropical troposphere and a strong wet bias in the two polar areas of the troposphere.

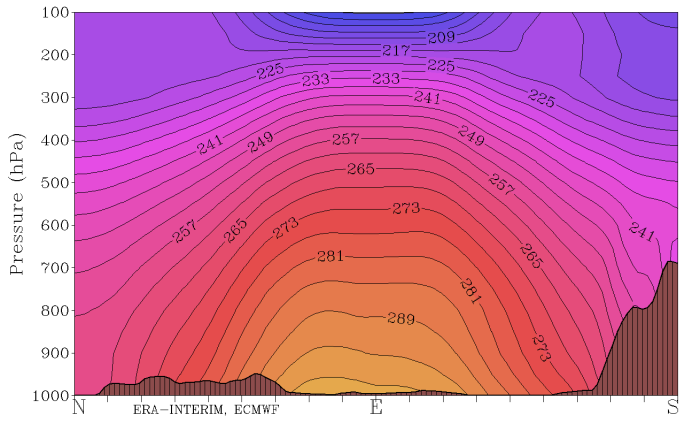

(a) ERA-Interim

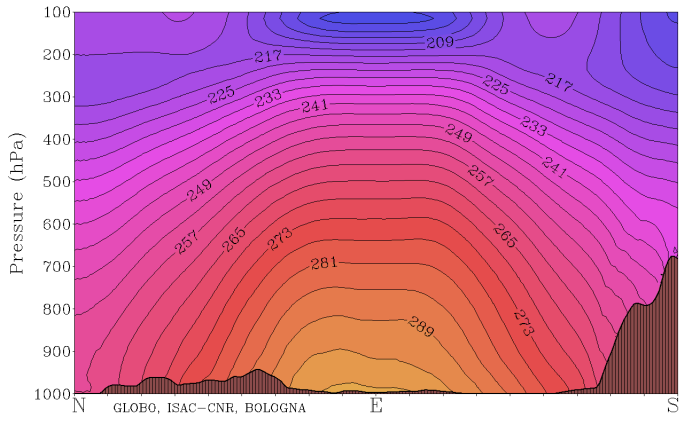

(b) GLOBO

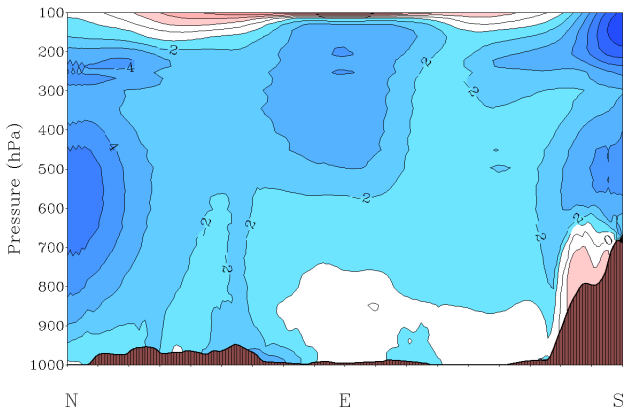

(c) Difference

Figure 2.7: Zonally averaged annual mean temperature: a) Era-Interim, b) GLOBO and c) Difference (GLOBO - ERA-Interim). In figures a) and b) contour lines every 4°C. Blue colors in figure c) represents negative values, red colors positive values. Contour lines every 1°C.

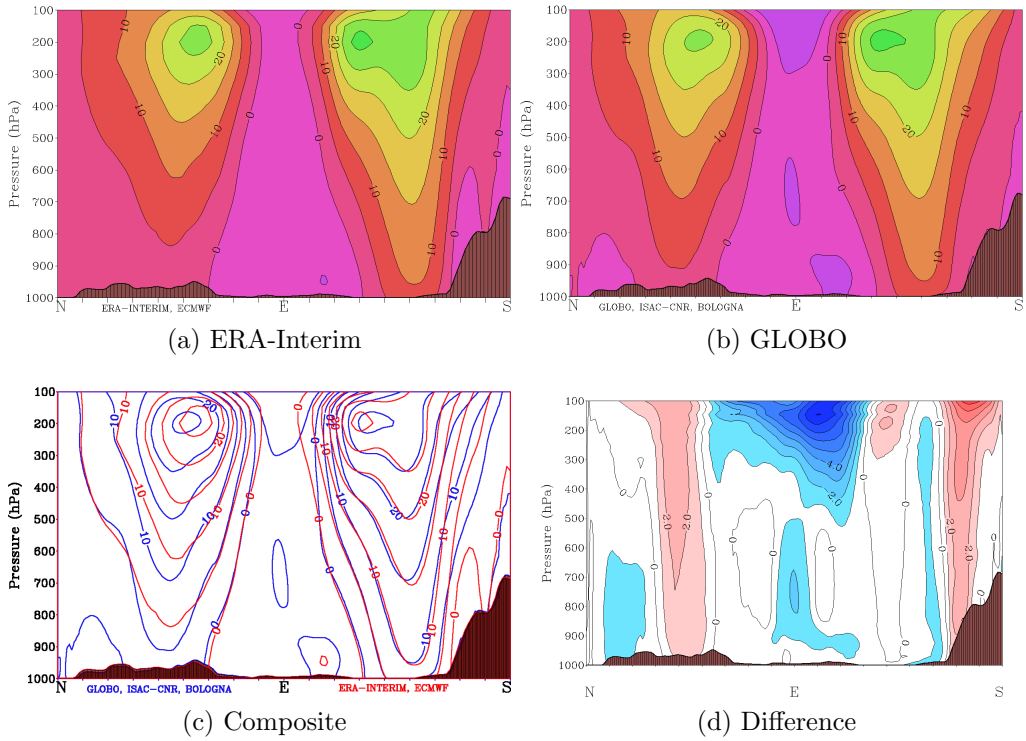

(a) ERA-Interim (b) GLOBO

(c) Composite (d) Difference

Figure 2.8: Zonally averaged annual mean zonal wind: a) Era-Interim, b) GLOBO, c) composite, and d) Difference (GLOBO - ERA-Interim). In figures a), b) and c) countour lines every 5 m/s. Blue colors in figure d) represents negative values, red colors positive values. Contour lines every 1 m/s.

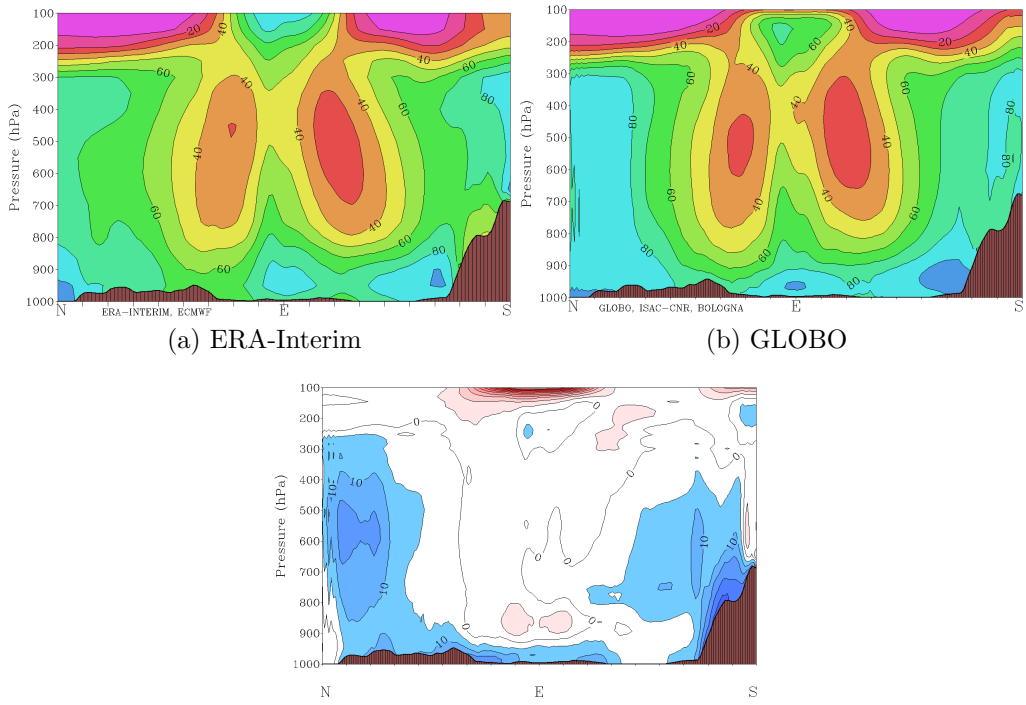

(a) ERA-Interim

(b) GLOBO

(c) Difference

Figure 2.9: Zonally averaged annual mean relative humidity: a) Era-Interim, b) GLOBO and c) Difference (GLOBO - ERA-Interim). In figures a) and b) contour lines every 10%. Blue colors in figure c) represents negative values, red colors positive values. Contour lines every 5%

2.2.3 Changes to the model and sensitivity experiments to improve systematic errors

Another test has been carried out to analyze the variability of the atmospheric circulation in terms of the geopotential height at 500 hPa, by computing Empirical Ortoghonal Functions (EOF) over the winter Northern Hemisphere. The number of years (ten) used to compute climatology (observed and simulated) resulted insufficient to estimate with sufficient precision the EOF as presented in the literature for the low-frequency variability (Corti et al., 2003). However, the first and most important EOFs simulated by GLOBO were similar to those computed using observed winter monthly data from ERA-Interim dataset, both in the spatial patterns and in the fraction of explained variance (not shown). After this first evaluation of model performance and systematic errors, a series of modifications to the model and sensitivity experiments were conducted to reduce the systematic errors. The attention has been focused on the zonal and annual mean errors of the temperature and the zonal wind component that showed a more zonal circulation and a colder simulated atmosphere than observed, as explained in the previous section. As for the "zonalization" error, it has been reduced (fig. 2.11) after developing and implementing an orographic gravity wave drag parameterization scheme. Several sensitivity tests have been conducted in order to find the proper parameter values so as to reduce significantly the zonal wind component errors. Further modifications have been made on the longwave radiation fluxes in the radiative parameterization scheme and in the implementation of the frictional heating due to the turbulence, that reduced the systematic errors in the temperature field (fig. 2.10). This first evaluation and correction of the systematic model errors for long term simulations has provided useful elements in showing the model capabilities to produce extended-range forecasts.

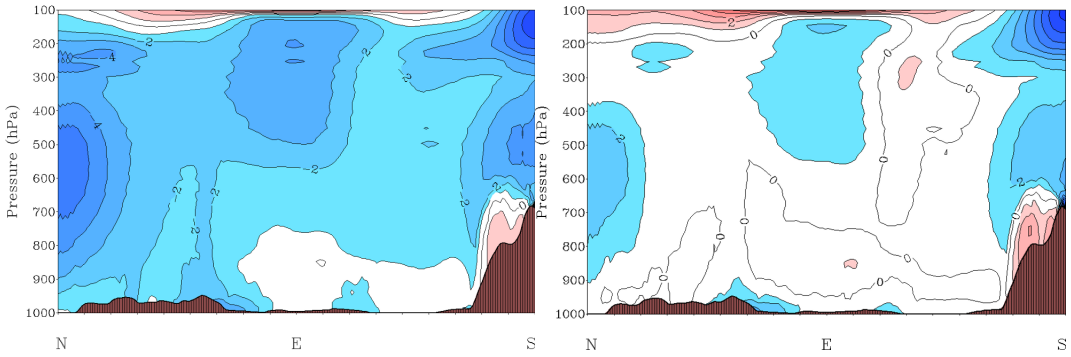

(a) before (b) after

Figure 2.10: Zonally averaged annual mean temperature difference in GLOBO model from observations (ERA-Interim): a) before, b) after the sensitivity test. Contour lines every 1 °C.

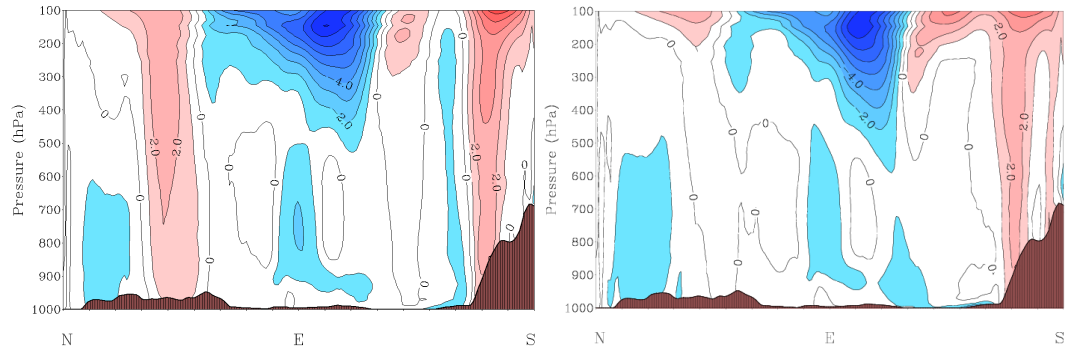

(a) before (b) after

Figure 2.11: Zonally averaged annual mean zonal wind difference in GLOBO model from observations (Era-Interim): a) before, b) after the sensitivity test. Contour lines every 1 m/s.

Chapter 3

The monthly atmospheric ensemble prediction system at the ISAC-CNR

Since 2009 the GLOBO model has been used to issue, once a month, a monthly forecast for the following 30-35 days. The implementation of the monthly forecasting system is part of the research activity of this thesis. During these years various modifications and improvements have been made in the dynamics and physics of the model. These changes improved the stability of the numerical integration, reduced problems relative to noise generation over the poles and on very high orography (Himalaya). Currently GLOBO is employed with a horizontal resolution of 1 degree in longitude and about 0.75 degree in latitude, with 50 levels. The ensemble forecast is produced using as initial conditions those of the ensemble system of GFS (Global Forecasting System) of NOAA/NCEP (USA). They consist in one un-perturbed and twenty perturbed analyses obtained with the breeding method (Toth and Kalnay, 1997). At the beginning, 21 members from GFS analysis of 00 UTC were used. Then, in order to increase the number of ensemble members,

at ISAC additional perturbed initial conditions were introduced, selected out 14 from 00 UTC and 18 from 12 UTC of the day of analysis (including both unperturbed analysis) for a total number of 32 ensemble forecast members. The choice of the day of analysis is defined on Civil Protection Department requests. As a consequence, it is not the same every month and most of the times it corresponds to one of the last ten days of the previous month, so the length of forecast period is variable from month to month.

Since the model has a systematic error, it is not possible to compute the anomaly forecast using the observed climatology. Therefore the anomaly forecast is evaluated as a difference between the forecast ensemble mean and a model climatology, created for the same time range based on the "reforecasting" technique. This model climatology is obtained using initial conditions for the same day of the forecast initial analysis, but for past years available from ERA-Interim dataset (Berrisford et al., 2009). The reference time range is the period 1989-2009. In order to increase the number of ensemble members and to have a smoother ensemble mean (and also to mitigate possible problems related to the diurnal cycle), the analysis of both 00 and 12 UTC are used also for the reforecasts, for a total number of 42 ensemble members. Figure 3.1 shows a schematic flow chart of the system, while figure 3.2 shows some products of the monthly forecasting system.

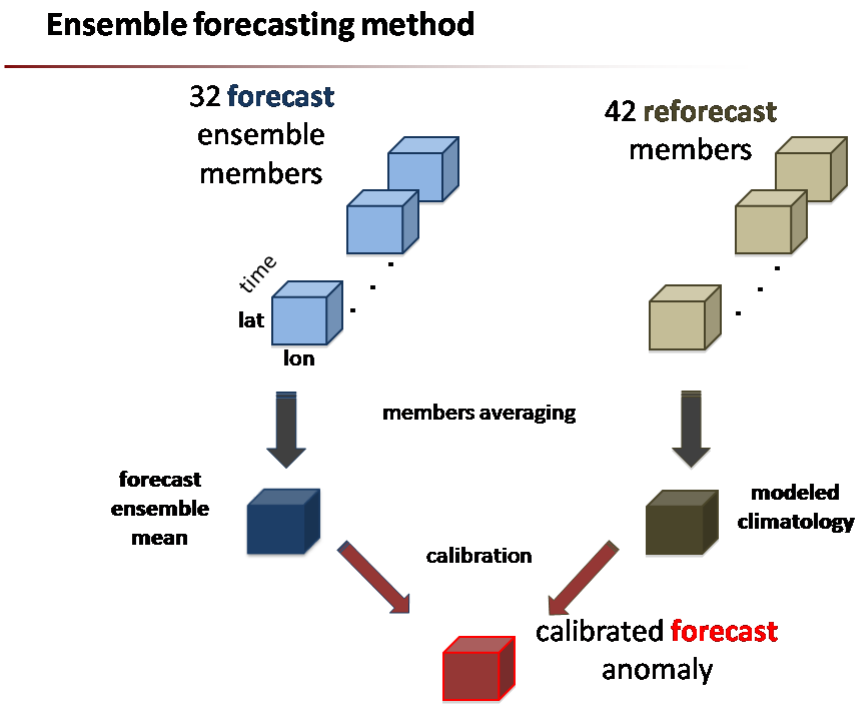

Figure 3.1: Schematic view of the anomaly forecast method (until September 2011).

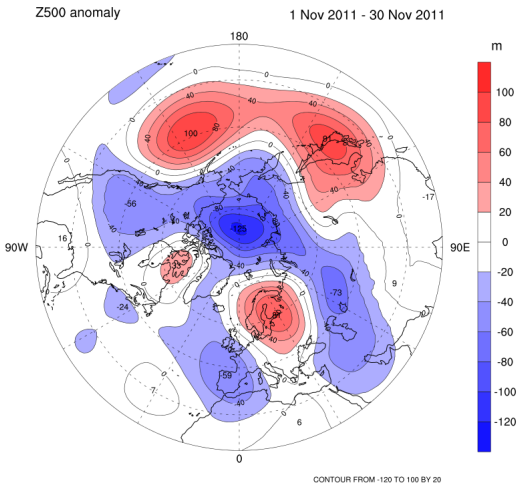

(a) Z500 anomaly field

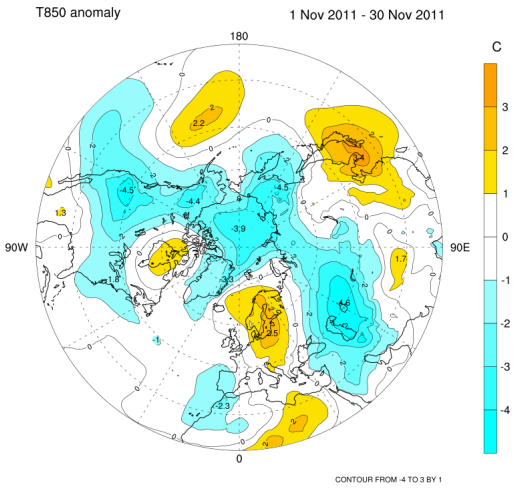

(b) T850 anomaly field

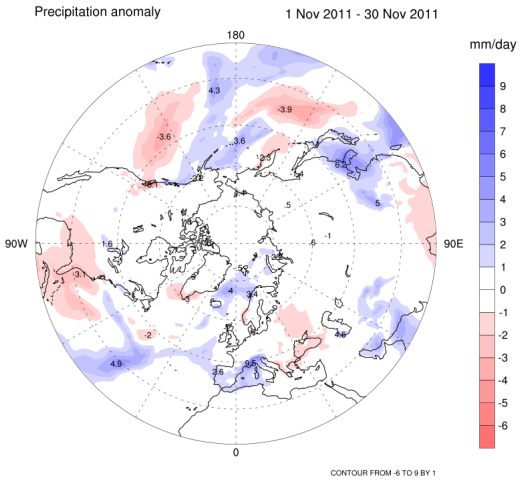

(c) Precipitation anomaly field

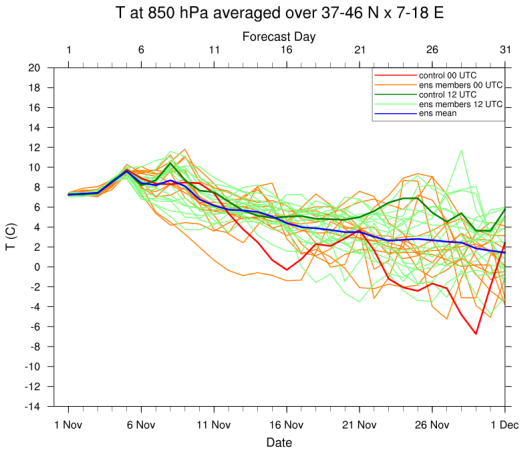

(d) T850 ensemble plume

Figure 3.2: An example set of graphical products of the ISAC-CNR monthly forecasting system, for the forecast related to November 2011.

3.1 The boundary conditions

As explained in the introduction and in the Chapter 1, predicting the atmospheric evolutions in the time scale of about 30-40 days is not only an initial value problem, but also a boundary values one. The most important boundary parameters forcing the atmosphere are sea surface temperature, sea ice cover, soil moisture, soil temperature and snow cover. In the following sections, the methods employed to treat the evolution of some of the above quantities will be illustrated.

3.1.1 Sea surface temperature

This monthly forecast system is based only on an atmospheric general circulation model , and the oceanic contribution to the atmosphere is represented by a simple mixed layer slab model in which the sea surface temperature tendency depends on the net heat surface fluxes and a relaxation term to climatology as it follows:

$$\frac{\partial SST}{\partial t} = \frac{F_{net}}{h(x,y)\rho C_P} - \gamma(SST - SST_{clim}) \tag{3.1}$$

$$\rho = 10^3 \frac{Kg}{m_3}, C_P = 4186 \frac{J}{KKg}, \gamma = \frac{1}{2.3} days^{-1}$$

$$F_{net} = SH + LH + F_{lw} - F_{sw}$$

where ρ is water density, C_P is the specific heat at constant pressure of water, γ is the relaxation parameter corresponding to a time scale of 2.3 days, SH are the sensible heat fluxes, LH are the latent heat fluxes and $F_{lw,sw}$ are respectively the longwave and shortwave radiation fluxes. The parameter $h(x,y)$ represents the mixed layer depth. It is defined as a climatological annual cycle of 10-day means (for a total of 36), averaged over the period 1941-2008 (de Boyer Montegut et al.,

2004) and variable in the space. SST_{clim} represents a combination of the initial SST anomaly and the SST climatology for the period 1989-2008, based on ERA-Interim dataset. The initial SST anomaly decays slowly during the integration. It is reduced by about 15% at the end of the forecast run. In the same way as the mixed layer depth, the SST climatology consists of an annual cycle of 10-day means so as to simulate the internal monthly variability of the predicted sea surface temperature.

3.1.2 Sea ice cover

There is no sea ice dynamical model coupled with the GLOBO model. The sea ice cover in the initial conditions is kept constant up to the first update of the SST climatology, then a climatological tendency every ten days is applied to simulate sea ice evolution. These climatological tendency values are also extracted from the ERA-Interim dataset. Sometimes, during the forecast integration, there is the formation of areas with no sea ice cover where it should be present. This happens when there is an extremely small sea ice cover extent in autumn or when there are problems with the satellite data retrieval. Therefore an aggregation algorithm has been applied in order to fill these areas with sea ice. It consists in a spatial filter that is iterated until the value of sea ice cover in a given point reaches the mean value of surronding grid points.

3.1.3 Soil moisture and temperature

The soil model inside GLOBO has been described in chapter 2 and it has 4 vertical levels. The deepest one contains a forcing climatology both for temperature and moisture. These climatologies are defined by 10-days averages for the period 1989-2008 from the ERA-Interim reanalysis dataset. The variables are set at the beginning of the forecast run equal to their climatological values and no anomaly

is calculated or taken into account.

3.2 The model climatology and the anomaly products

The model climatology is composed of a dataset of reforecasts. These reforecasts are produced with the same set-up imposed on the forecast runs, with the purpose to mantain uniformity as much as possible between the two sets of runs for the anomaly forecast computation.

The final products are predicted anomalies, calculated as difference between forecast ensemble mean and reforecast ensemble mean, of the most important atmospheric parameters, i.e. geopotential height at 500 hPa, temperature at 850 hPa and total daily precipitation. They are computed over the Northern Hemisphere as time averages for the first half (or first 15-days period), second half of the month and for the full month. Ensemble mean time series are also computed averaging over Italy, showing daily values and ensemble spread.

Since September of 2011, the reforecasts are not anymore initialized with the same day of forecast initialization. A new method has been introduced as follows: a set of 24 42-members of reforecasts has been run starting from the 1st and the 15th day of every calendar month. Then a gaussian weighting function with a standard deviation $\sigma = 1.5$ months has been applied on the dataset, centering it on the reforecast month closer to the day of forecast initialization. The new scheme is represented in figure 3.3. With this method, a smoother model "climate" has been obtained to be used as reference.

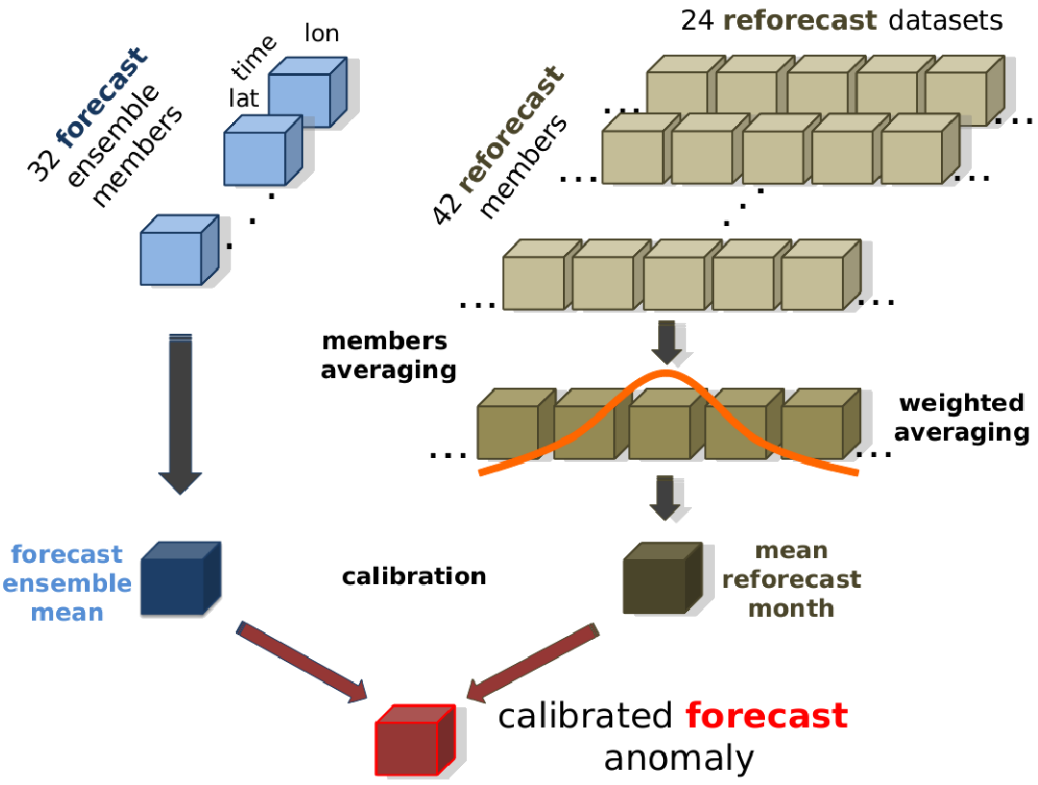

Figure 3.3: Schematic view of the new anomaly forecast method (after September 2011)

3.3 Statistical verification

A forecast verification is required to assess the performance of the model. Given the probabilistic nature of the monthly forecast, this verification must be done in probabilistic terms too. Therefore a large number of ensemble forecasts is necessary to obtain valid statistics.

The first monthly forecasts produced were verified only qualitatively. The predicted anomaly patterns were compared visually with the observed ones using NCEP reanalyis, available in near real-time, or using ERA-Interim reanalysis (released with a 2 months delay). The results showed, much as expected, a good match in the first 2 weeks, when the deterministic signal is very strong, and a poor skill in the second part of the month. However, a more quantitative verification was necessary, so a method of forecast verification has been recently set up using some statistical indices like the Root Mean Square Error (RMSE) and the uncentered Anomaly Correlation (AC, Wilks, 2006). The RMS forecast error is defined as:

$$RMSfe = \sqrt{\frac{1}{M}\sum_{i=1}^{M}(f_i - o_i)^2} \tag{3.2}$$

where M is the number of grid points considered, f is the forecast ensemble mean and o is the observed field. The RMS systematic error is defined as:

$$RMSse = \sqrt{\frac{1}{M}\sum_{i=1}^{M}(r_i - c_i)^2} \tag{3.3}$$

where r is the reforecast ensemble mean and c is the reference climatology for the predicted month, extracted from ERA-Interim over the period 1989-2009. The anomaly correlation is defined as:

$$AC = \frac{\sum_{i=1}^{M}[(f_i - c_i)(o_i - c_i)]}{\sqrt{\sum_{i=1}^{M}(f_i - c_i)^2}\sqrt{\sum_{i=1}^{M}(o_i - c_i)^2}} \tag{3.4}$$

In the last equation the comparison of the forecast anomaly with the observed one is "raw", because the forecast retains its bias. Therefore, it is possible to compute the AC for a calibrated anomaly forecast using the model climatology r since $c = r + b$, where b is the model climatology bias, which is variable in time and different for each model grid point. Figure 3.4 shows the daily systematic error (eq. 3.3) of the reforecast dataset for the geopotential height at 500 hPa in the two hemispheres, averaged over the period August 2010 to August 2011: this is comparable with the systematic errors from other models (Vitart, 2004), saturating after 10-15 days near the value of 40 meters, and it is larger in the Southern Hemisphere. The weighted RMSE is built using weighted reforecast as explained in last paragraph of the previous section. With this method the RMSE is reduced with respect to the old method. This can be due to a better representation of the climate obtained with the weighted reforecast than that achieved with a single reforecast dataset per month. Figure 3.6 shows the daily anomaly correlation and the daily forecast error averaged over the period August 2010 to August 2011 for both the hemispheres. The AC drops dramatically under the threshold value of 0.6 after 8 days in the NH and 7 days in the SH and tends asymptotically to 0.2: in both cases the AC calculated with the weighted calibration shows less skill than that calculated with the "raw" forecast anomalies, and this is more evident in the Southern Hemisphere. This means that the representation of climate with the weighted reforecasts has still a large bias with respect to the observed one, probably due to a low number of ensemble members and a limited reforecast dataset. As for the forecast error, it increases up to 10 days, reaching the same value of the climatology, around 100 m. Nevertheless, in order to achieve robust statistics it is necessary to produce a large number of cases, and these values represent only a very preliminary estimate of the potential skill of the ISAC monthly forecasting system.

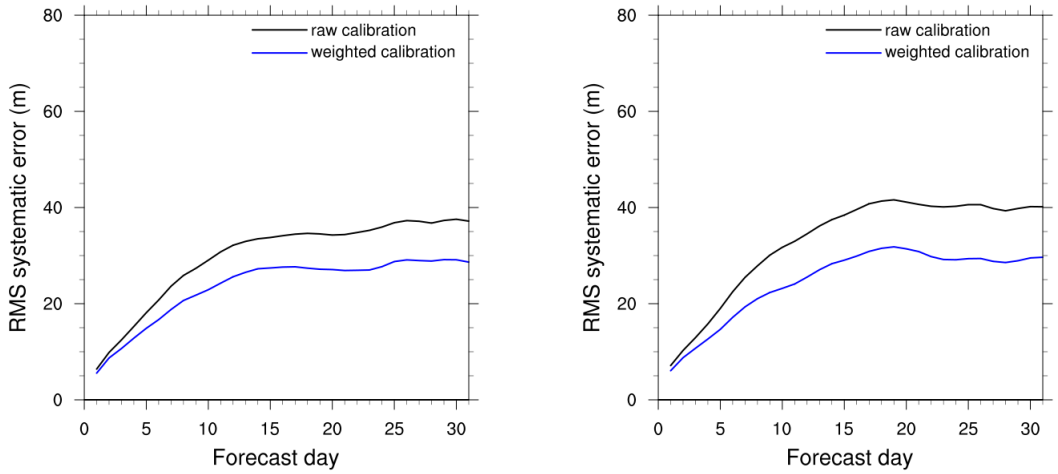

(a) Northern Hemisphere (20N–80N) (b) Southern Hemisphere (20S–80S)

Figure 3.4: Daily RMSE of the geopotential height at 500 hPa reforecast ensemble mean for both the hemispheres.

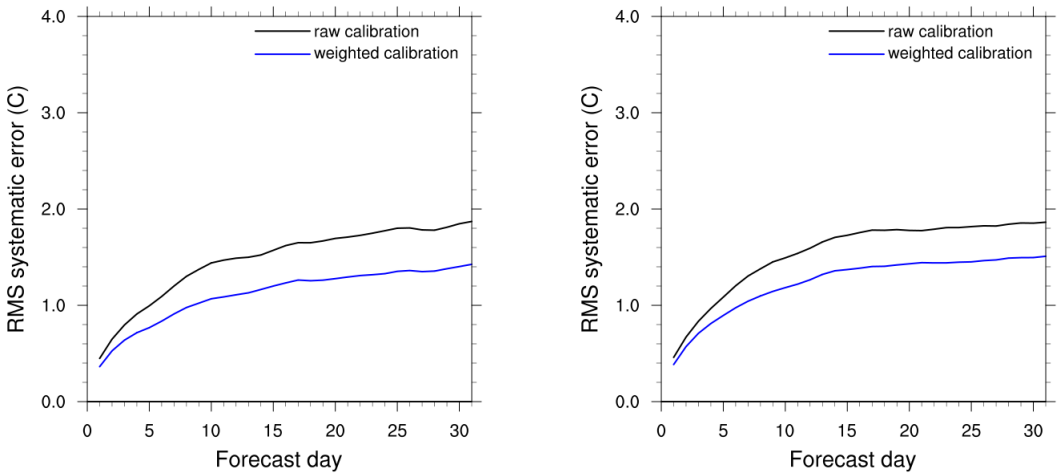

(a) Northern Hemisphere (20N–80N) (b) Southern Hemisphere (20S–80S)

Figure 3.5: Daily RMSE of the temperature at 850 hPa reforecast ensemble mean for both the hemispheres

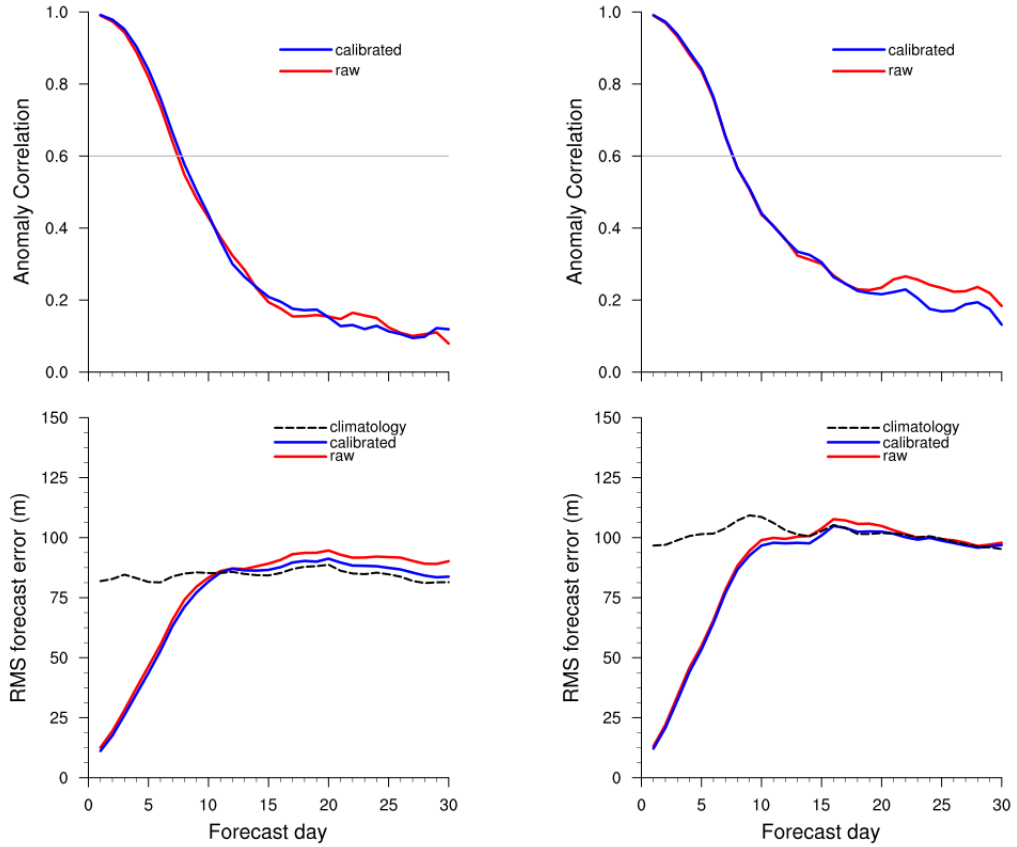

(a) North Hemisphere (20N–80N) (b) South Hemisphere (20S–80S)

Figure 3.6: Daily Anomaly Correlation of the geopotential height at 500 hPa forecast ensemble mean for both the hemispheres (top panels) and daily Root Mean Square of forecast error for the same variable compared to climatology (bottom panels).

Chapter 4

The new ocean definition in GLOBO

The flux corrected version of the slab ocean model

In chapter 1, we discussed the possible modelling solutions to be adopted for the representation of SSTs. After the examination of the various possibilities, it was decided to implement a modified version of the operational slab mixed layer model. As a consequence, equation 3.1 has been modified, adding a flux correction term and changing the values of some parameters. The new equation predicting the SST evolution is:

$$\frac{\partial T}{\partial t} = \frac{F_{net} + O_{res}}{\rho C_P h(x,y)} - \gamma \left(T - T_{clim}\right). \tag{4.1}$$

$$O_{res} = \Delta Q_{clim} - \Delta Q_{flux}$$

Variable O_{res} is a "flux correction" term representing the residual heat fluxes due to the internal ocean dynamics (see below). The relaxation parameter γ has been set to represent an inverse time scale of about 23 days. The specific heat C_P has been set to 3930 $JKg^{-1}K^{-1}$ and the density ρ has been fixed to 1026 Kg/m^3. The

last two quantities are mean values for sea water used in the literature (see Neale et al., 2010, chapter 5).

The residual fluxes O_{res} are computed as follows: the reforecast members are forced using observed daily SST and sea ice cover from the ERA-Interim dataset for the period 1989-2009 and for the month of interest. The net surface heat fluxes are saved as output during model runs (but only for the members starting with initial conditions at 00 UTC), to create a model flux climatology ΔQ_{flux} for the particular month, defined in terms of 10-day means. This climatology is subtracted from the corresponding climatological heat fluxes ΔQ_{clim}, obtained from the climatological 10-day mean SST tendency for the same month (still from the ERA-Interim dataset).
The flux correction is a technique often used in coupled models for climatic simulations. It has been applied to test its validity in this shorter time scale.

Model and experiment setup

The forecast run is set up in this way: the initial SST field is kept persistent until day 5 of the calendar month we are simulating, in order to mantain the initial anomaly for the first period of the forecast. From day 5, the SST evolution starts, based on equation 4.1. The initial SST anomaly, that forms the combined SST forcing as described in chapter 3, decays slowly to climatology by a fraction of 5% each time, at calendar days 1, 11 and 21, as in the operational case. The residual fluxes O_{res} are updated at days 15 and 25 of calendar months. The initialization day is chosen from one of the last ten days of the previous month (see the introduction at chapter 3). This is another reason to use the persistence of the initial SST. Infact, the residual fluxes and, as a consequence, the model flux climatology are required for the last ten days of the month of the initial analysis in order to start the evolution of the SST from the first time step. This implies that the reforecasts should start from the 20th day of the month of the initial analysis. However in

this way the method of calculation of the anomaly forecasts would differ from the old operational one (the new operational method uses a weighted average of the reforecasts, see chapter 3) and therefore the comparison would not be uniform.

The predicted anomalies are computed by subtracting the reforecast ensemble mean of each variable of interest, calculated from the reforecast dataset forced with daily observed SST and sea ice cover data, from the forecast ensemble mean produced with the new model. For the numerical experiments several months of 2011 have been simulated, and the SST and the atmospheric fields (geopotential height at 500 hPa, temperature at 850 hPa and precipitation) have been compared.

4.1 Results of the experiments

4.1.1 SST differences

Figures 4.1 - 4.2 show some examples of the evolution of the sea surface temperature predicted in selected areas of the global oceans in different months. The SST simulated with the operational slab model shows very little spread among the members. It shows also an unrealistic trend in which "jumps" are clearly visible at the instants in which SST climatology is updated. This is due to the too short relaxation time scale (about 2.3 days), that was set up originally in order to avoid the temperature drift from observed climate. The SST simulated with the new equation shows persistence until day 5 as requested, then temperature evolves with a larger spread of the ensemble plume with respect to the operational case and with larger variability due to the weather. Note that SST is plotted from the day 1 of the predicted calendar month, that does not coincide with the initial analysis. The observed SST used as reference is obtained from the ERA-Interim dataset.

A comparison of the two models in terms of forecast errors against observations has been made by computing monthly averaged SST ensemble means. We first

used the observed SST monthly means from the NOAA Optimal Interpolation SST Analysis (version 2) dataset (Reynolds et al., 2002), released in near real time. Later, data from the ERA-Interim dataset have been used for comparisons. Figures 4.3 – 4.6 show the forecast error patterns for some of the simulated months using the ERA-Interim observed SST (the results are similar to those obtained with OISST dataset). The averaged root mean square error (RMSE) and mean absolute error (MAE) are reported as well, computed in the range of latitudes from 60S to 60N. The forecast error patterns of the new model are similar to those of the operational model, even though individual months RMSE and MAE are similar or slightly larger for the new model than those obtained with the operational model (except for March 2011). The larger RMSE and MAE of the new model can be attributed to the increased SST ensemble spread, which allows a larger variability of the ensemble mean.

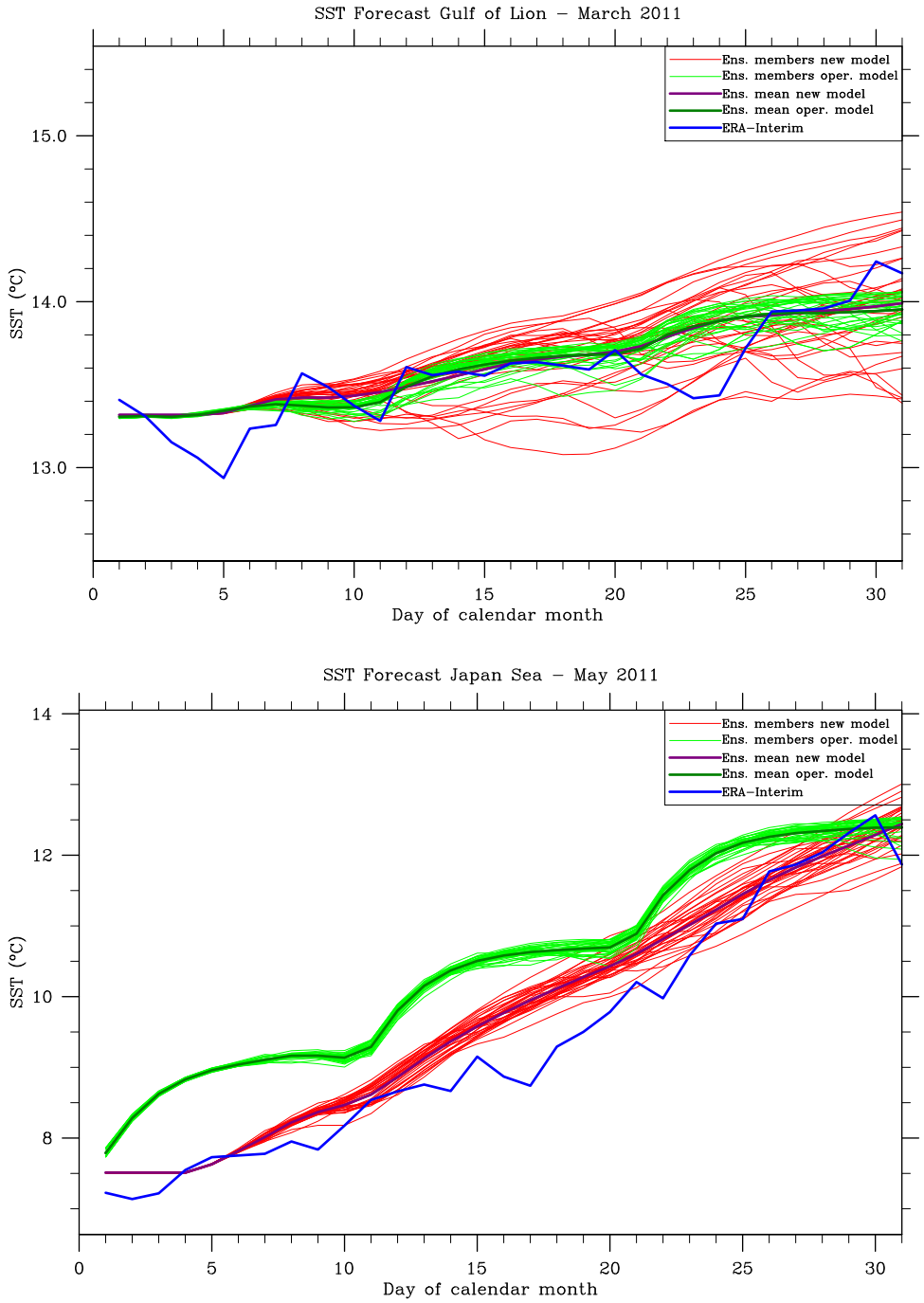

Figure 4.1: Plume of daily SST forecasts in the Gulf of Lion in March (top) and Japan Sea in May (bottom) for year 2011, with the operational slab ocean model (thin and thick green lines) and the new model (thin and thick red lines).

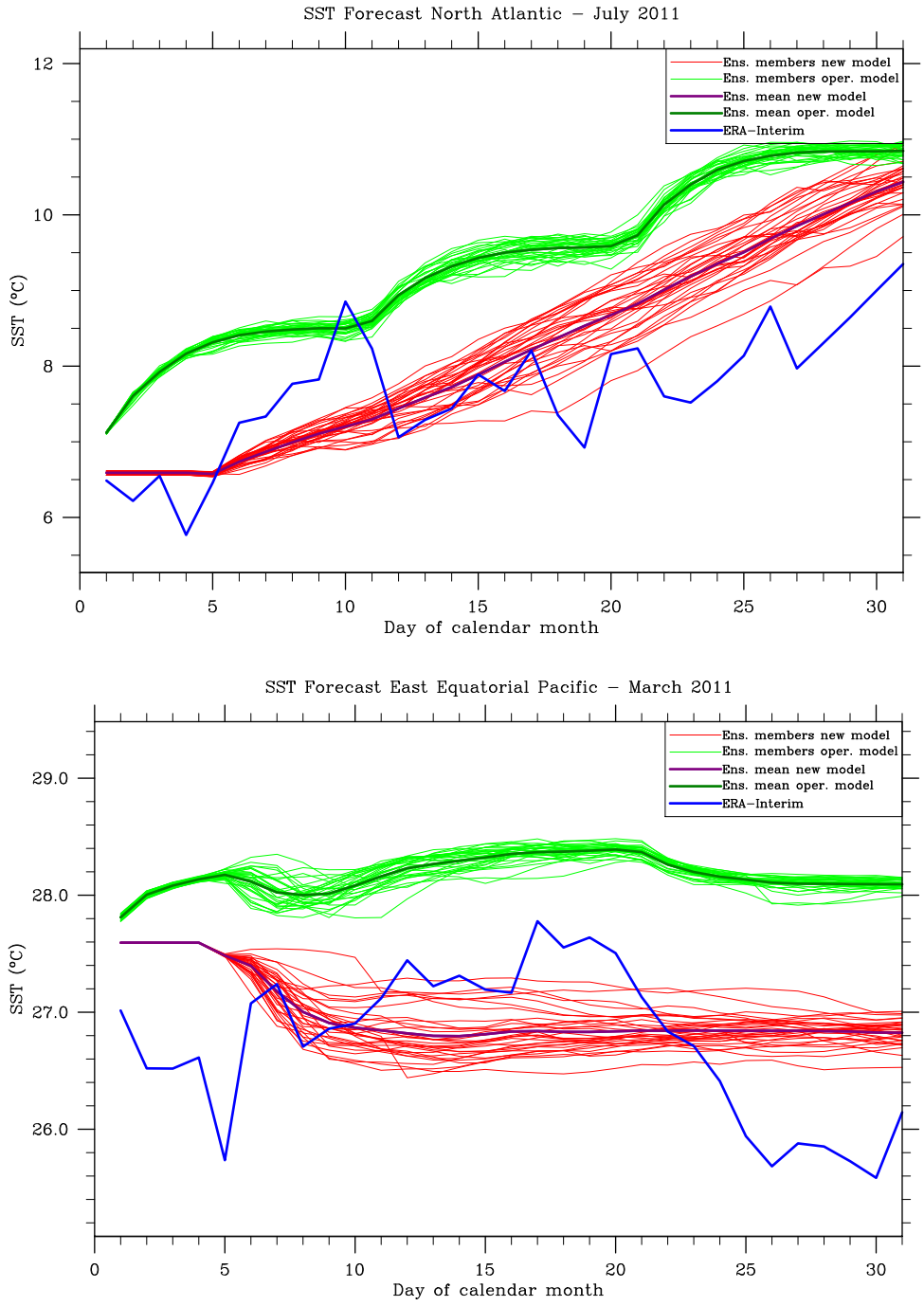

Figure 4.2: The same as fig. 4.1 but in the North Atlantic in July (top) and East Equatorial Pacific in March (bottom) for year 2011.

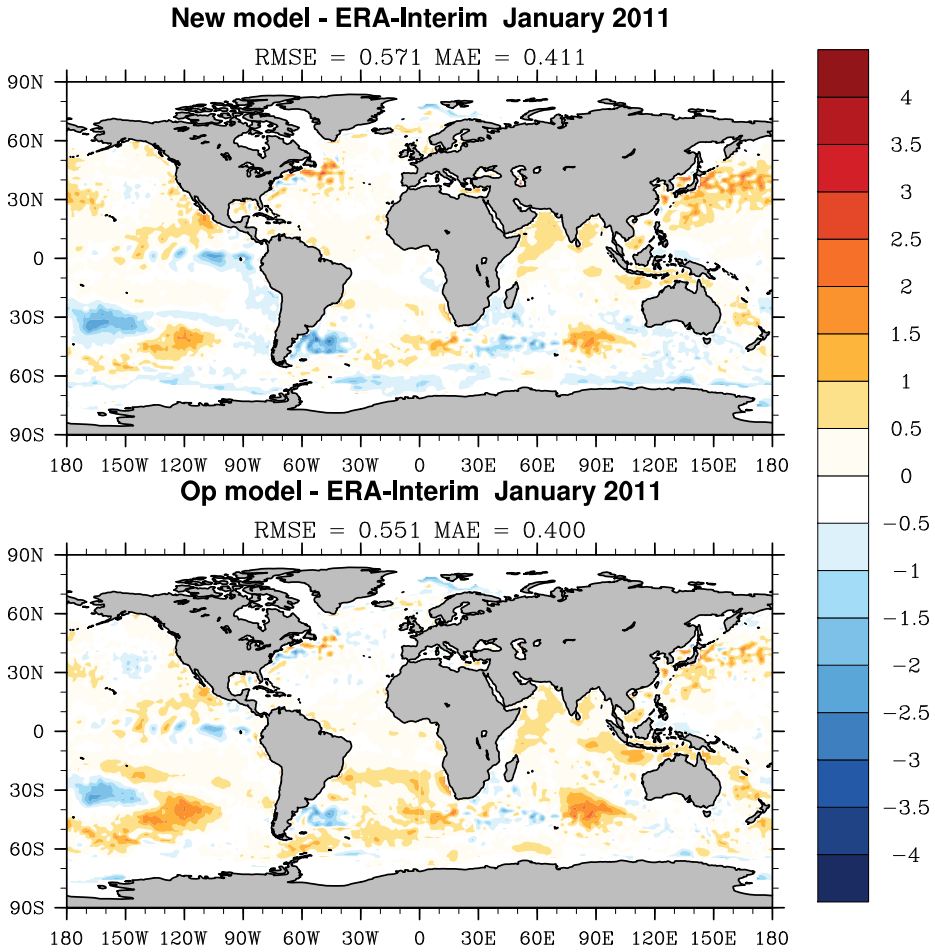

Figure 4.3: Global distribution of the monthly ensemble mean forecast error of SST in January 2011. The top panel refers to the new model, the bottom panel to the operational model. Also reported the root mean square error (RMSE) and the mean absolute error (MAE) averaged in the area 60S – 60N.

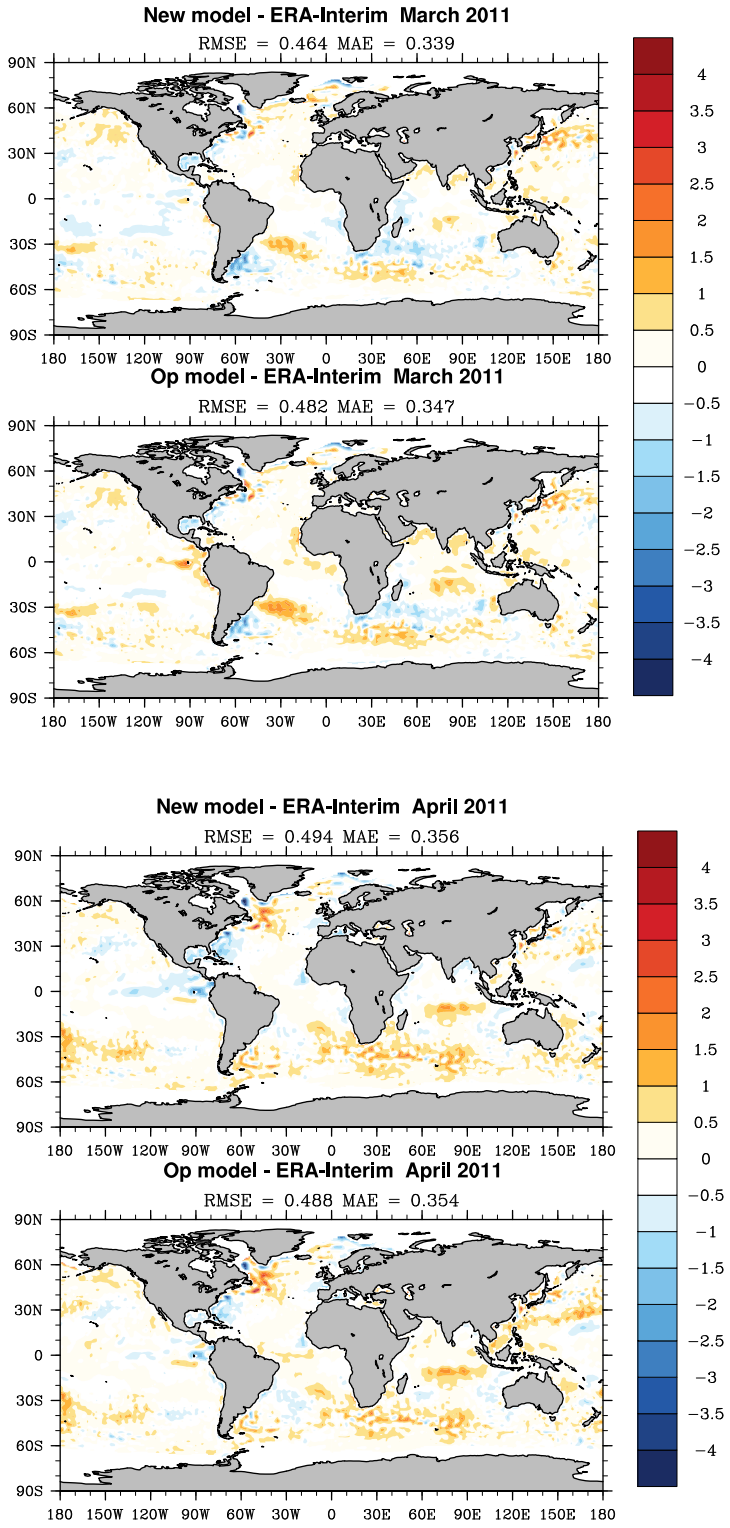

Figure 4.4: As in figure 4.3, but for March 2011 (top) and April 2011 (bottom).

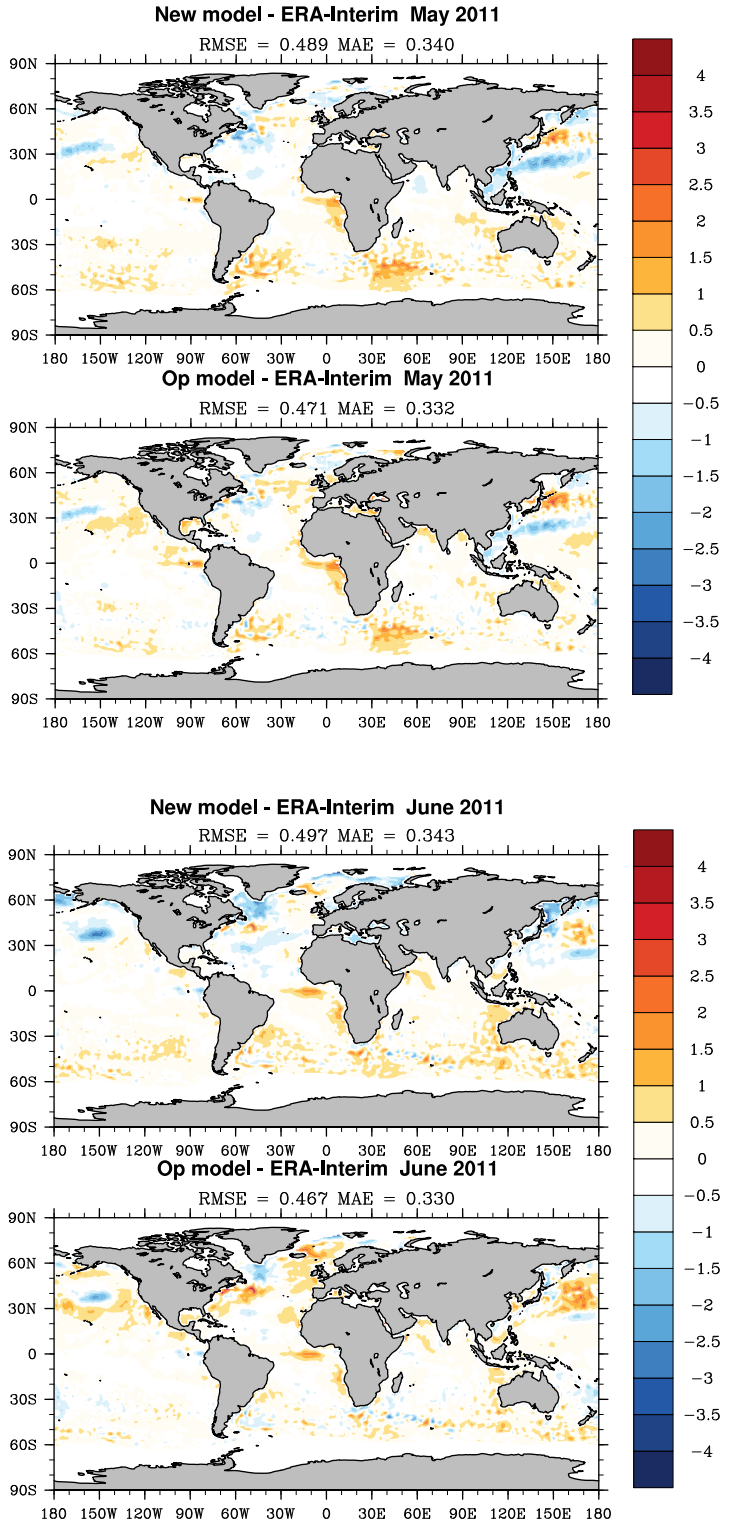

Figure 4.5: As in figure 4.3, but for May 2011 (top) and June 2011 (bottom).

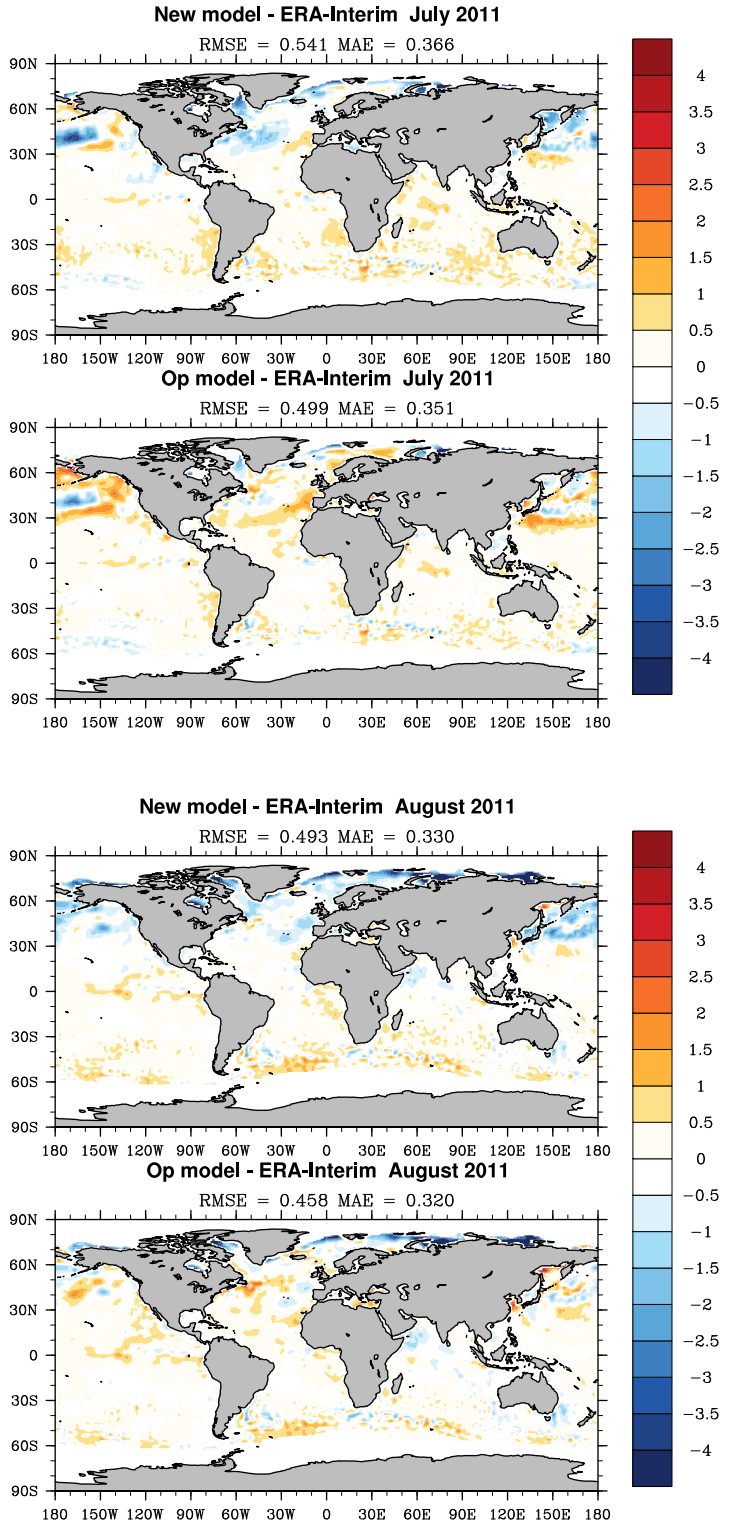

Figure 4.6: As in figure 4.3, but for July 2011 (top) and August 2011 (bottom).

The temperature differences between the two model forecasts in terms of global distribution of the ensemble means are showed in figures 4.7–4.13. The most noticeable feature is that the new model produces colder temperatures in the tropical belt (of the order of 0.5°C), and warmer (colder) temperatures in the winter (summer) hemisphere. Moreover, the differences are larger mostly in the first part than in the second part of the month. This is due probably to the initial persistence of SST in the first days as applied in the new method, that temporarily increases the difference between the two ensemble means (see fig. 4.1).

The same difference analysis has been made for the two reforecast datasets, the operational one that uses the operational version of the slab model (see eq. 3.1) and the one that is forced with daily observed SST data. This comparison has been made to check if there are differences that arise using the ocean model instead of a forcing of daily observed SST and sea ice cover data. Figures 4.14–4.20 show that the difference patterns are similar to those of the forecasts previously displayed, altough the amplitudes are smaller (about 0.2 °C). The differences show that negative values prevail on positive values. This means that globally the operational ocean model tends to produce warmer sea surface temperature than climatology.

The ensemble forecast spread of the SST produced by the new model has been compared with the observed variability of the SST computed from the ERA-Interim dataset. In both cases, equation 4.2 has been used to compute the spread at each grid point. The term $\overline{SST}^{j}_{15}$ represents the SST predicted by individual ensemble members j averaged over a period of 15 days (15-day average of observed SSTs for the same month of past years), relative to the second part for the month of interest, while the term $\overline{SST}_{15}$ represents the 15-day average of the ensemble forecast mean of the SST (climatological 15-day mean), still relative to the second part of the month. N is the number of ensemble members (number of years). The first part of the month is not considered because of the persistence that limits the initial

spread.

The results indicate that the ensemble forecast spread σ_{SST15} of the new model, defined as:

$$\sigma_{SST15} = \sqrt{\frac{\sum_{j=1}^{N} \left(\overline{SST}^{j}_{15} - \overline{SST}_{15} \right)^2}{N}} \tag{4.2}$$

is in general still smaller than the observed variability, especially in the Equatorial Pacific. This happens because in this region there are strong sources of variability with long time scales, like the El Nino Southern Oscillation (ENSO, not shown).

Therefore the SST spread has been analyzed in terms of internal variability, still in the second part of the month. By the term "internal variability" we intend the mean difference of daily SST values of a definite period (in this case 15 days) from the SST value averaged over the same period. The internal variability has been computed for each grid point with the following formula:

$$\sigma_{SST15} = \sqrt{\frac{\sum_{j=1}^{N} \sum_{i=1}^{15} \left(SST_i^j - \overline{SST}^{j}_{15} \right)^2}{N \cdot 15}} \tag{4.3}$$

where SST_i^j represents the predicted daily SST in the second part of the month of each ensemble forecast member j (observed daily SST for the year j), while $\overline{SST}^{j}_{15}$ and N have the same meaning as the terms in equation 4.2.

Even in this case, the internal variability produced by the new model is in general still smaller than observed. However, differences are very small and there is a good agreement between the two quantities. Especially from April to July in the Northern Hemisphere, the distribution of spread values are very similar, indicating that the new model is able to reproduce correctly the internal monthly variability (see as example fig. 4.21).

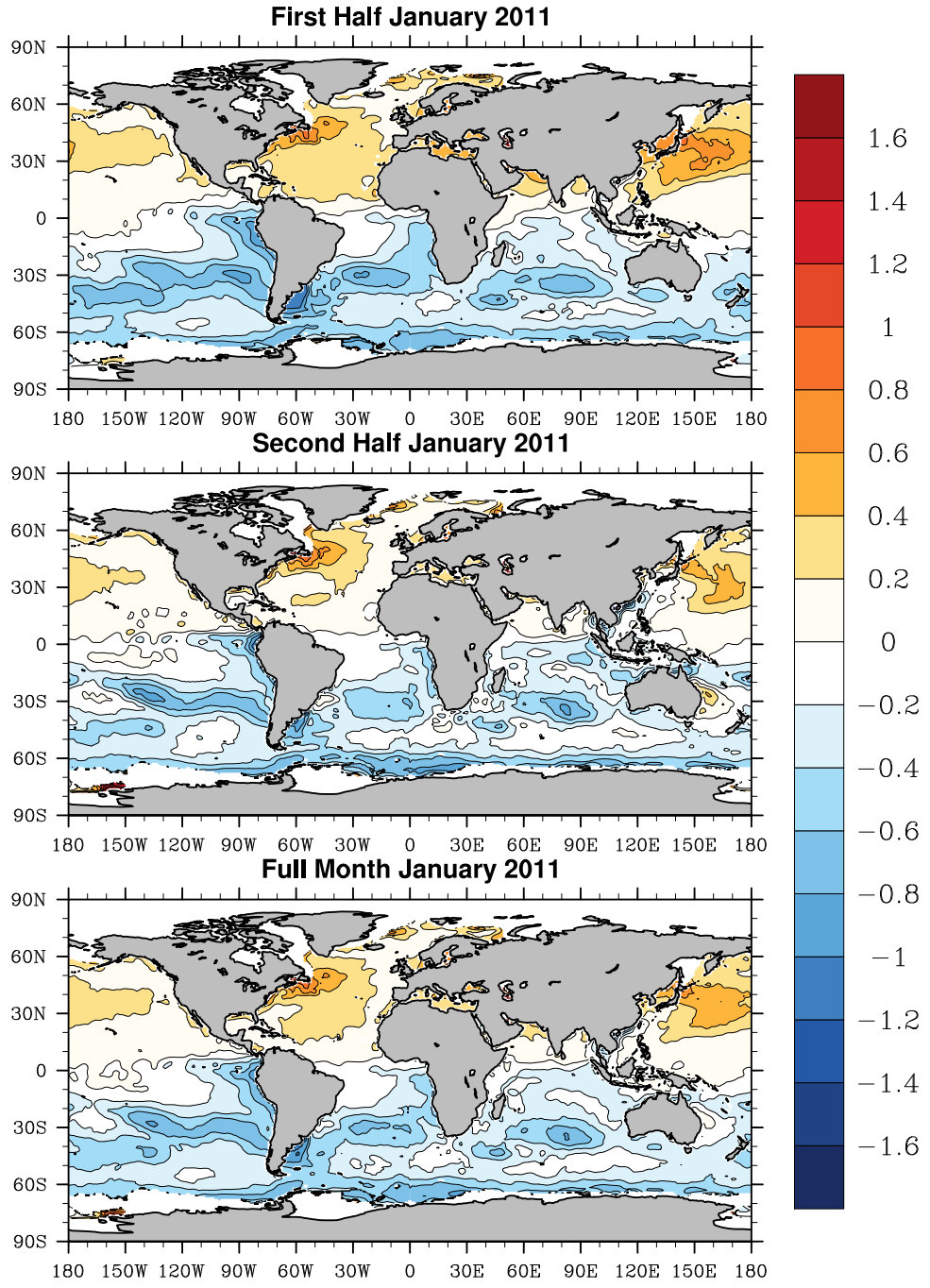

Figure 4.7: Differences in monthly global forecast ensemble mean of SST in January 2011 between the two models (new minus operational). The top panel refers to the first fifteen days, the middle panel to the second fifteen days and the bottom panel to the full month. Values are in degrees Celsius.

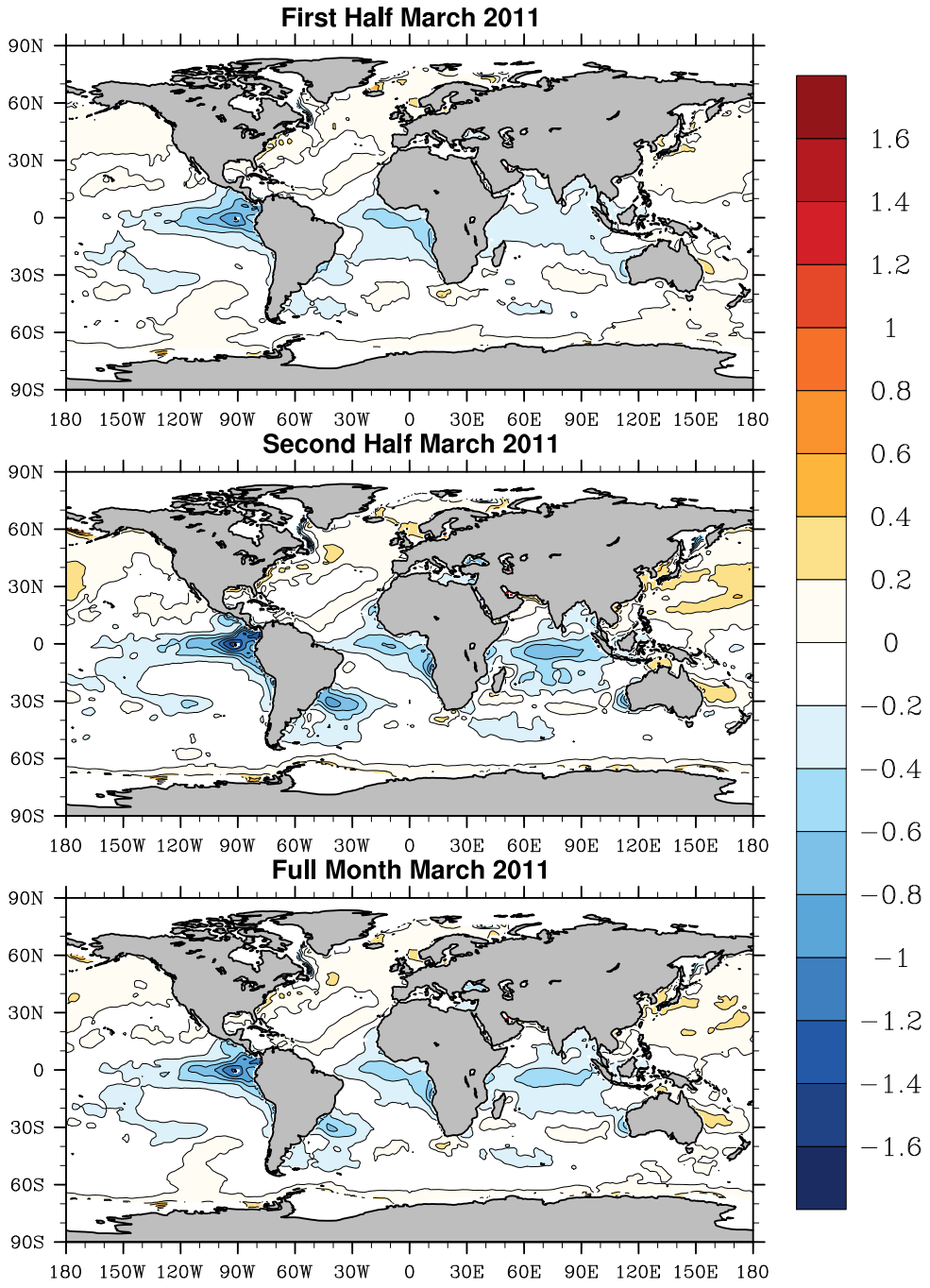

Figure 4.8: As in Fig. 4.7 but for March 2011.

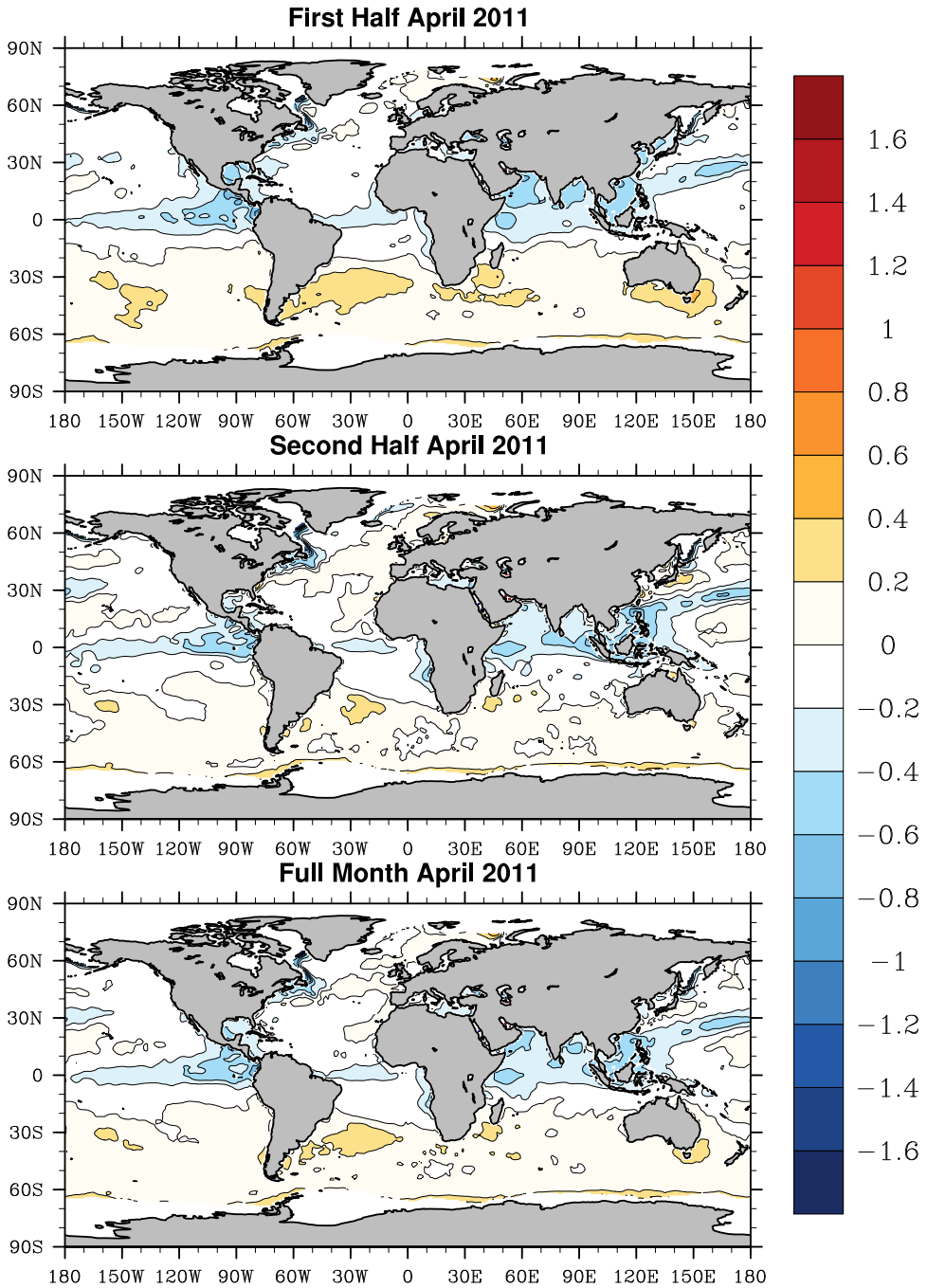

Figure 4.9: As in Fig. 4.7 but for April 2011.

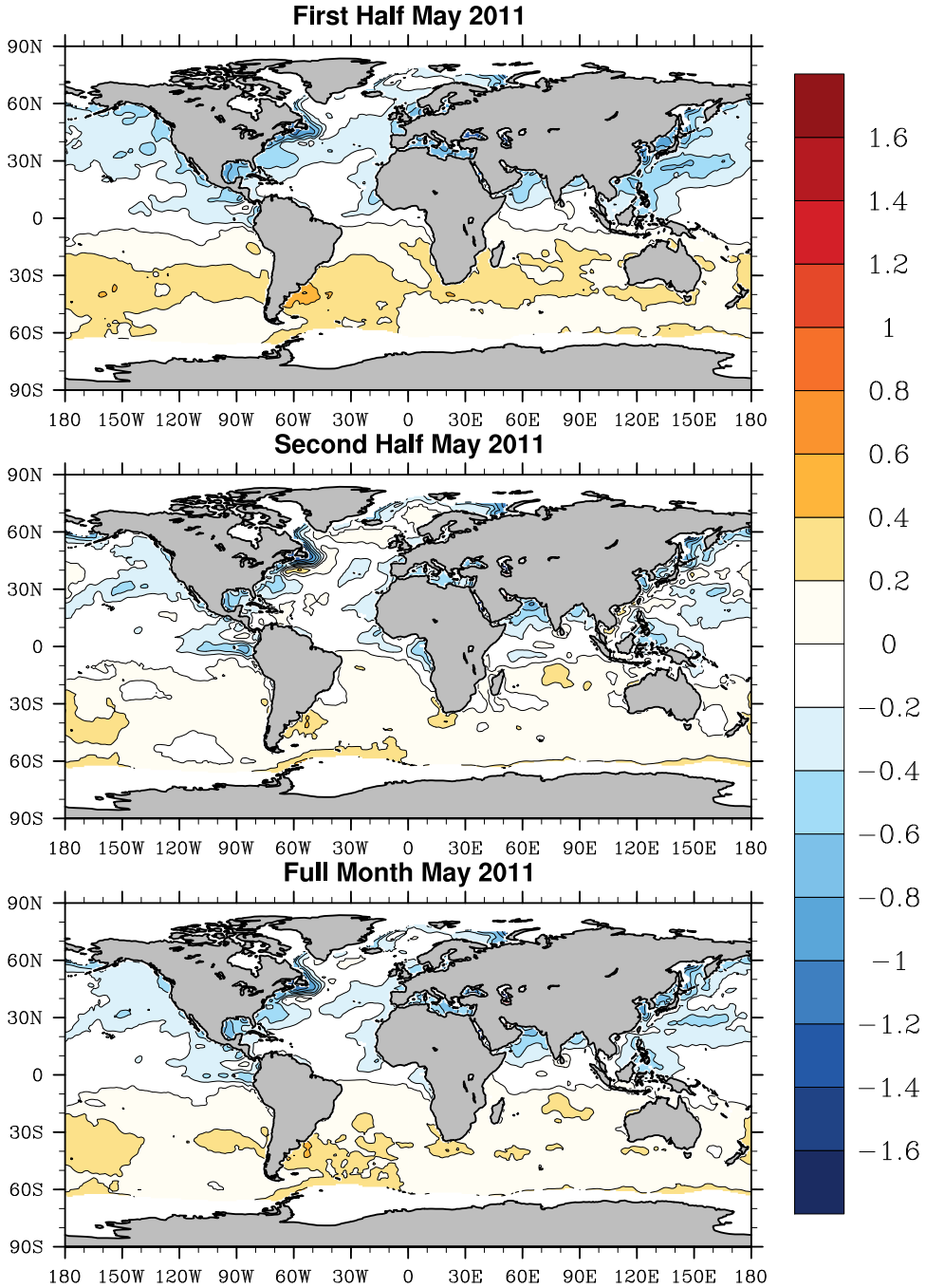

Figure 4.10: As in Fig. 4.7 but for May 2011.

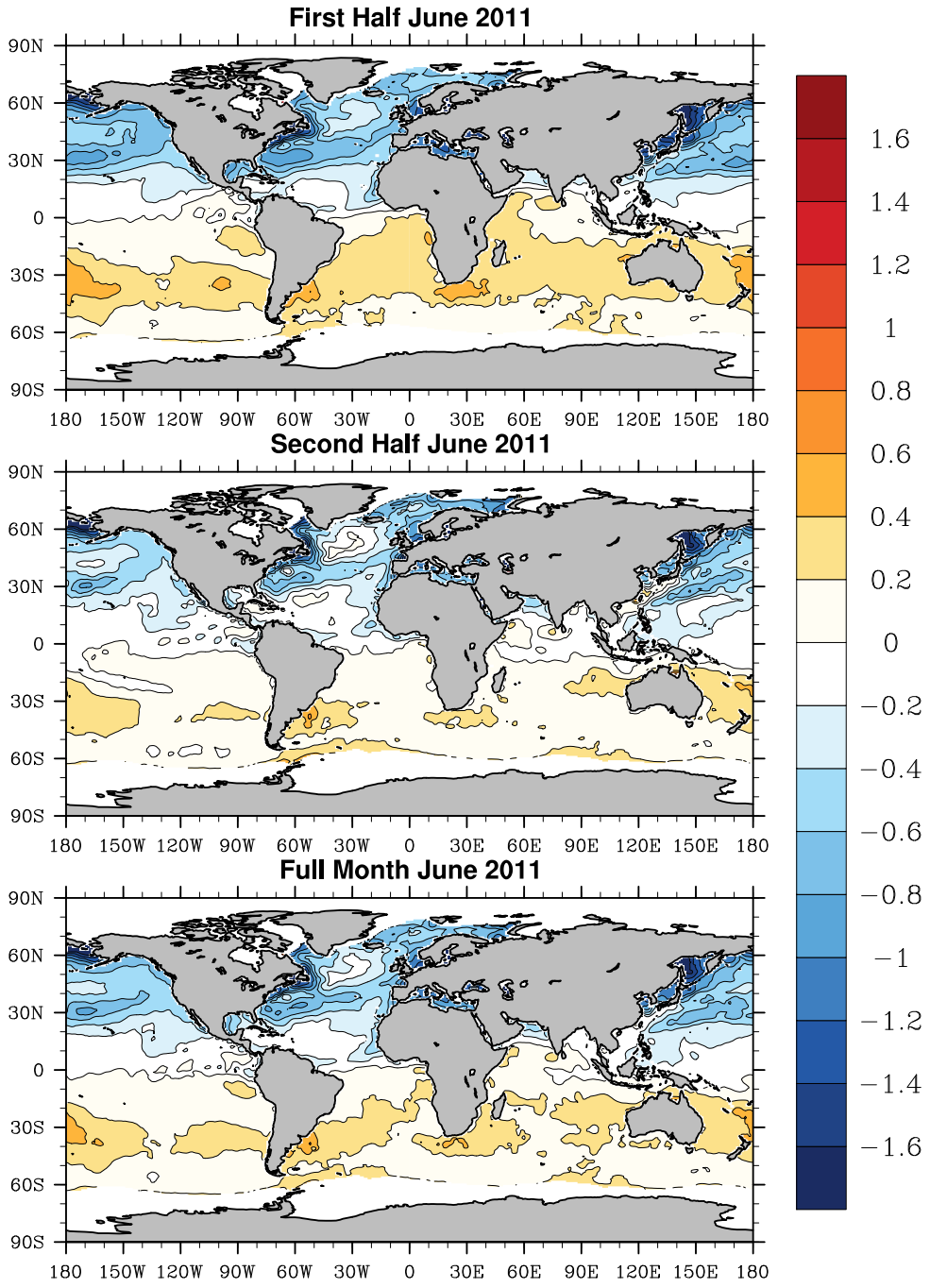

Figure 4.11: As in Fig. 4.7 but for June 2011.

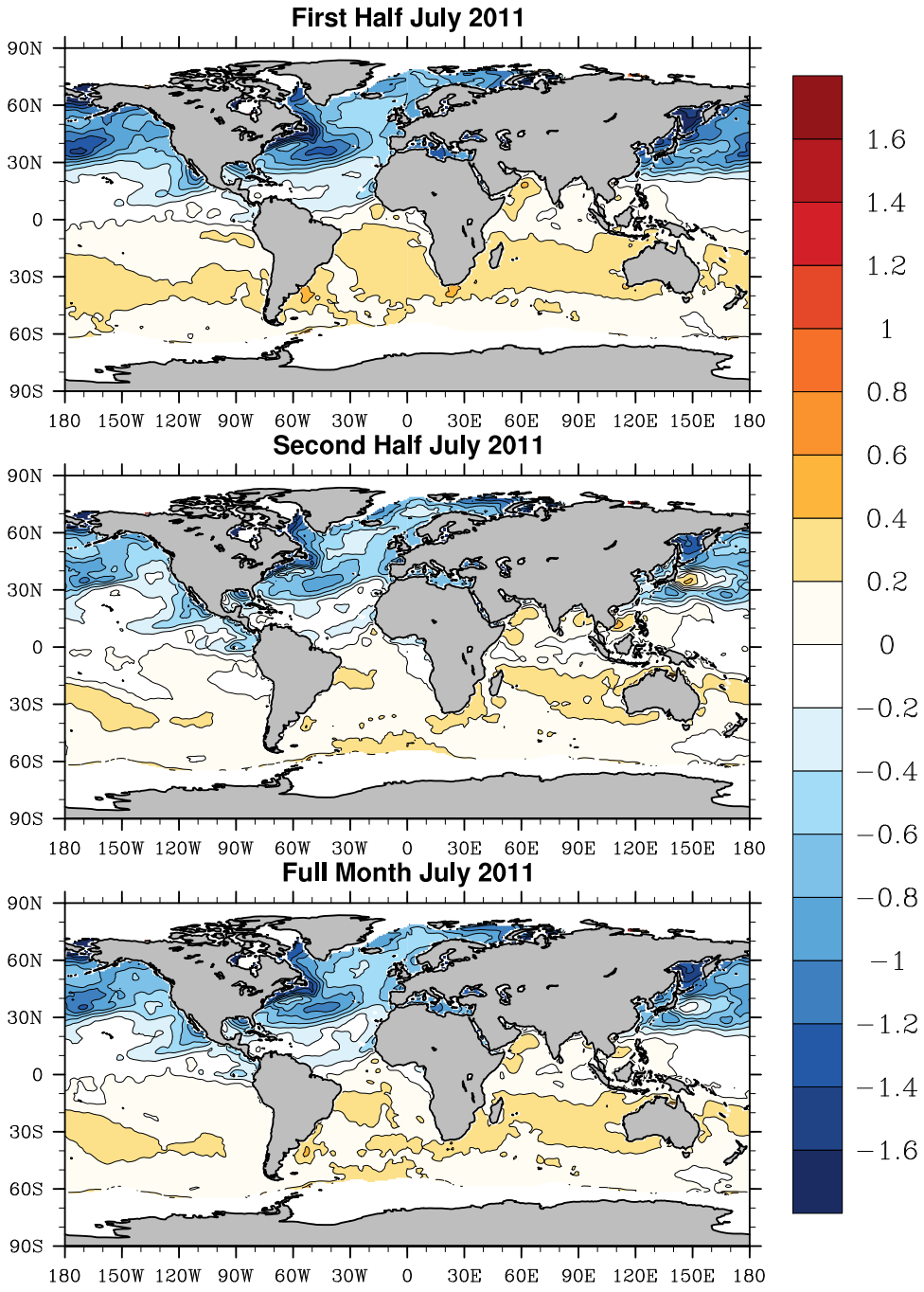

Figure 4.12: As in Fig. 4.7 but for July 2011.

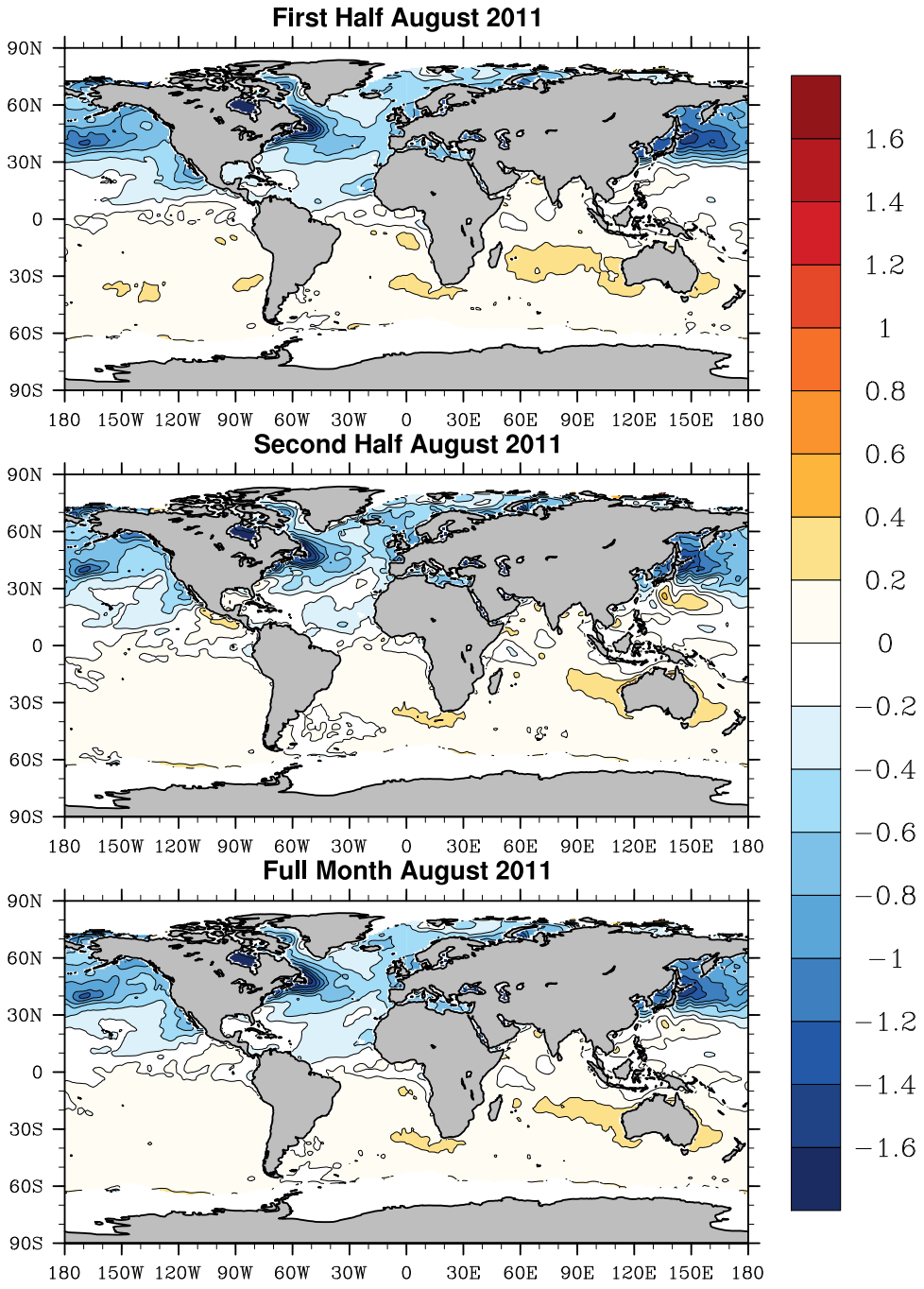

Figure 4.13: As in Fig. 4.7 but for August 2011.

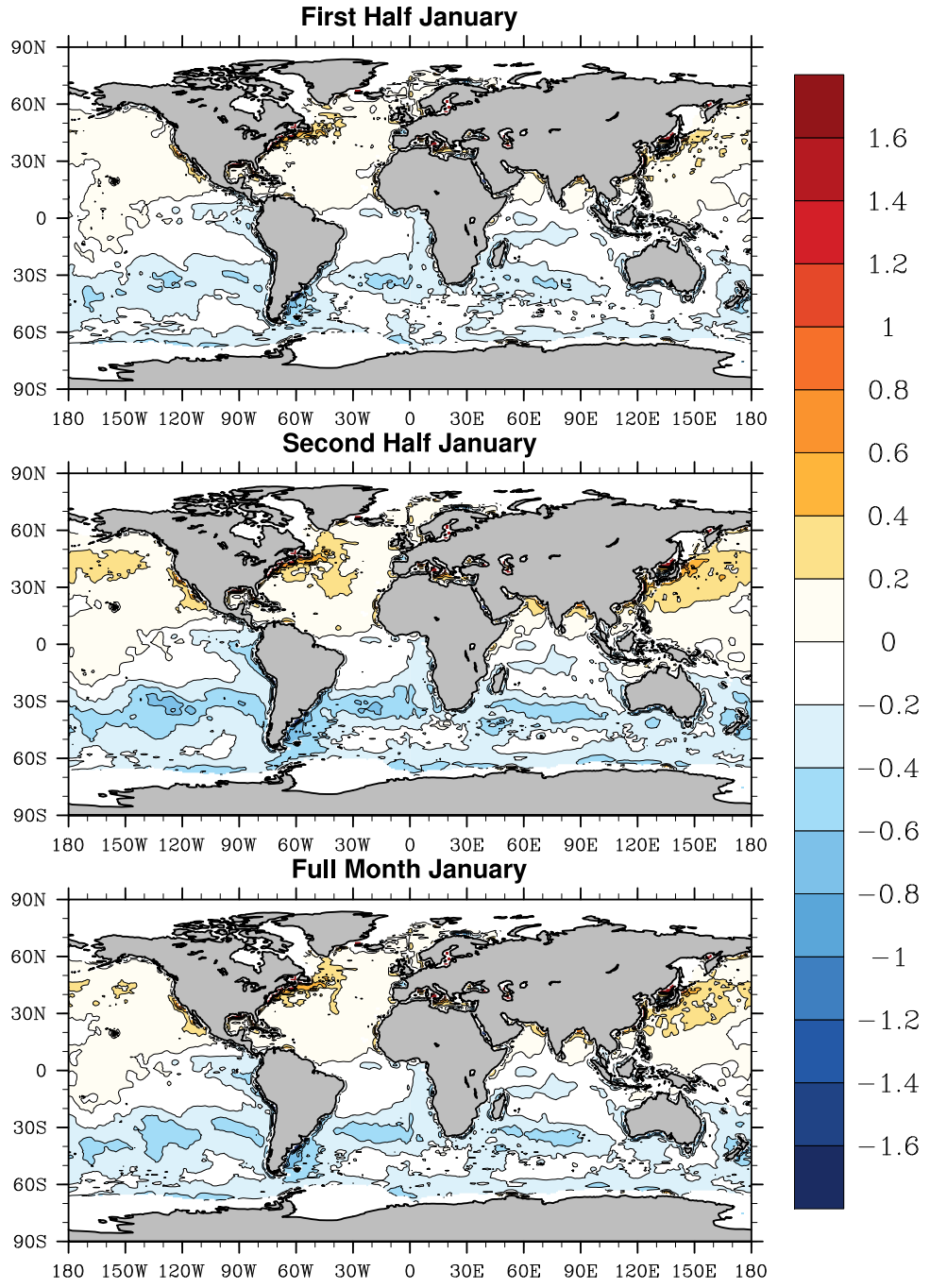

Figure 4.14: Differences in monthly global reforecast ensemble mean of SST in January between the two methods (daily forced minus operational ocean model). The top panel refers to the first fifteen days, the middle panel to the second fifteen days and the bottom panel to the full month. Values are in degrees Celsius.

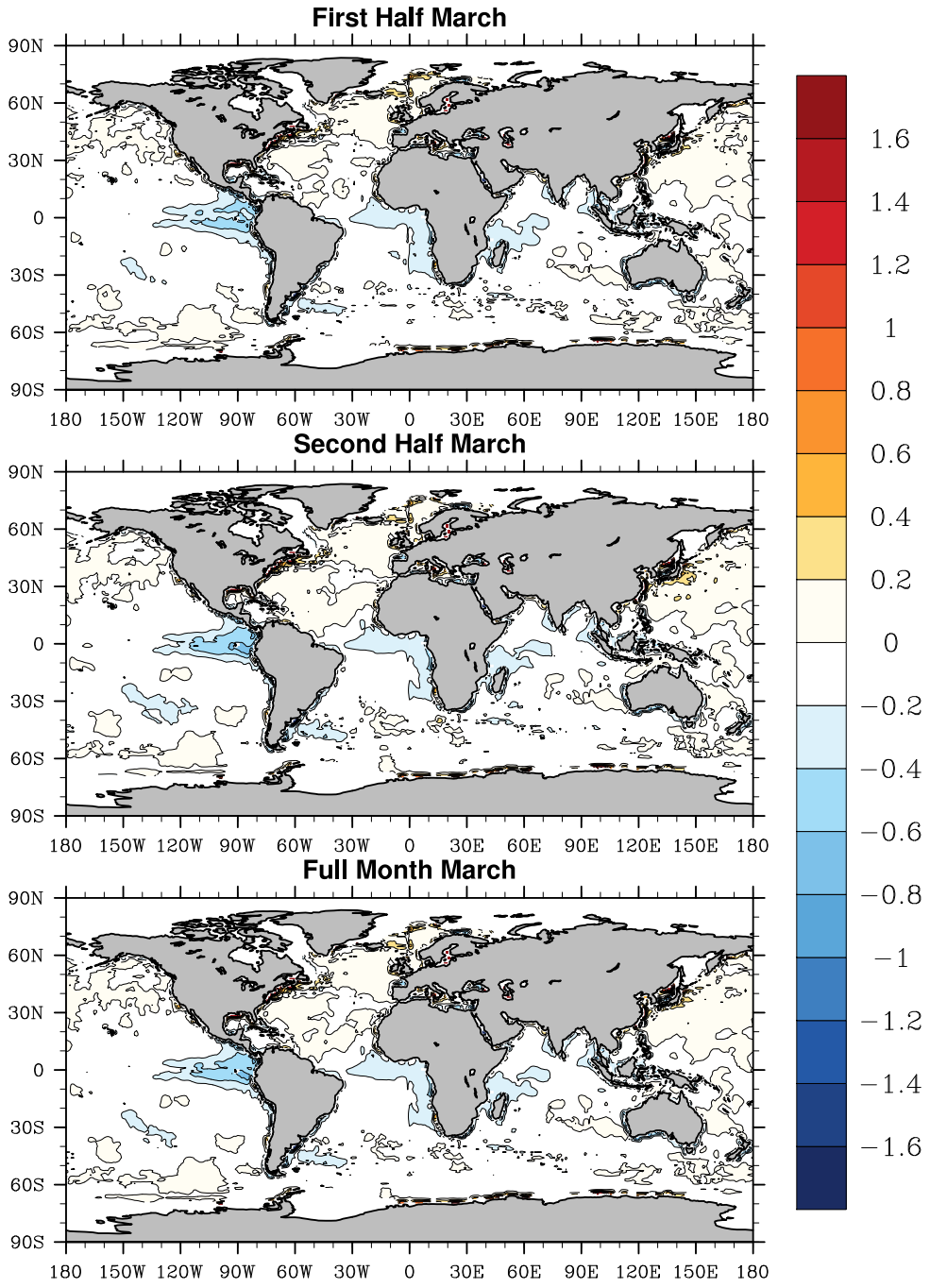

Figure 4.15: As in Fig. 4.14 but for March.

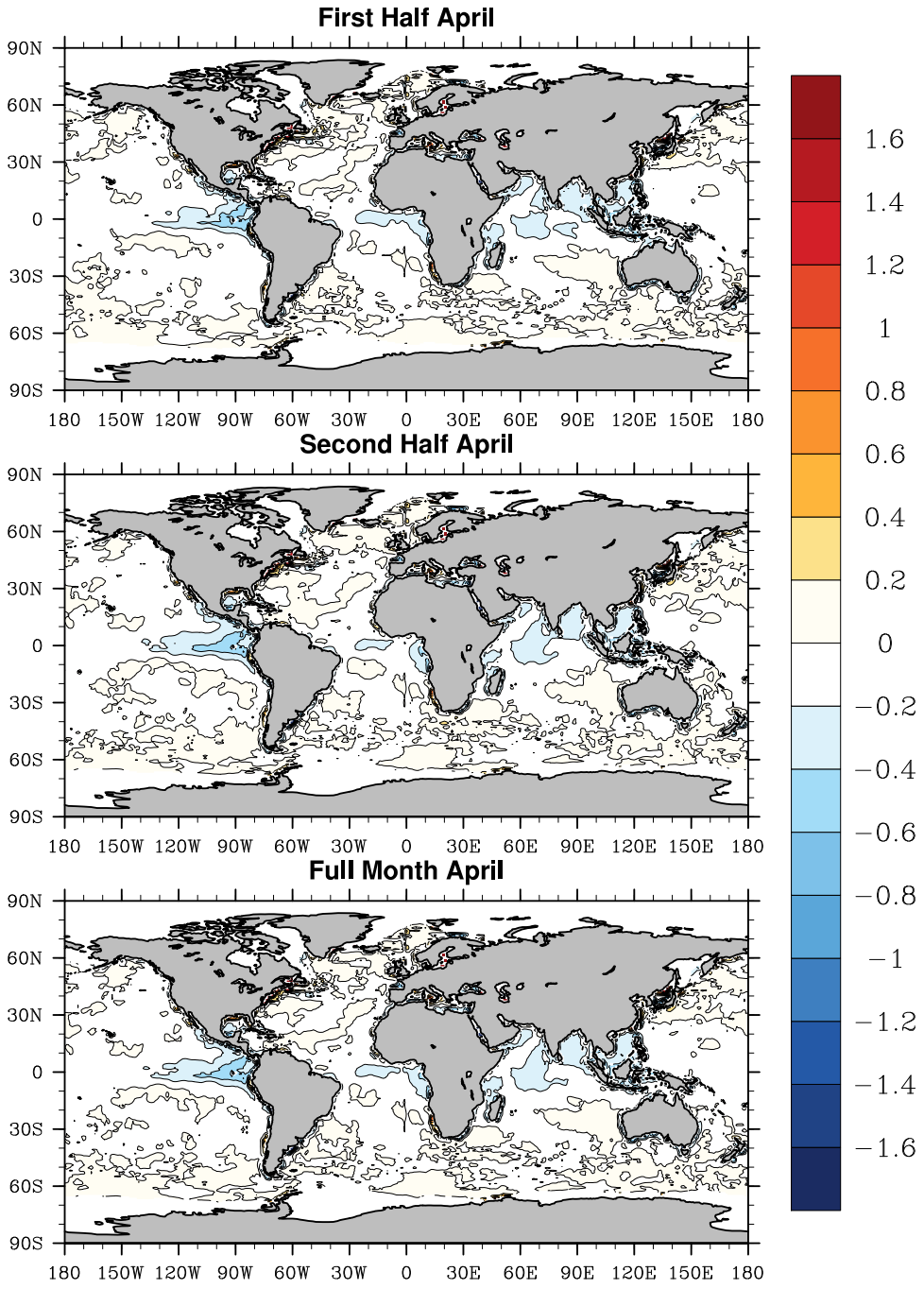

Figure 4.16: As in Fig. 4.14 but for April.

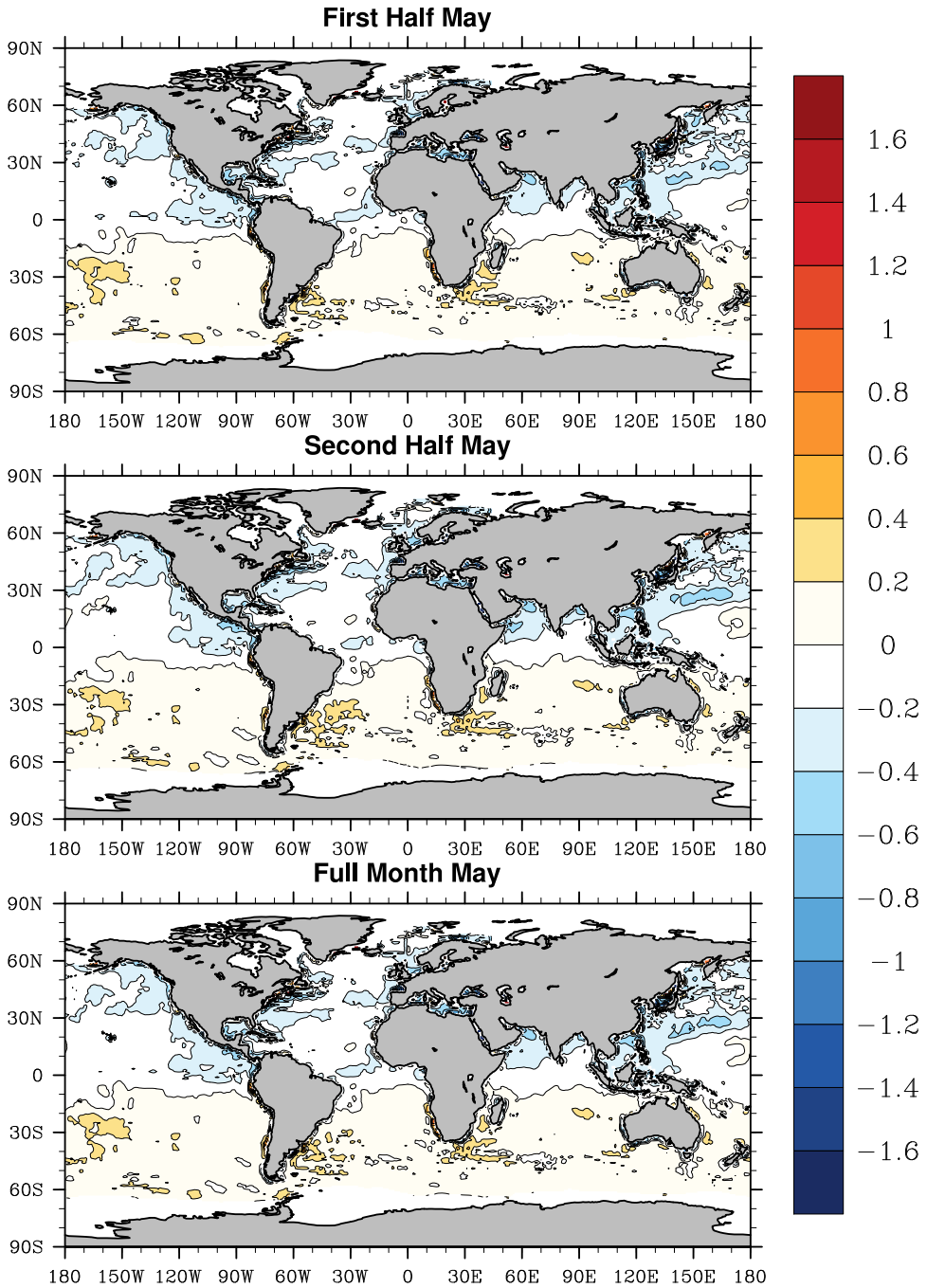

Figure 4.17: As in Fig. 4.14 but for May.

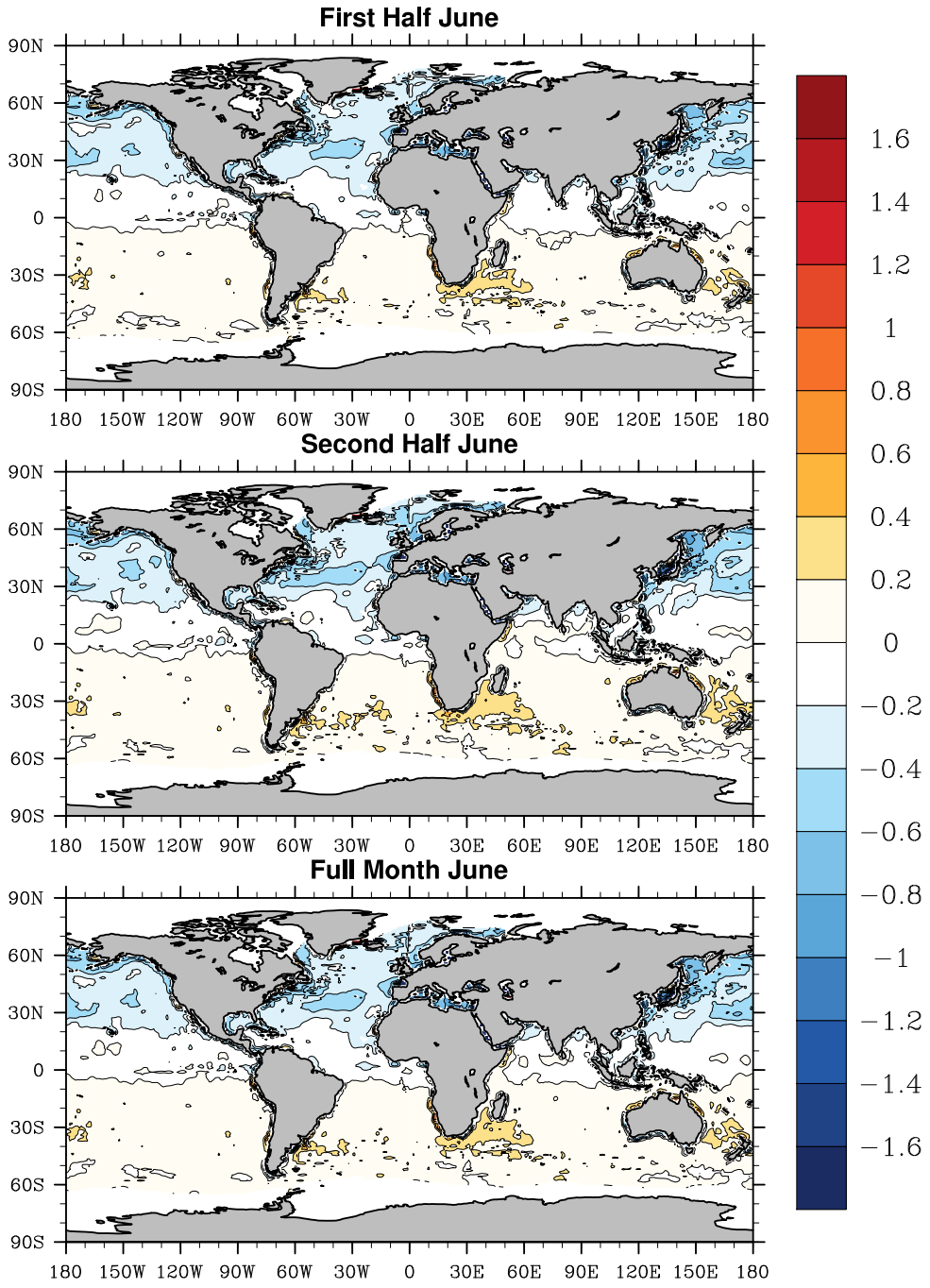

Figure 4.18: As in Fig. 4.14 but for June.

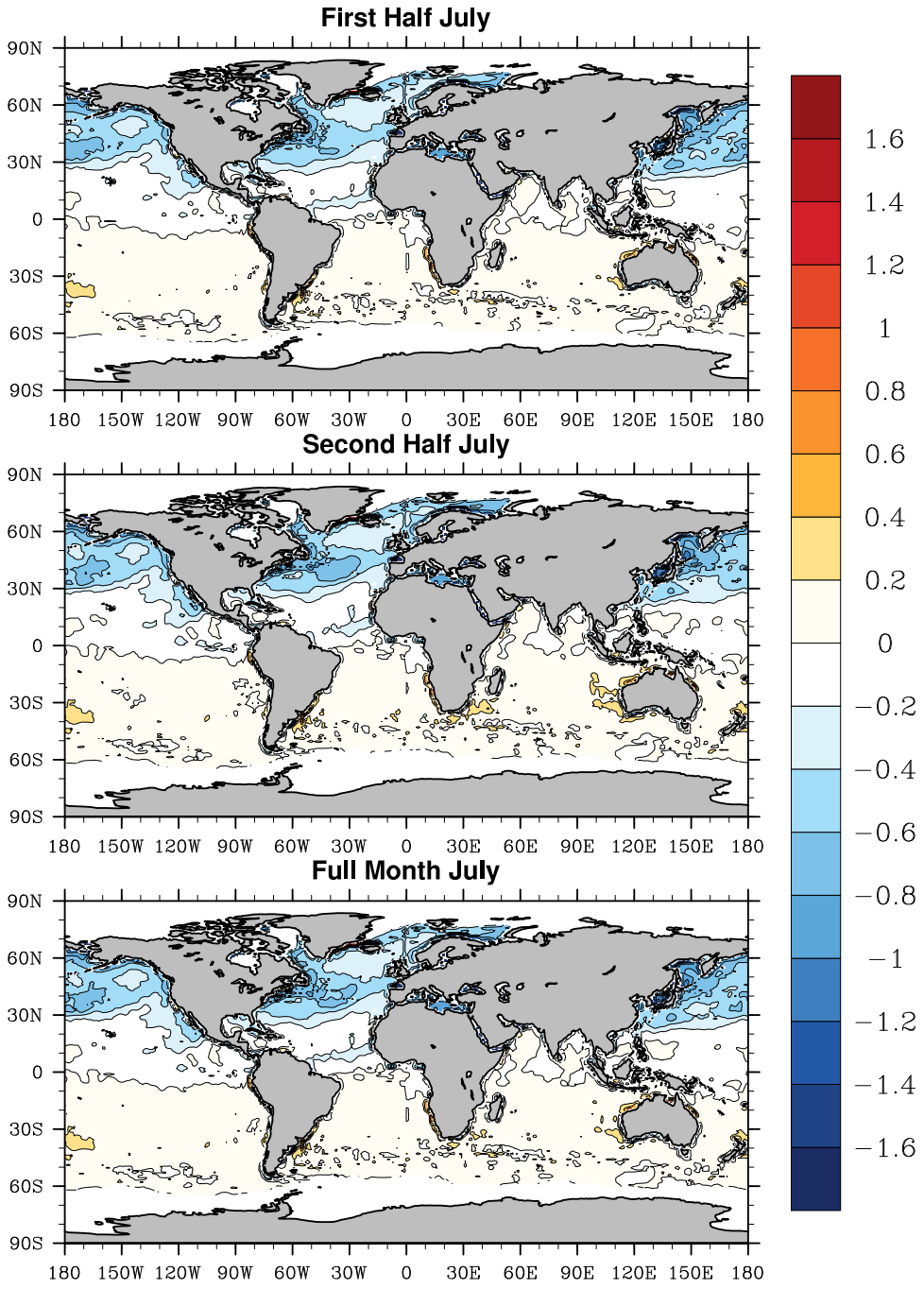

Figure 4.19: As in Fig. 4.14 but for July.

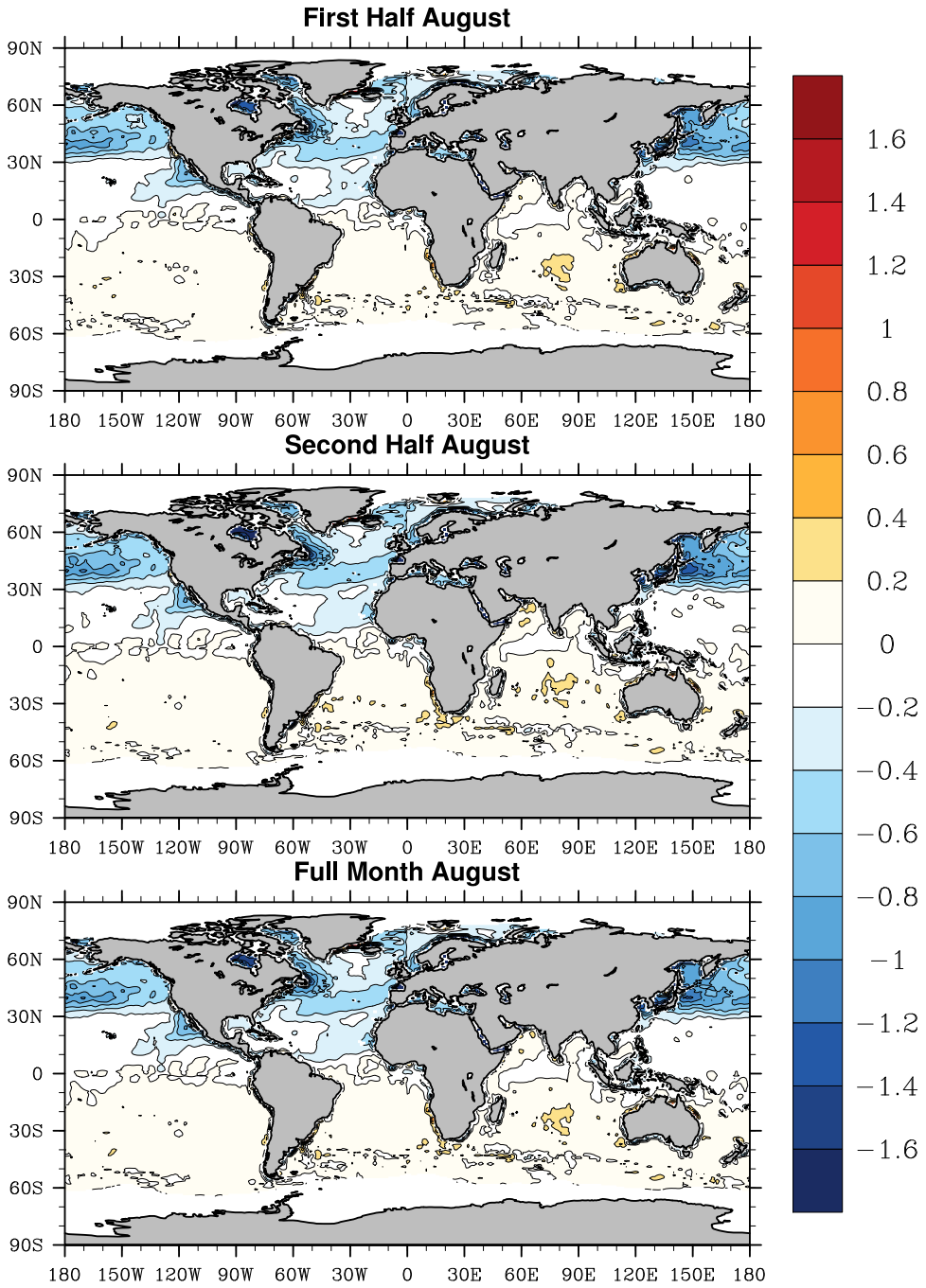

Figure 4.20: As in Fig. 4.14 but for August.

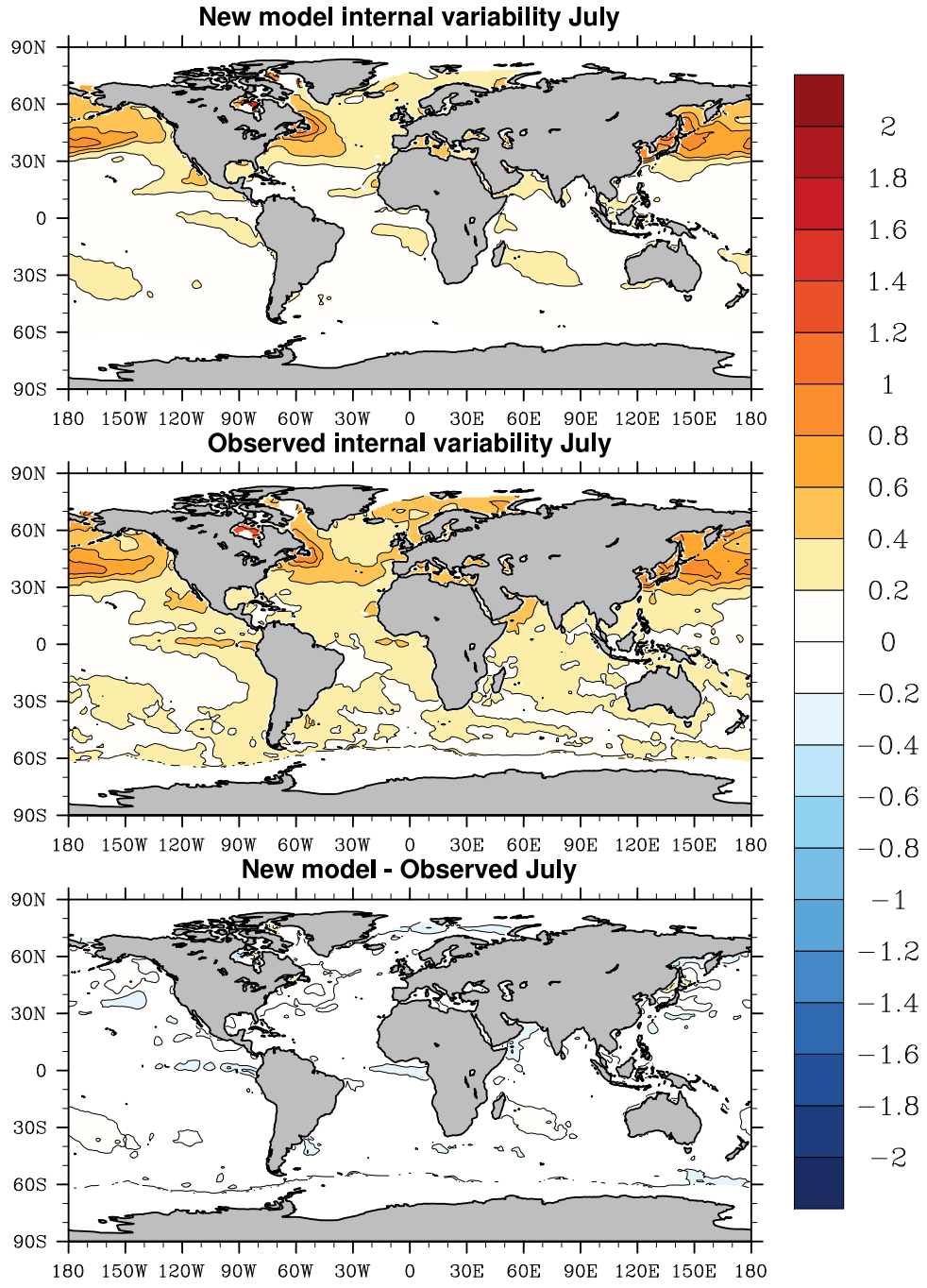

Figure 4.21: Global distribution of σ_{SST15} values for internal variability (see text) in the second part of July: in the top panel simulated by the new model, in the middle panel observed in Era-Interim, in the bottom panel the differences. Values are in degrees Celsius.

4.1.2 Verification using GFS analysis

Recently, the same verification of the forecast errors of SSTs simulated by the new and operational models has been made using daily GFS analysis as reference. This further evaluation is carried out since relativeli large differences of SST between ERA-Interim and GFS analysis were found, and since GFS analysis has been used as initial conditions for the monthly forecasts. Figure 4.22 shows the same content as figure 4.1, including also the GFS analysis. The two observations (ERA-Interim and GFS) have a different daily variability. Absolute differences between monthly averages of daily values of ERA-Interim and GFS are of order of 0.5 – 1°C (not shown).

Globally averaged forecast errors in terms of RMSE and MAE have also been computed with respect to GFS analysis using monthly averaged SST values (fig. 4.23). In this case, the forecast error of SST obtained with the new model is smaller than that obtained with the operational model in every simulated month, showing that the new model is better than operational model. However, these results are too dependent on the particular SST analysis used as reference.

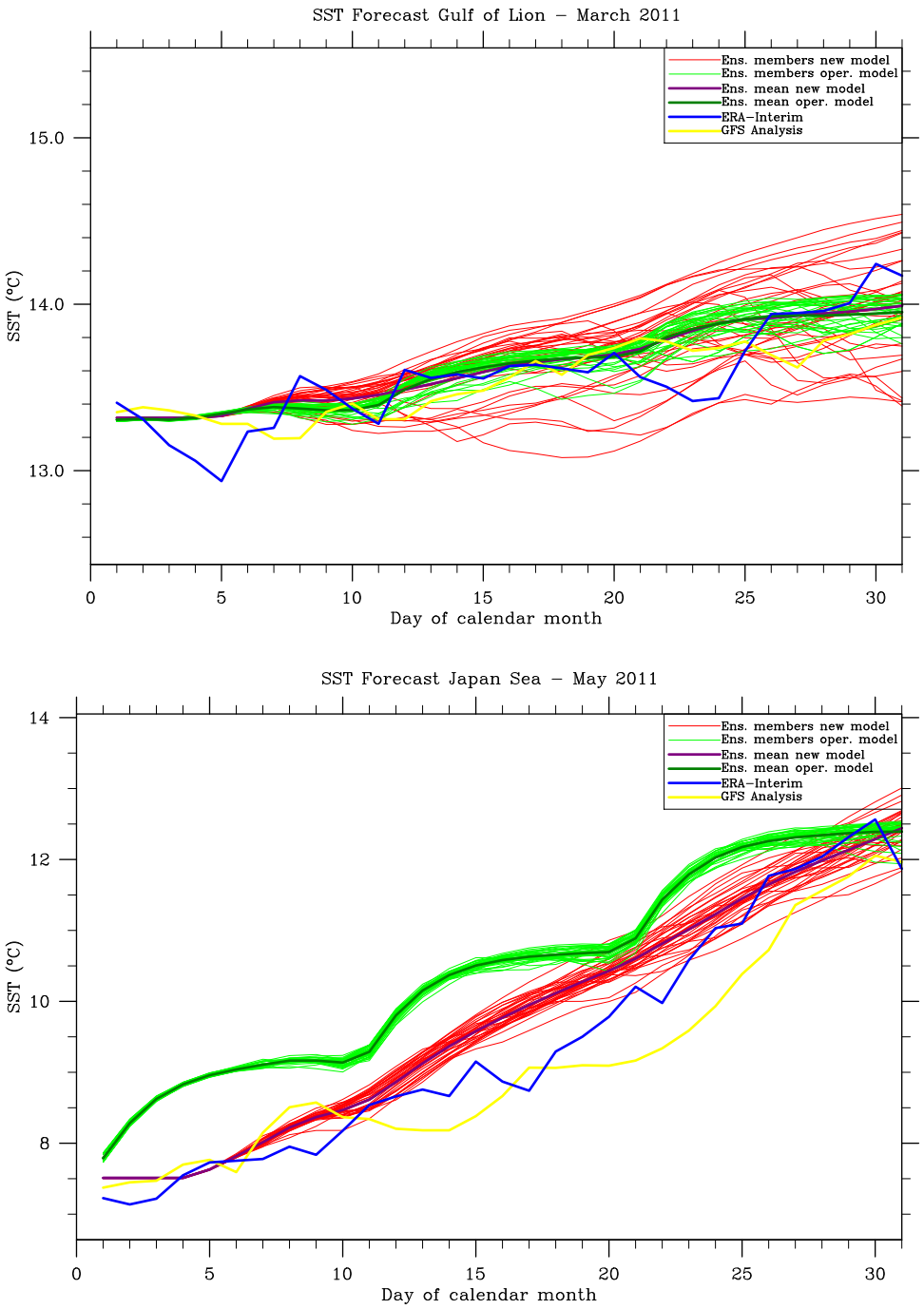

Figure 4.22: As in fig. 4.1, but with GFS analysis added.

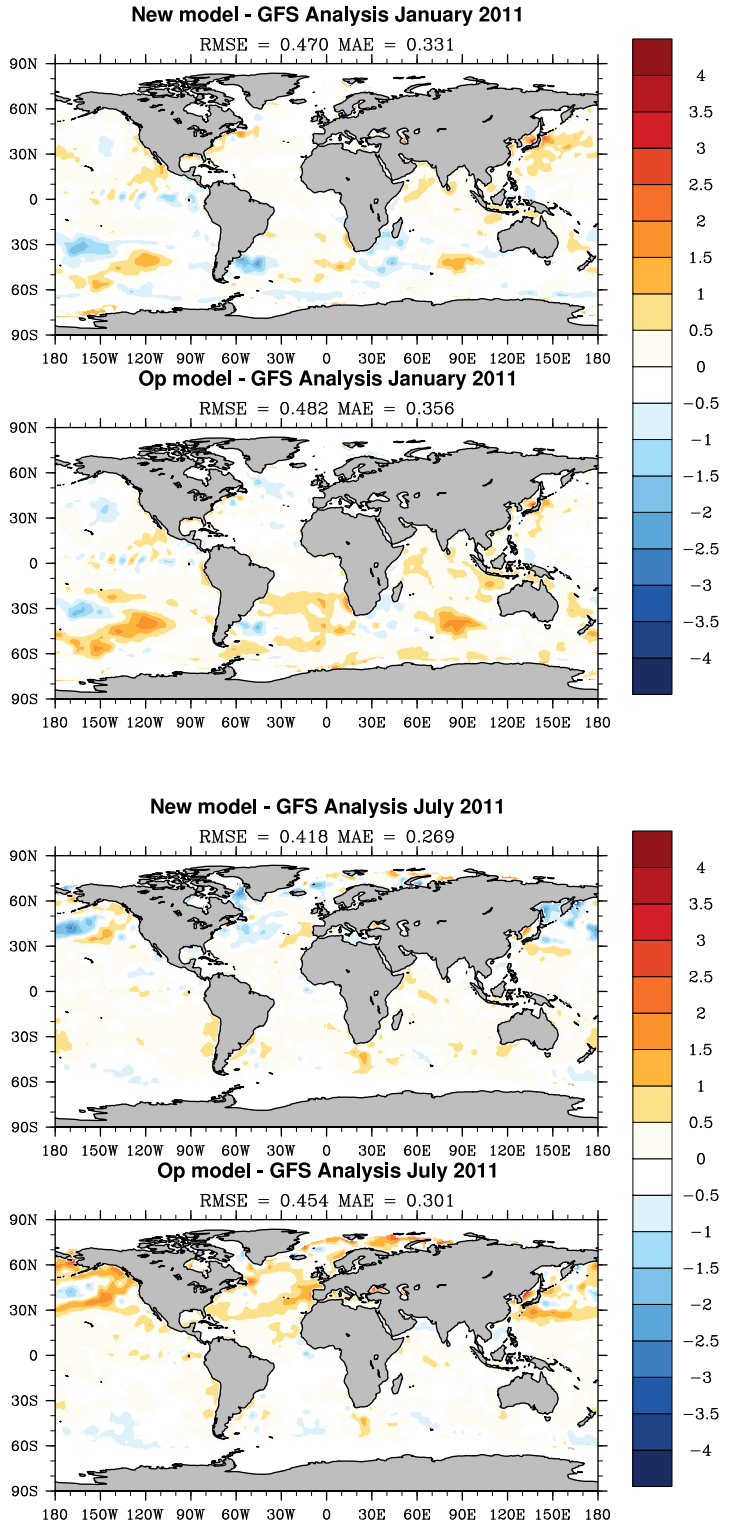

Figure 4.23: As in figure 4.3, but with GFS analysis for January 2011 (top) and July 2011 (bottom).

4.1.3 Differences in atmospheric fields

As discussed in chapter 3, the atmospheric parameters used to evaluate the forecasts are the geopotential height at 500 hPa, temperature at 850 hPa and accumulated precipitation. For the three variables the forecast and reforecast ensemble mean differences and spread are analyzed in this section. Only the months of January and July are shown in the figures, along with the differences averaged over all the simulated months.

Differences in geopotential height at 500 hPa

Figures 4.24–4.25 show some particular features in the difference patterns between the two forecast methods. The differences present very small amplitude (about 5 meters) in the first 15-days period of each month, while this amplitude increases in the second 15-days period, reaching absolute values of about 50 meters in some cases. The largest difference values are present in the winter hemisphere in the middle and high latitudes. In the Southern Hemisphere, the difference fields generally assume a shape of a wavenumber 3 pattern, while in the Northern Hemisphere the patterns are different in the different months. This is clearly visible in the difference fields averaged over the simulated months shown in figure 4.26, in which the Southern Hemisphere has still a pattern as described above, while the Northern Hemisphere shows very small averaged difference values. Another feature is that in many cases the sign of the difference values turns out to be opposite in some areas between the first and the second period of the month, which means that there is an evolution in time of the spatial differences. A constant feature in the simulated months consists in a lower height in the equatorial belt for the new forecasts with respect to the operational ones.

From this analysis we can infer that the "forcing" signal that comes from different SST evolutions in the first days of the monthly forecast can change the

circulation pattern in the middle troposphere and middle latitudes after about 15-20 days. However the differences that are present between the new and the operational forecast datasets are visible, with smaller amplitude but similar patterns, also between the reforecast dataset obtained with the operational version of the slab model and the reforecast that is forced with daily observed SST and sea ice cover data (see fig.4.27–4.28). This means that the systematic differences between the reforecast datasets that arise using different ocean temperature forcings are well correlated with the differences between the respective forecasts. This implies that the final products, i.e. the anomaly forecast patterns obtained with the new method, are very similar to the operational ones (we will see in detail in section 4.1.5).

A comparison of the daily RMSE for both the reforecast methods has been made (fig. 4.30) in order to verify if using a forcing with daily observed SST data can improve the systematic error in the model atmospheric climate for this parameter. However, as the figure shows, the systematic errors are very similar in both cases, although in some cases the daily-forced method increases a little the RMSE compared to the operational reforecast method.

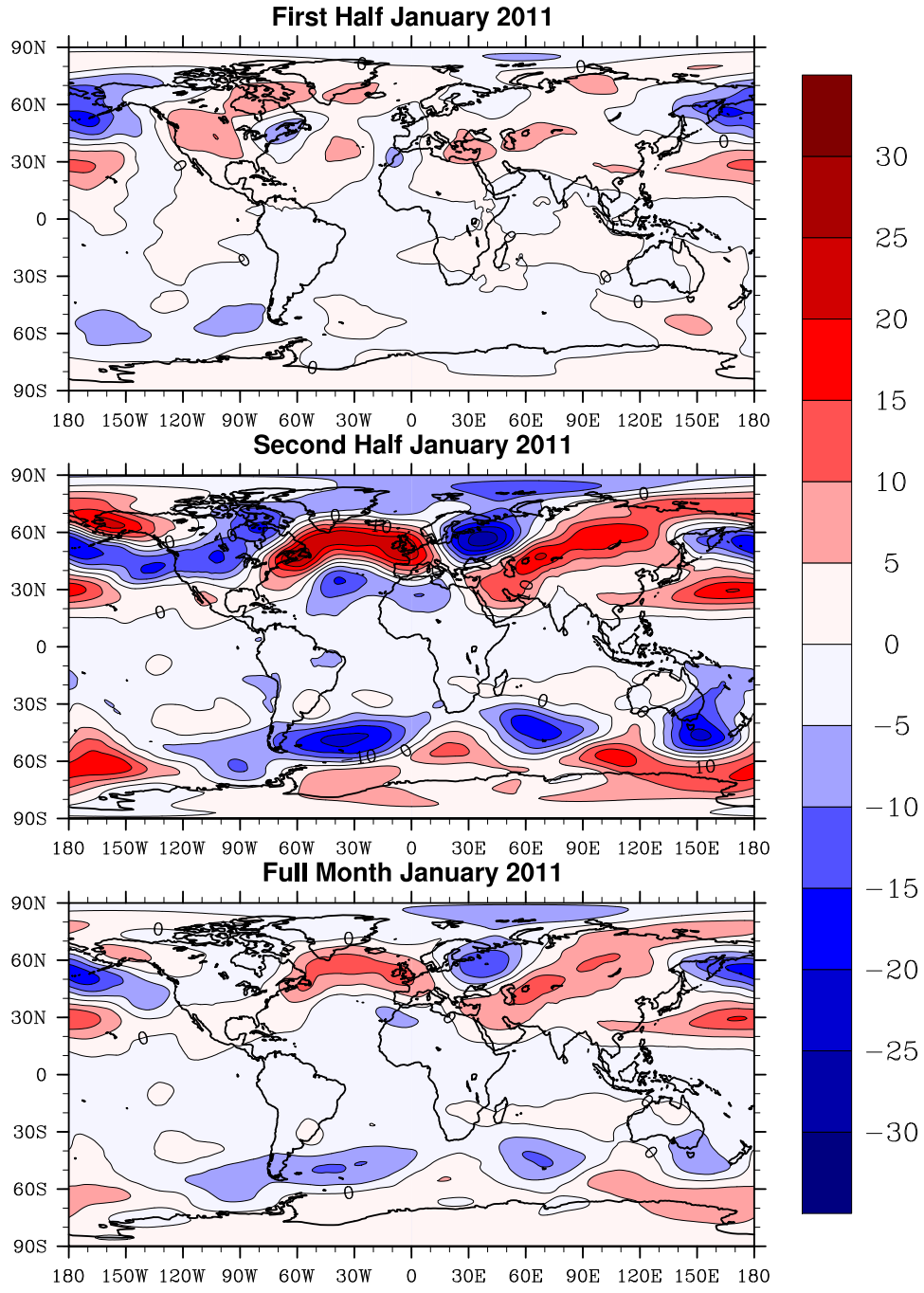

Figure 4.24: Global distribution of the differences in monthly forecast ensemble mean of geopotential height at 500 hPa in January 2011 between the two models (new minus operational). The top panel refers to the first fifteen days, the middle panel to the second fifteen days and the bottom panel to the full month. Values are in meters.

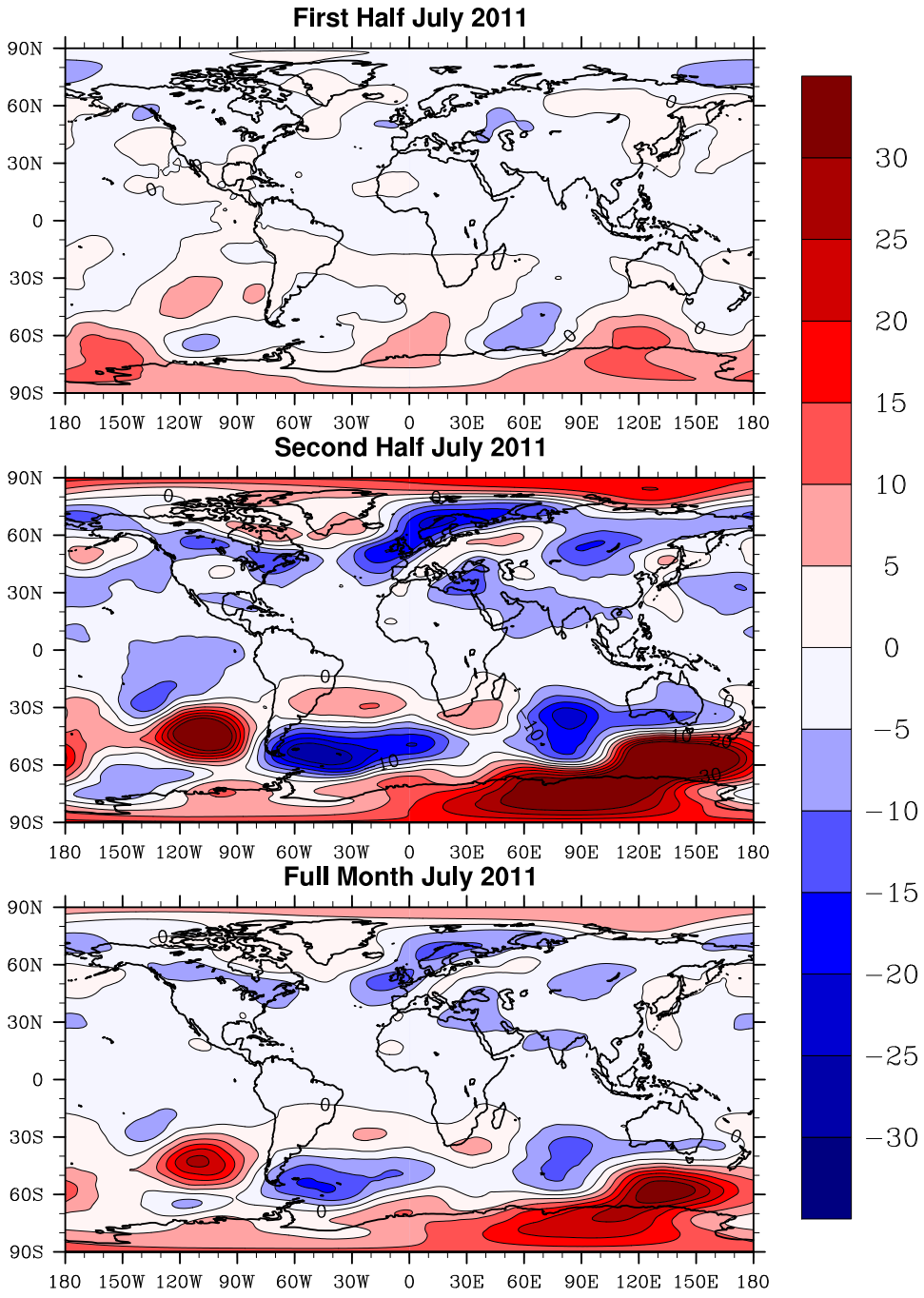

Figure 4.25: As in Fig. 4.24 but for July 2011.

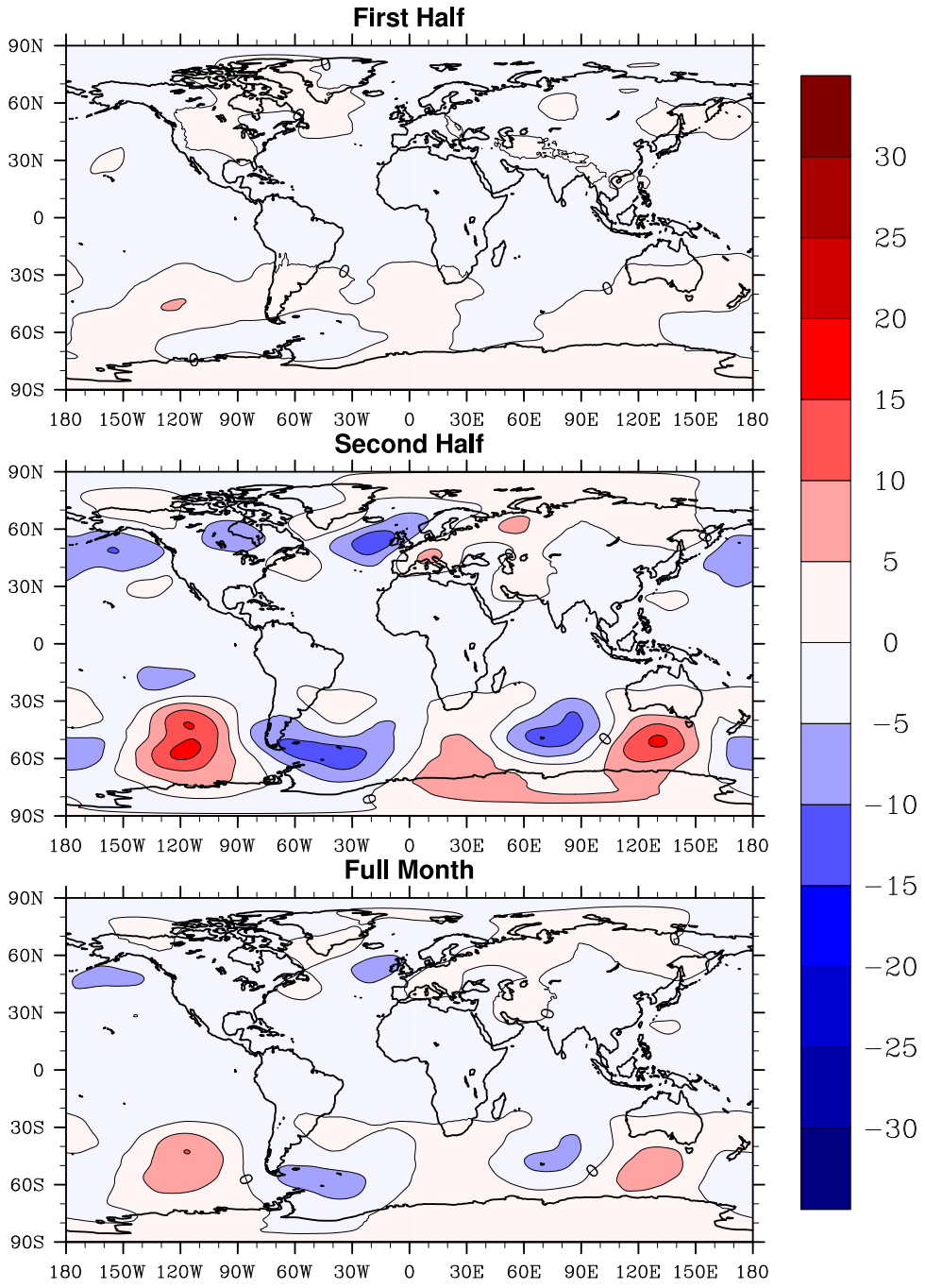

Figure 4.26: As in Fig. 4.24 but averaged over the simulated months.

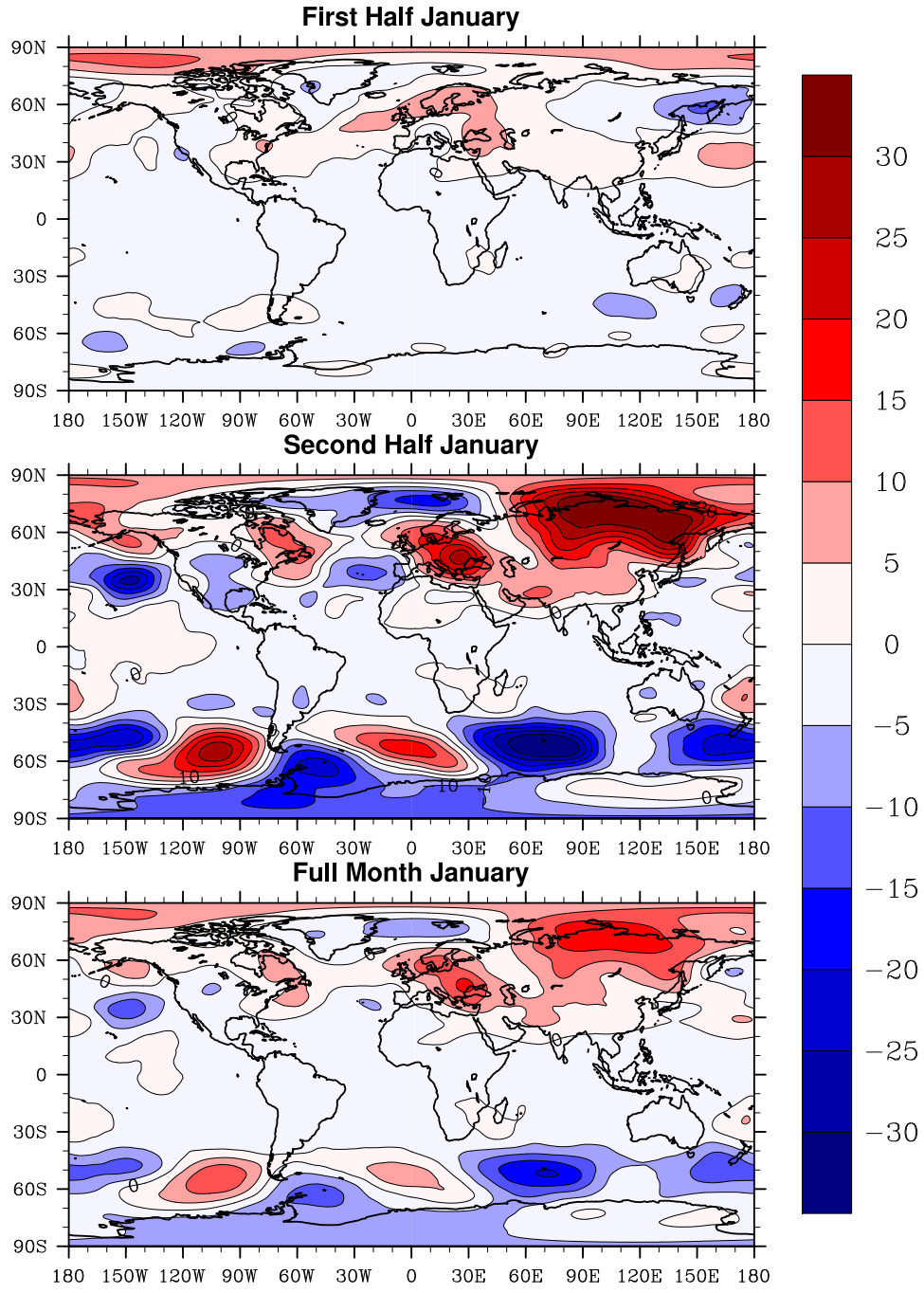

Figure 4.27: Global distribution of the differences in monthly reforecast ensemble mean of geopotential height at 500 hPa in January between the two methods (daily forced minus operational ocean model). The top panel refers to the first fifteen days, the middle panel to the second fifteen days and the bottom panel to the full month. Values are in meters.

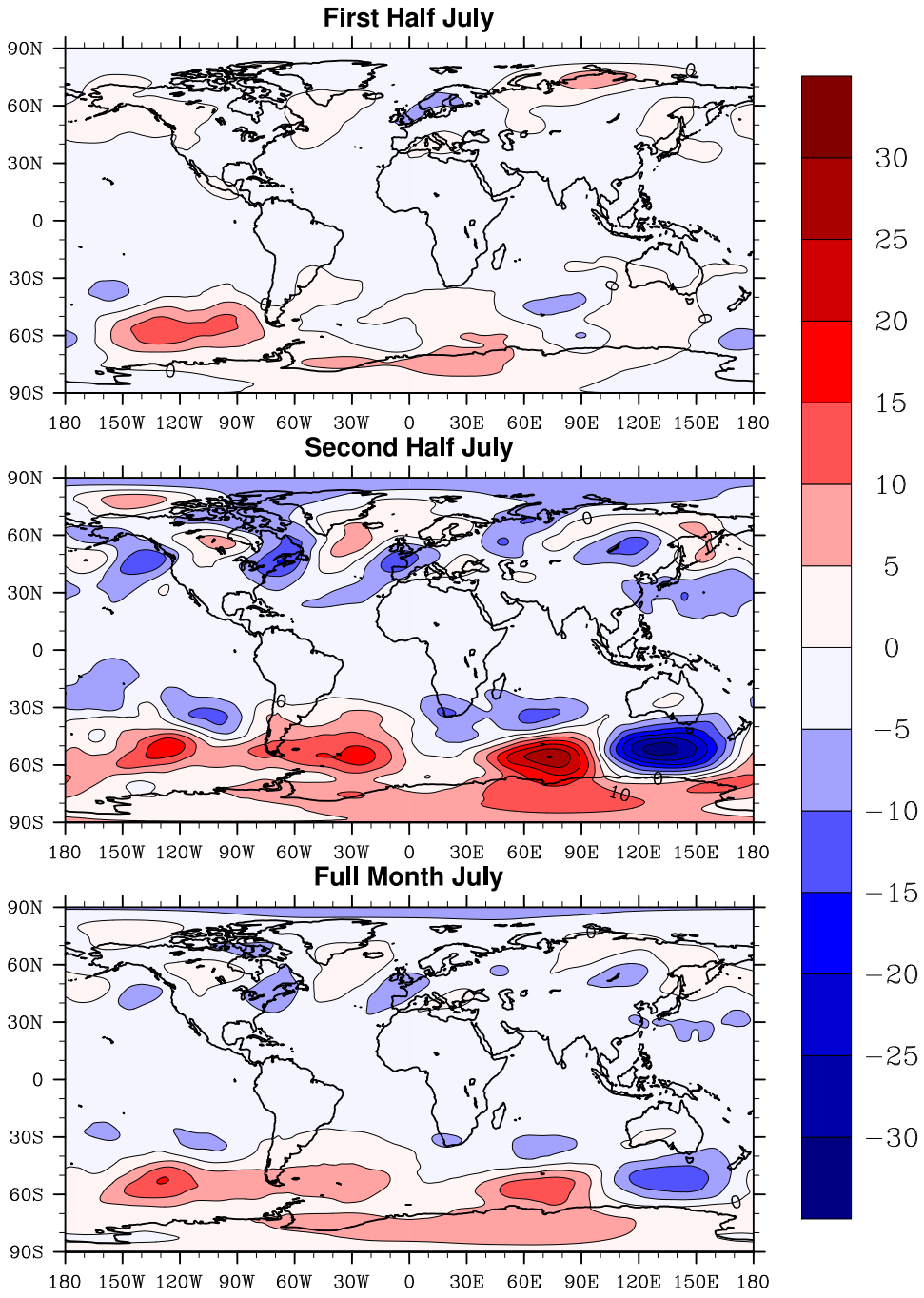

Figure 4.28: As in Fig. 4.27 but for July.

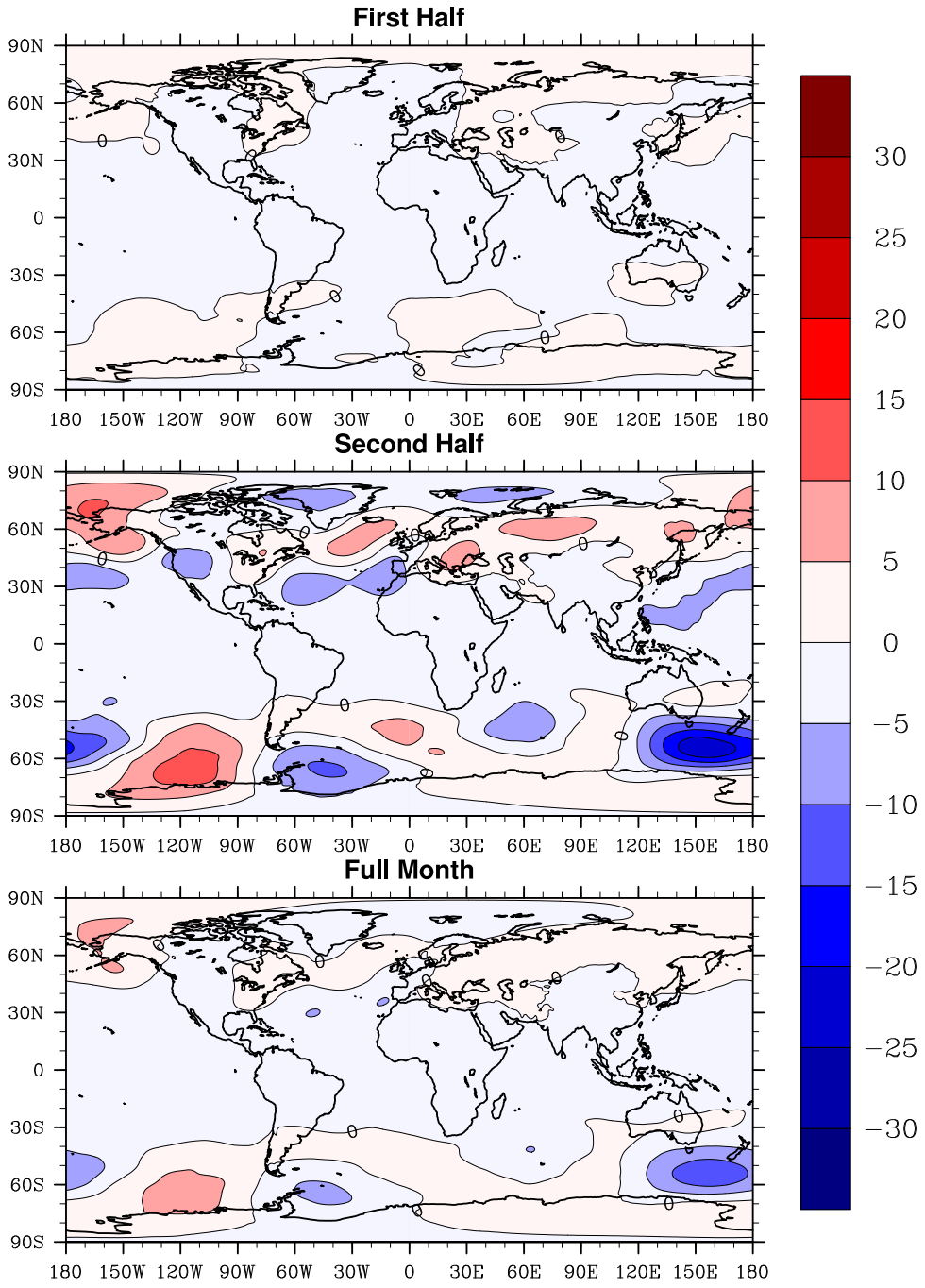

Figure 4.29: As in Fig. 4.27 but averaged over the simulated months.

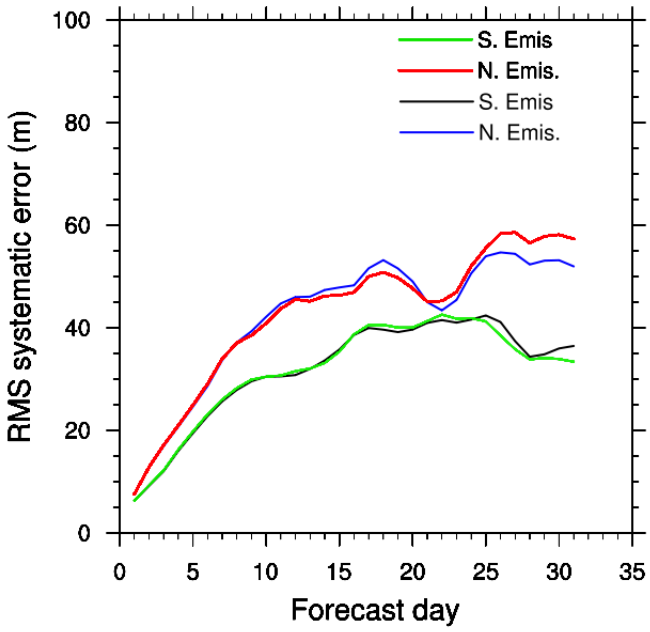

(a) January

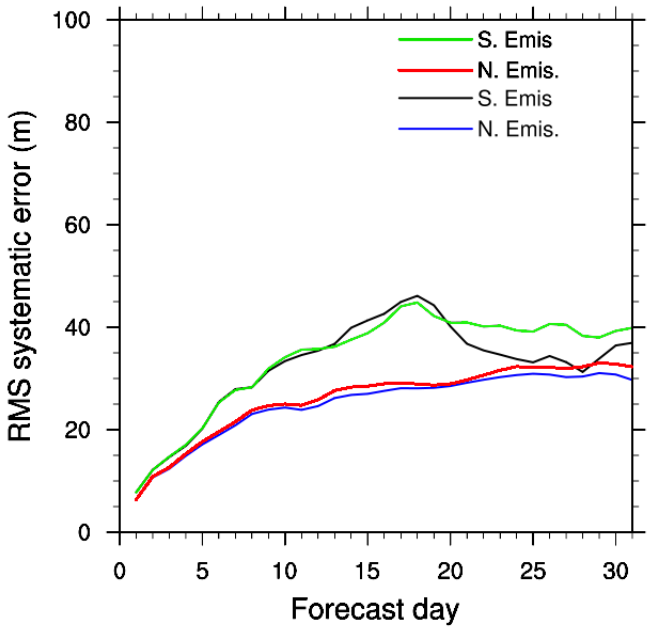

(b) July

Figure 4.30: Daily RMSE of geopotential height at 500 hPa in the Northern (20N-80N) and Southern (20S-80S) Hemispheres for January and July. Red and green lines refer to the reforecast forced with daily SST data, blue and black refer to the reforecast obtained with the operational version of the slab model.

Temperature at 850 hPa

Like for the previous parameter, the temperature at 850 hPa shows the increase of the amplitude in the differences from the first part of the month to the second one between the forecast ensemble means obtained with the two methods (fig 4.31–4.32). Generally, the maximum amplitude is around 1 – 1.5 °C in absolute value. The difference patterns are similar to those of geopotential height: the largest differences are present in the winter hemisphere, at middle-to-high latitudes (in the latter case also in the summer hemisphere). Patterns match quite well the geopotential height difference patterns. In the equatorial belt, there constantly is colder temperature in the new forecast model than in the operational one (in the range −0.5 – 0 °C in average), due to the colder SST simulated by the new ocean model shown in section 4.1.1. In the winter hemisphere, the differences are mostly positive, while, in the summer hemisphere, they are negative.

A similar analysis emerges from the reforecast ensemble mean differences. Such fields show patterns similar to the T850 forecast difference patterns (fig 4.34–4.35), with a sligthly higher values than the forecasts (up to 2 °C in absolute value). The equatorial belt shows colder temperature in the daily-forced reforecast with respect to the operational one, matching very well the same colder pattern found in SST reforecast difference fields shown in section 4.1.1, with values ranging −0.5 - 0 °C. Winter hemisphere middle-to-high latitudes also exhibit a positive pattern and the summer hemisphere a negative one.

Another question arises regarding the reforecast differences present in July and August. In these months, there is a large positive bias around the Antarctic continent coasts also in the first fifteen days. This means that the heat fluxes simulated by the model over sea ice cover are possibly incorrect, and that the sea ice cover can have a more intense impact on the lower troposphere than expected.

Figure 4.37 shows the RMSE of the temperature at 850 hPa for the two

reforecast datasets. Even for this parameter, in general, the values are similar between the two methods. Nevertheless, in some cases there is a little improvement using daily forcing, like, for example, in January where the RMSE for both the hemispheres decreases significantly (also in May for the Southern Hemisphere, not shown). This is in contrast with the RMSE of the geopotential height at 500 hPa that shows a slighter increase.

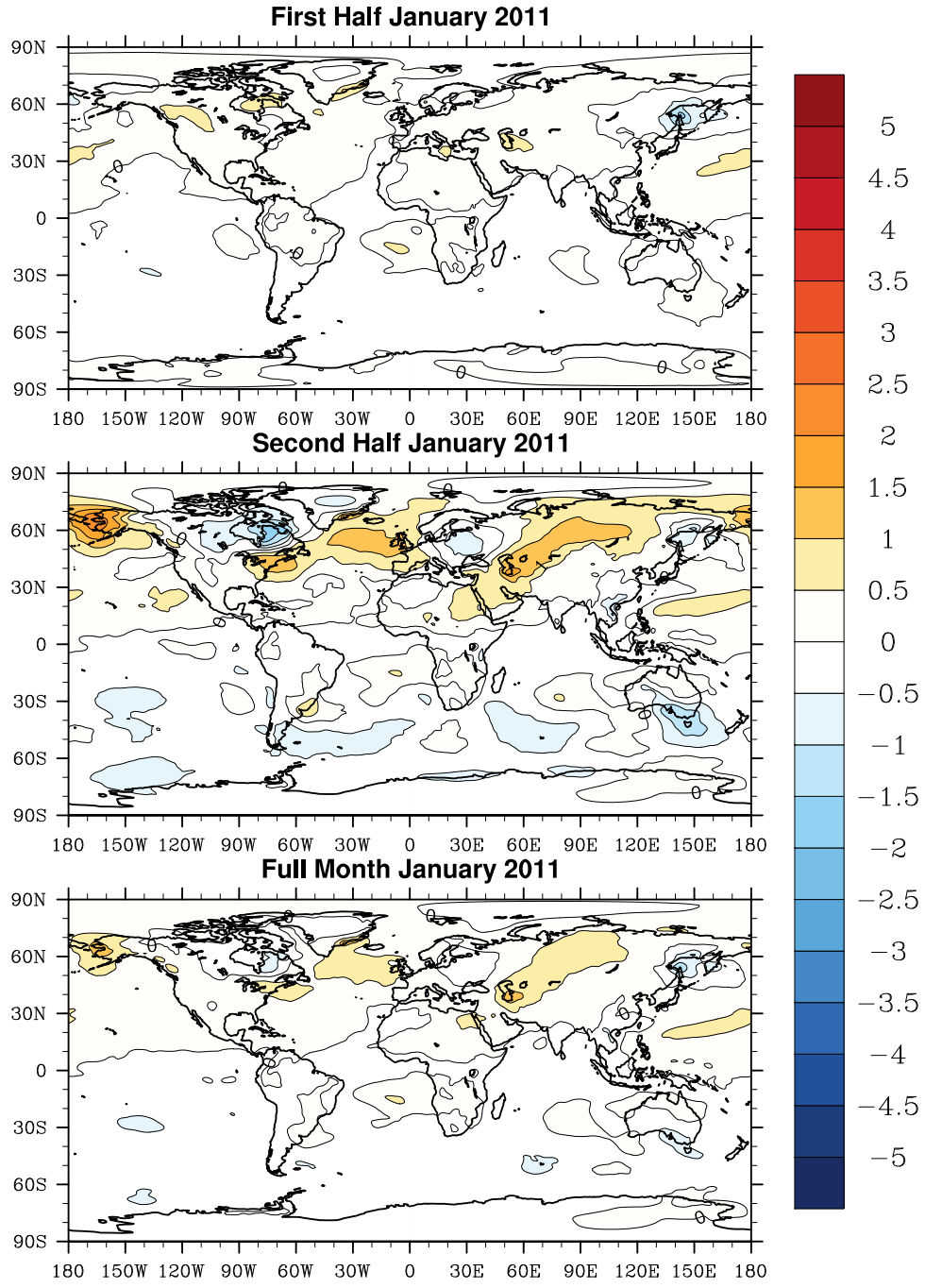

Figure 4.31: Global distribution of the differences in monthly forecast ensemble mean of temperature at 850 hPa in January 2011 between the two models (new minus operational). The top panel refers to the first fifteen days, the middle panel to the second fifteen days and the bottom panel to the full month. Values are in degrees Celsius.

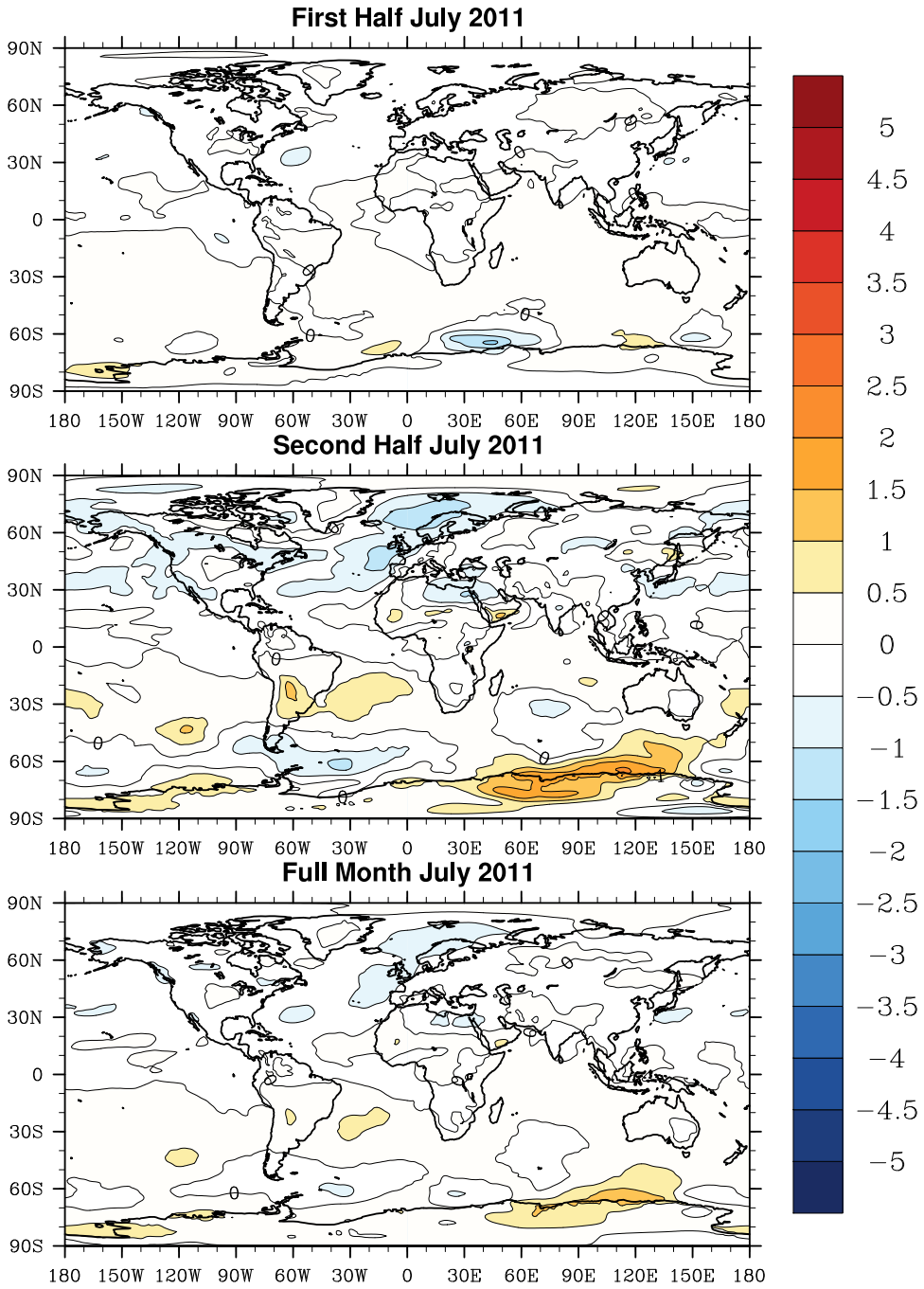

Figure 4.32: As in Fig. 4.31 but for July 2011.

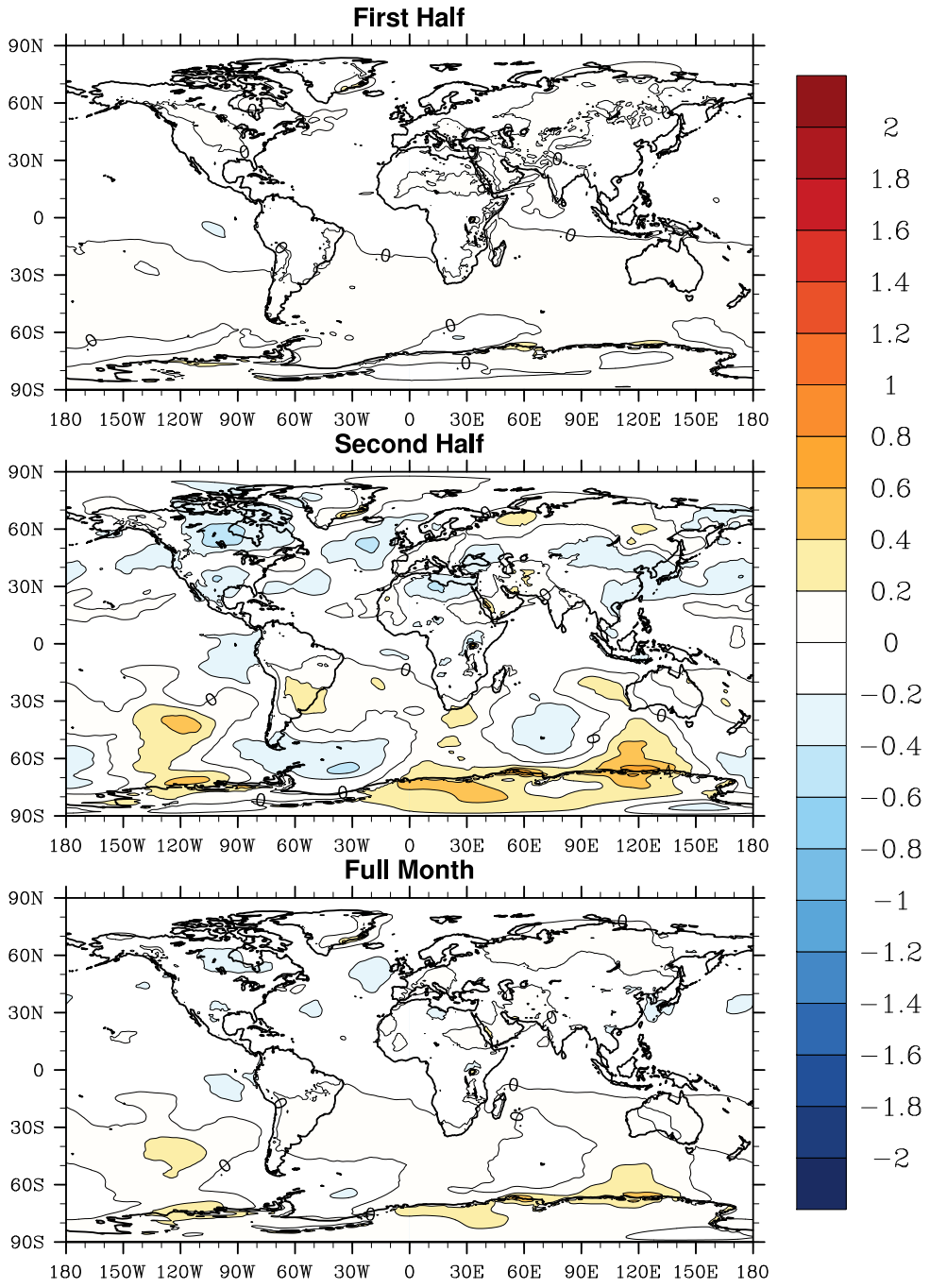

Figure 4.33: As in Fig. 4.31 but averaged over the simulated months.

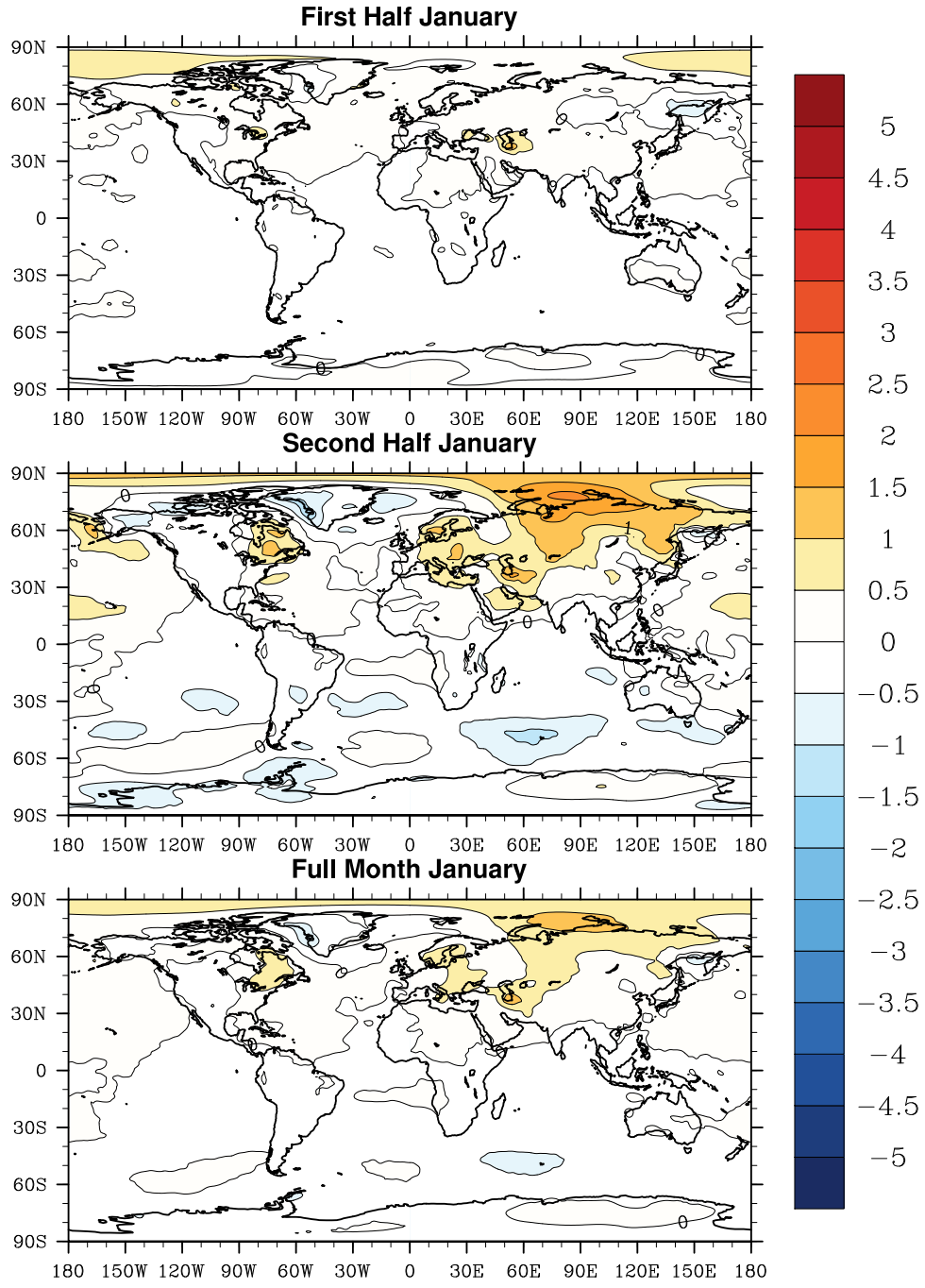

Figure 4.34: Global distribution of the differences in monthly reforecast ensemble mean of temperature at 850 hPa in January between the two methods (daily forced minus operational ocean model). The top panel refers to the first fifteen days, the middle panel to the second fifteen days and the bottom panel to the full month. Values are in degrees Celsius.

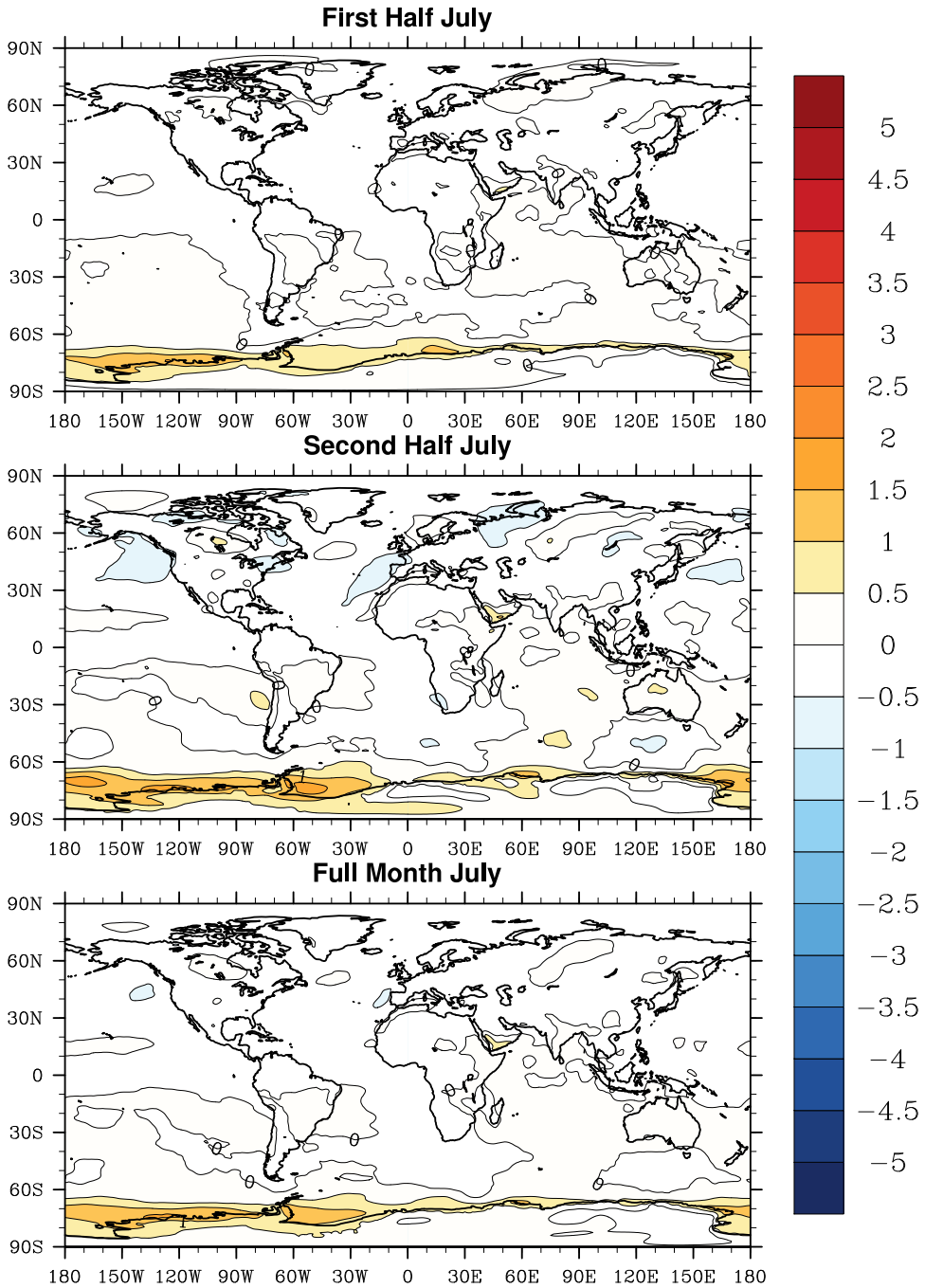

Figure 4.35: As in Fig. 4.34 but for July.

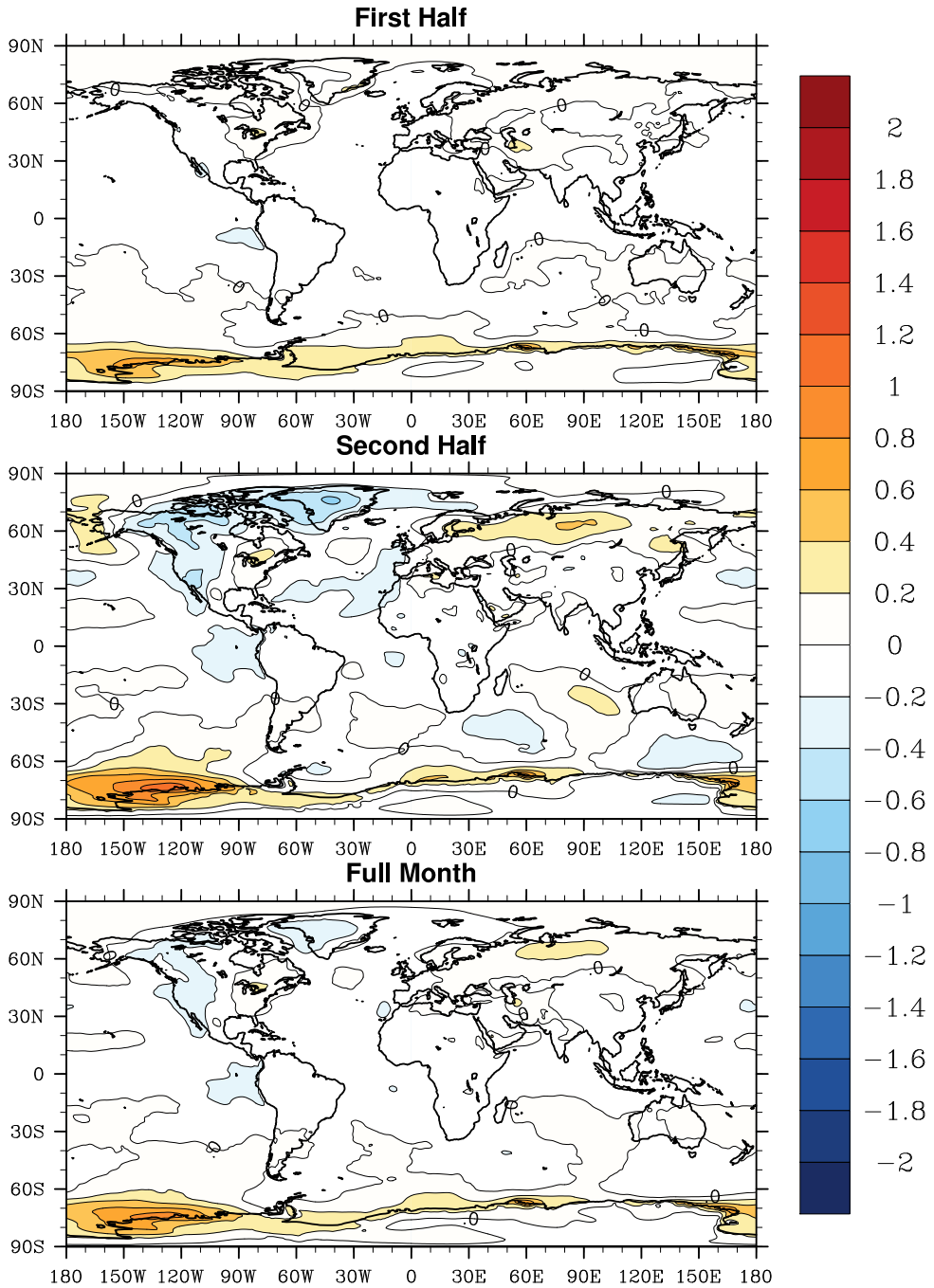

Figure 4.36: As in Fig. 4.34 but averaged over the simulated months.

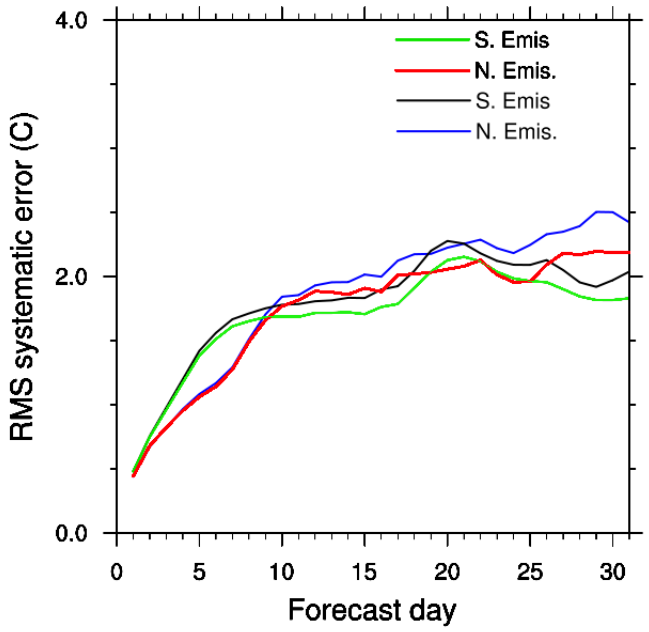

(a) January

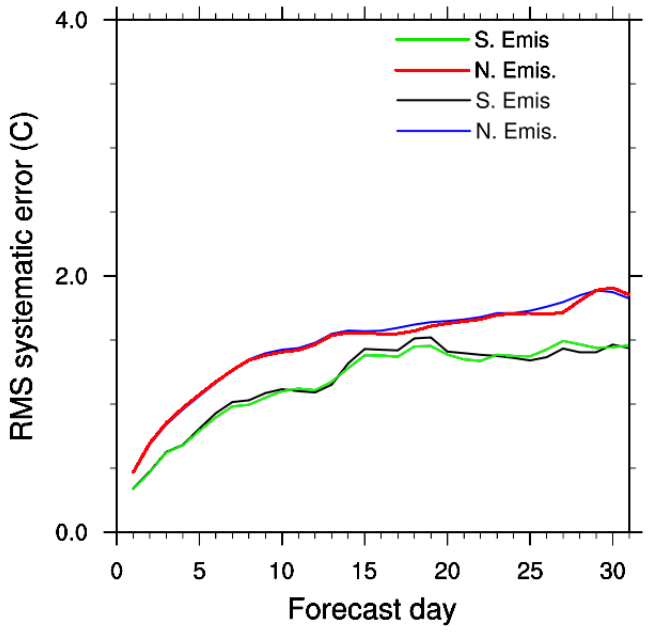

(b) July

Figure 4.37: Daily RMSE for temperature at 850 hPa in the Northern (20N – 80N) and Southern (20S – 80S) Hemispheres. Red and green lines refer to the reforecast forced with daily SST data, blue and black refer to the reforecast obtained with the operational version of the slab model.

Daily precipitation

Daily precipitation difference fields show some peculiar behaviours with respect to geopotential height and temperature. The temporal evolution is similar to the other two parameters, with an increasing amplitude of the differences from the first to the second part of the month. In some areas, the differences have a similar amplitude for both periods, indicating a relevant impact of the SST on the local scale in shorter time scales. However, the areas affected by the maximum difference values are those around the Equator, in the Pacific Ocean and Maritime Continent, Africa, South America and South Asia (see fig. 4.38 – 4.39). In many areas the differences reach 10 mm/day (the contour lines are showed every 5 mm/day) and are mostly related to the convective activity. In the forecasts with the new ocean model, the Asian monsoon is delayed in June 2011 (strong negative values, not shown) and too active in July 2011 (strong positive values). These differences are apparently due only to the different SST forcing. Also for this parameter, the difference patterns between the reforecast ensemble means are well correlated to the difference patterns between the respective forecasts, as well as for geopotential height and temperature. This implies then that anomaly forecast patterns are very similar between the new method and the operational one.

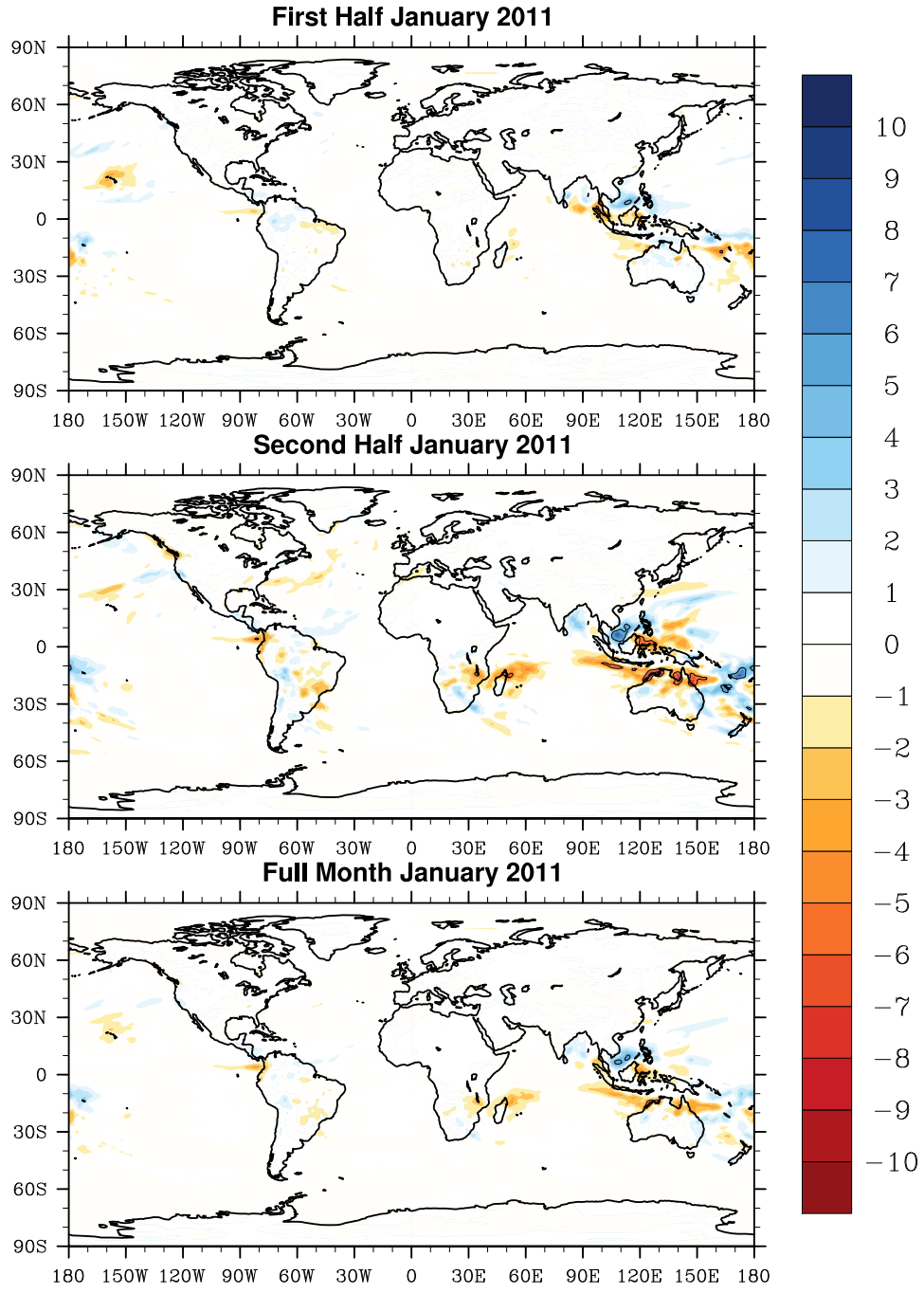

Figure 4.38: Global distribution of the differences in monthly forecast ensemble mean of daily precipitation in January 2011 between the two models (new minus operational). The top panel refers to the first fifteen days, the middle panel to the second fifteen days and the bottom panel to the full month. Values are in mm/day. Countur lines every 5 mm/day

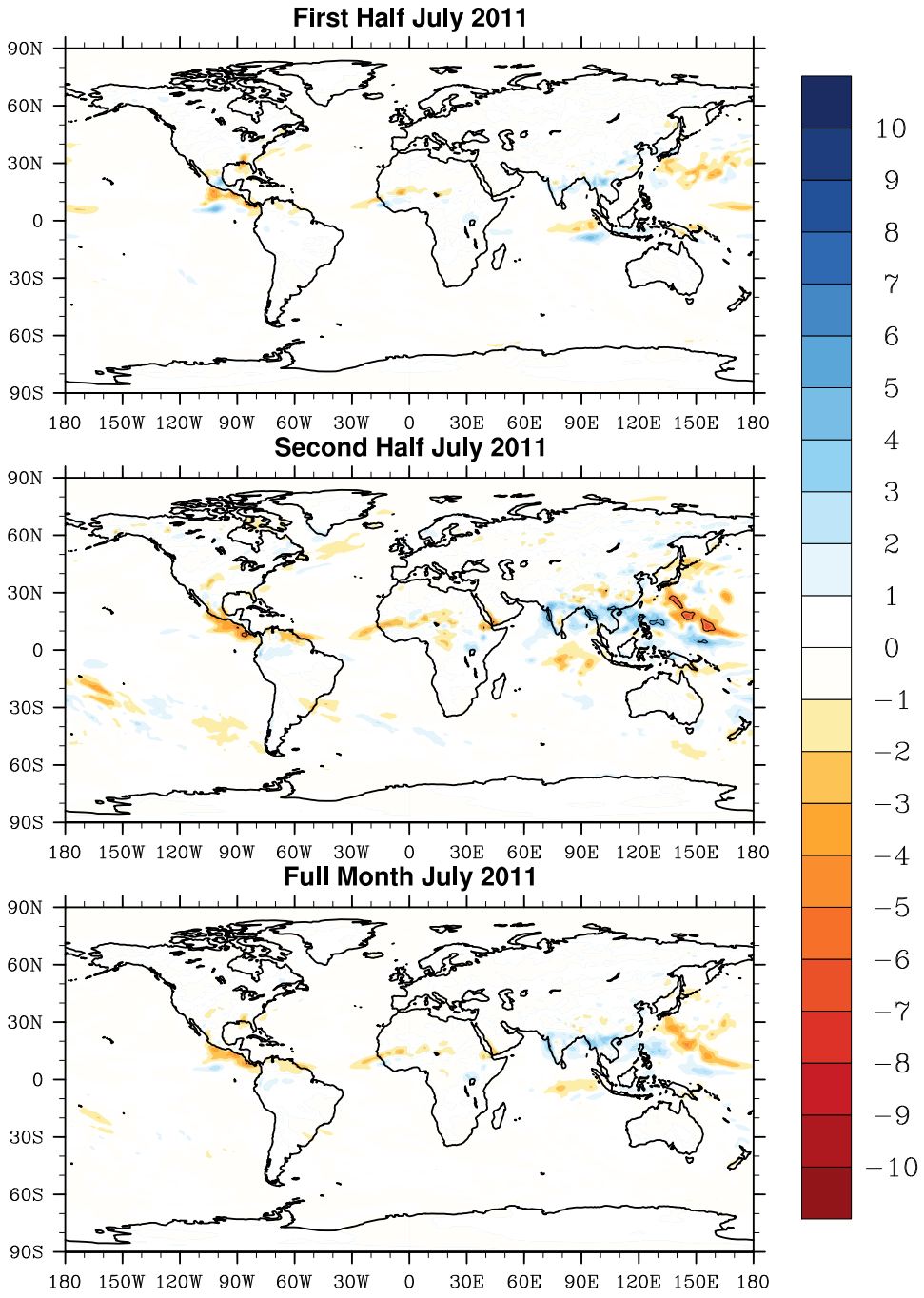

Figure 4.39: As in Fig. 4.38 but for July 2011.

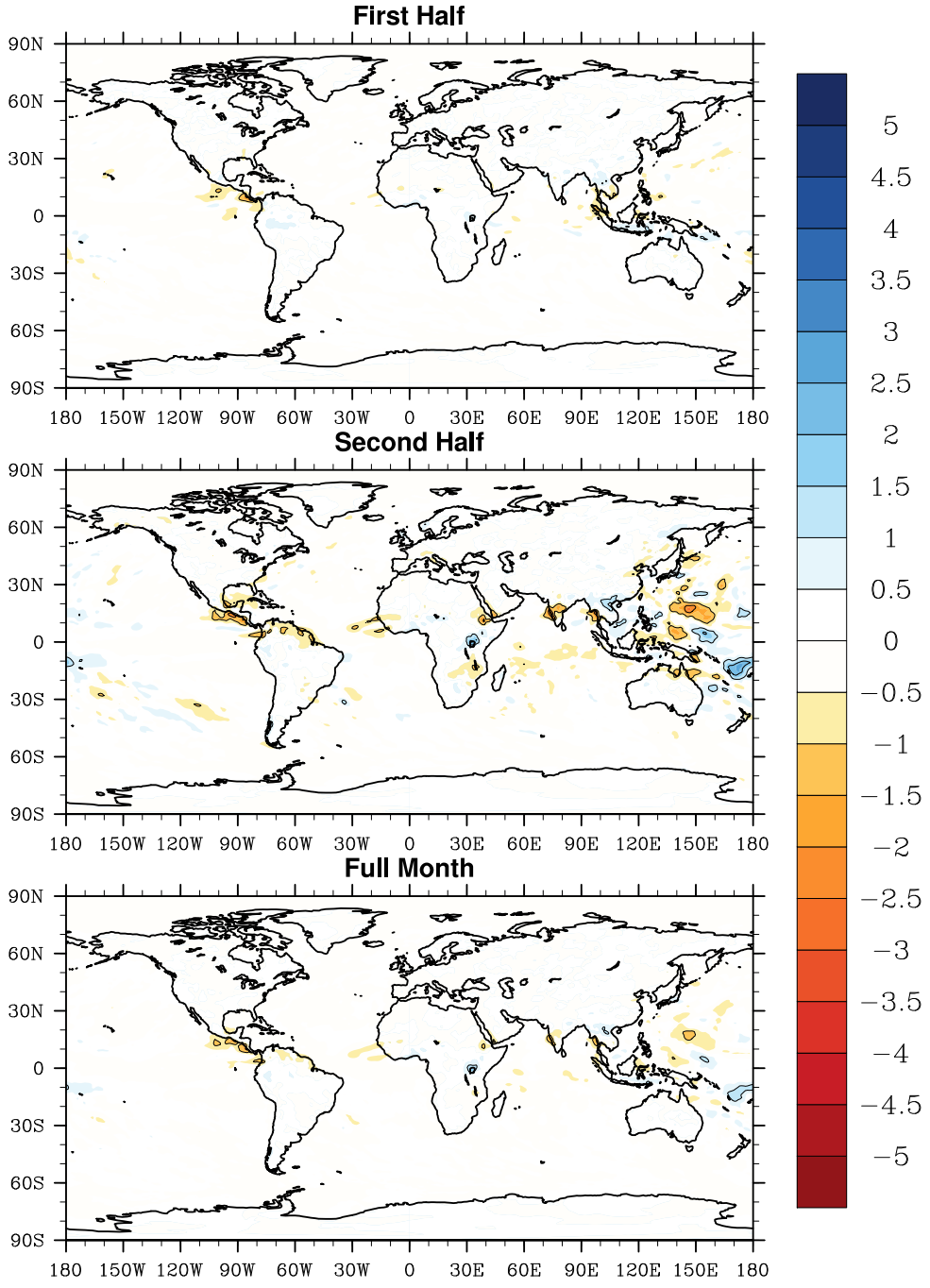

Figure 4.40: As in Fig. 4.38 but averaged over the simulated months. Contour lines every 1 mm/day

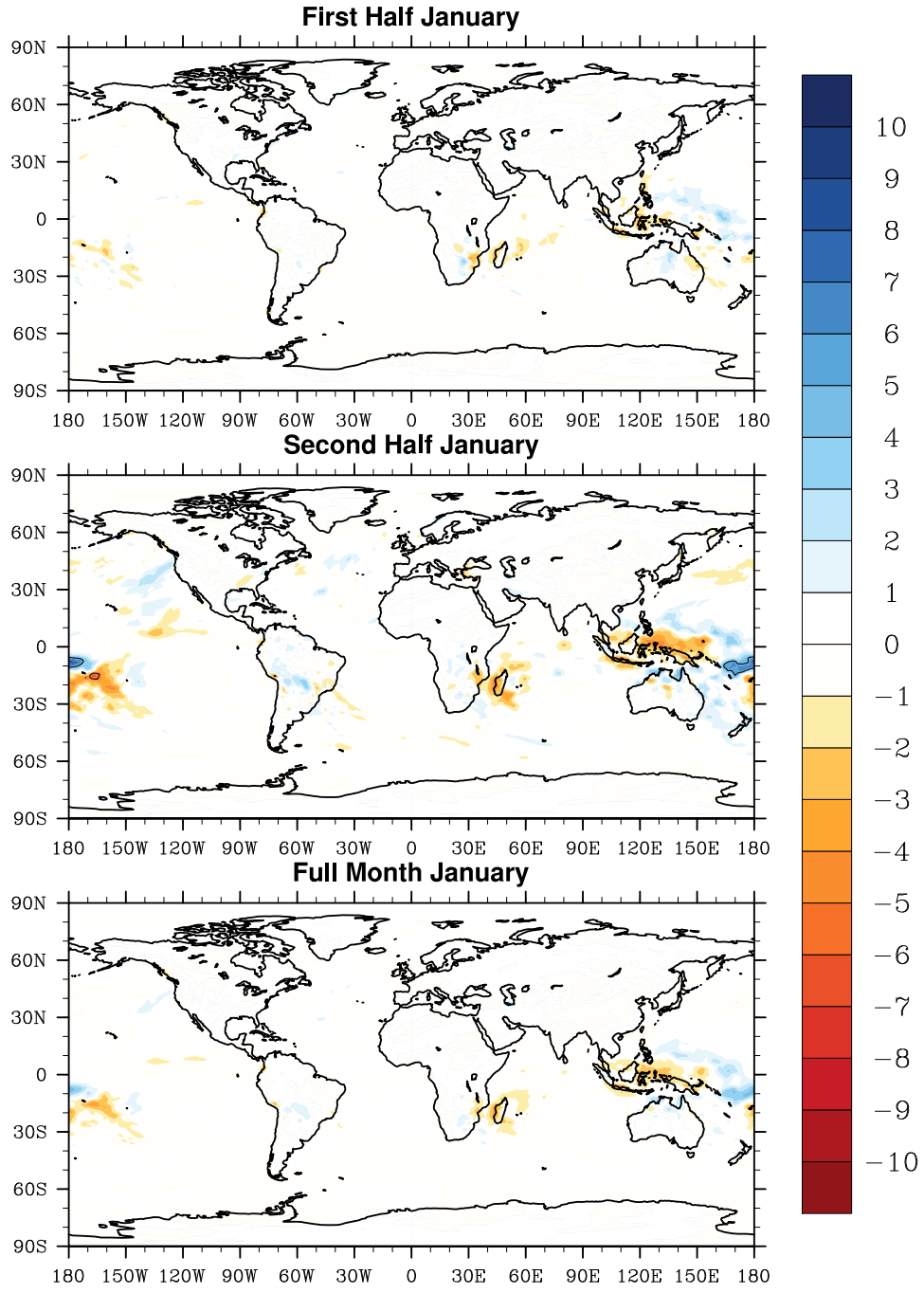

Figure 4.41: Global distribution of the differences in monthly reforecast ensemble mean of daily precipitation in January between the two methods (daily forced minus operational ocean model). The top panel refers to the first fifteen days, the middle panel to the second fifteen days and the bottom panel to the full month. Values are in mm/day. Countur lines every 5 mm/day.

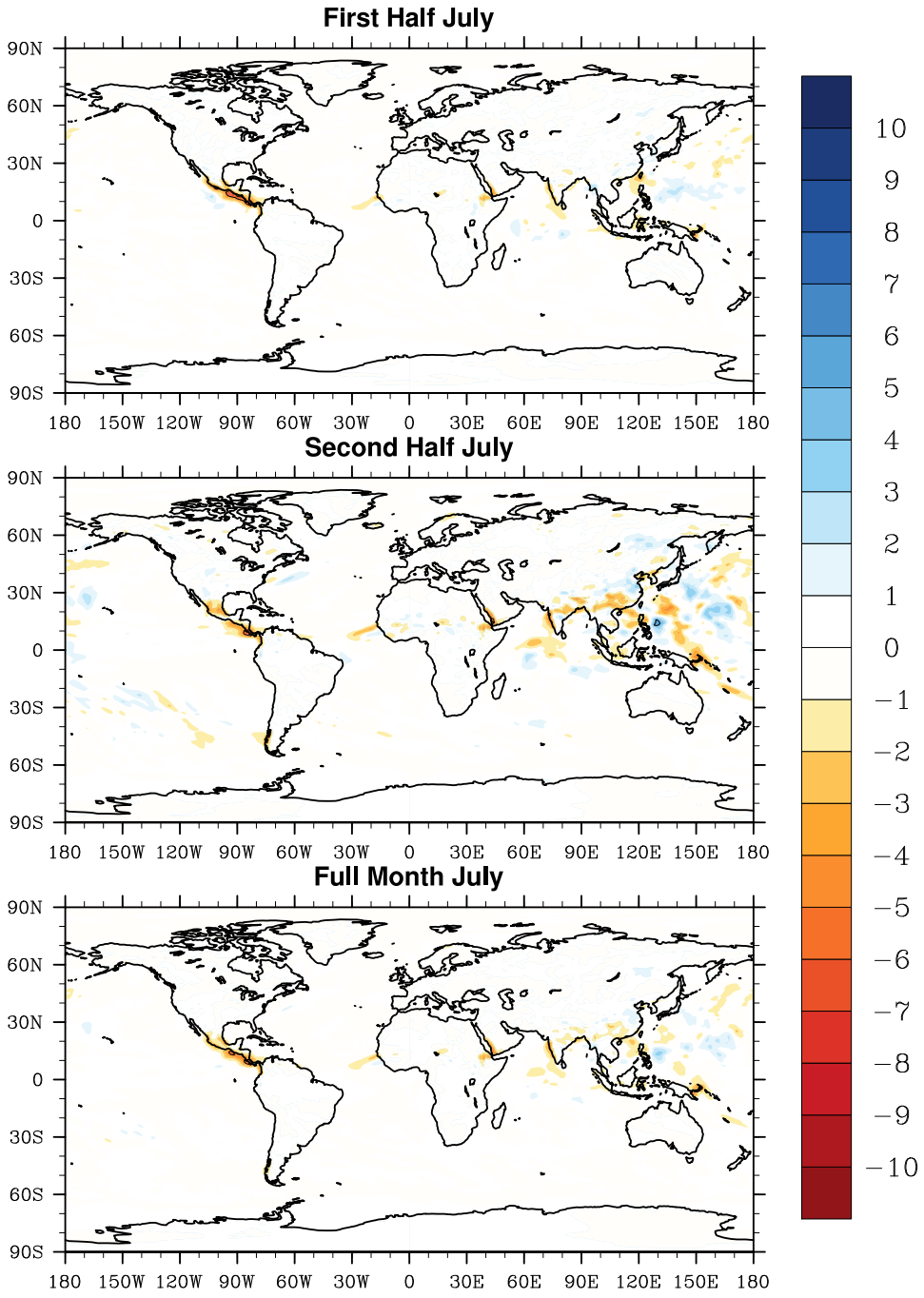

Figure 4.42: As in Fig. 4.41 but for July.

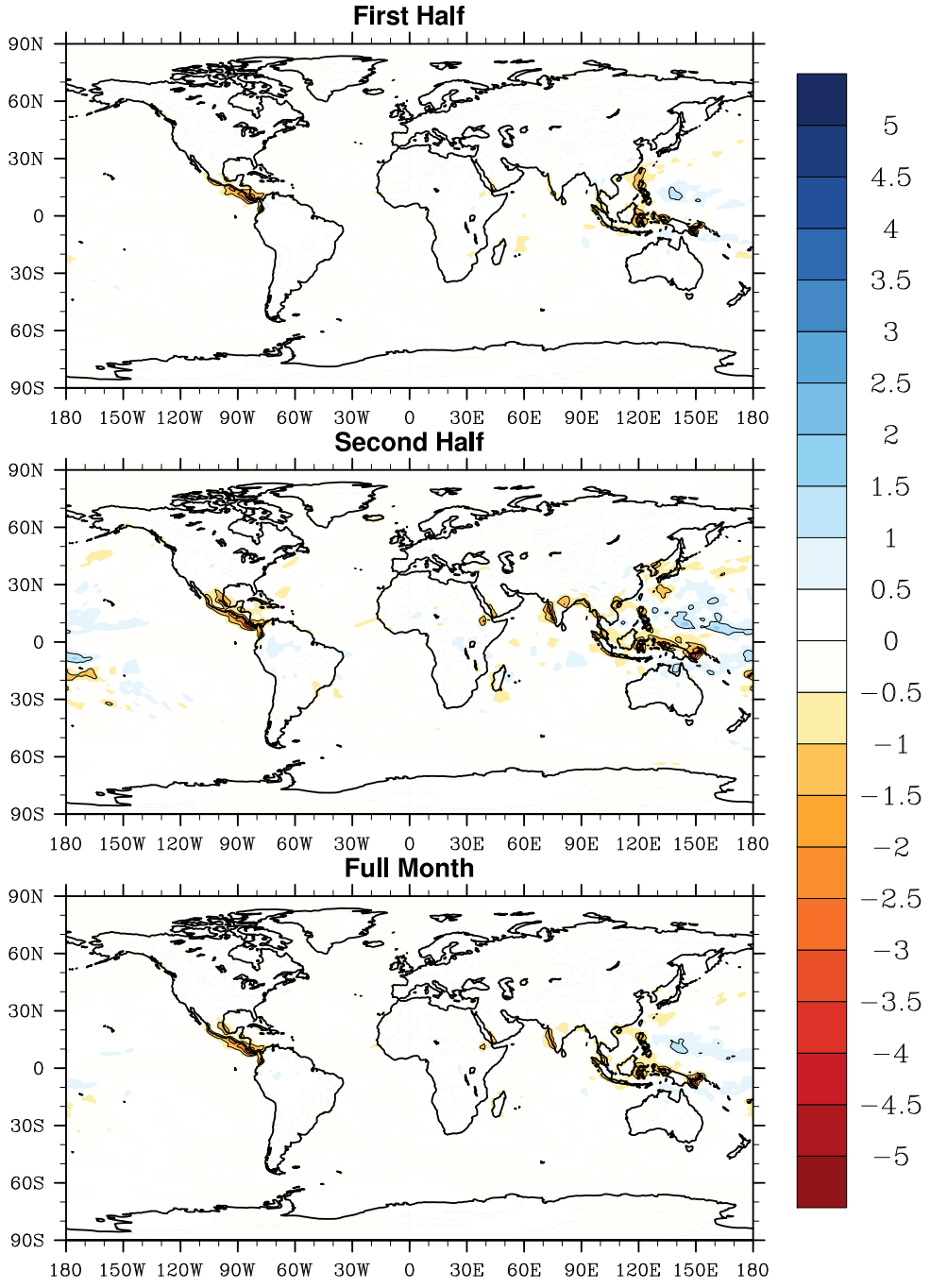

Figure 4.43: As in Fig. 4.41 but averaged over the simulated months. Countur lines every 1 mm/day.

Analysis of the atmospheric ensemble spread

An analysis of the ensemble spread for both forecast datasets is made here, to verify if there is a correlation between the spread in the predicted SST field and the spread of atmospheric variables. In this case, only geopotential height at 500 hpa and temperature at 850 hPa are examinated. The spread is computed using the standard deviation as follows:

$$\sigma_{15} = \sqrt{\frac{\sum_{i=1}^{N} \left(\bar{X}_{15}^{i} - \bar{X}_{15} \right)^2}{N}}$$

$$\sigma_{30} = \sqrt{\frac{\sum_{i=1}^{N} \left(\bar{X}_{30}^{i} - \bar{X}_{30} \right)^2}{N}}$$

where $\bar{X}_{15,30}^{i}$ are the individual ensemble members averaged over 15 and 30 days, and $\bar{X}_{15,30}$ are the ensemble means averaged over 15 and 30 days. Observation of the ensemble spread differences for the individual months reveals that there is a rather random spatial distribution (see fig. 4.44 – 4.45). In order to gain a more precise idea of the extent of the differences between the two models, a global average of the spread is computed for the first part, second part and the full month. The values are shown in tables 4.1 and 4.2. The highest value for each month is highlighted. There is a tendency to have a larger atmospheric spread when the new ocean model is used. This is more evident in the geopotential height, while for temperature spread differences are very small and present almost only in the second part of the month. The highest values in the first part of the month of April 2011 with respect to the other months are due to a longer period of integration (about 3 days more, see the introduction in chapter 3).

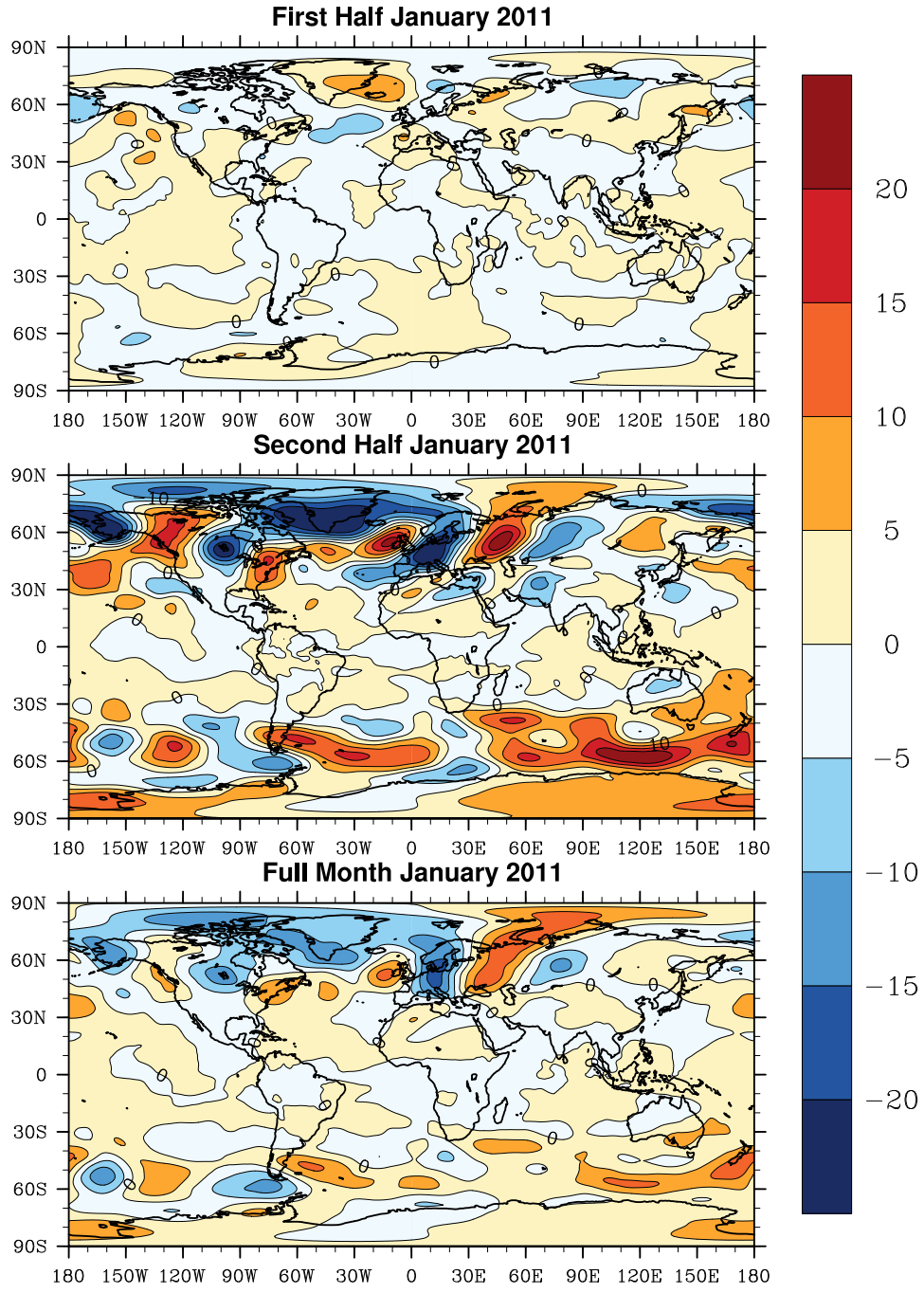

Figure 4.44: Global distribution of the differences in monthly forecast ensemble spread ($\sigma_{15,30}$) of geopotential height at 500 hPa in January 2011 between the two models (new minus operational). The top panel refers to the first fifteen days, the middle panel to the second fifteen days and the bottom panel to the full month. Values are in meters.

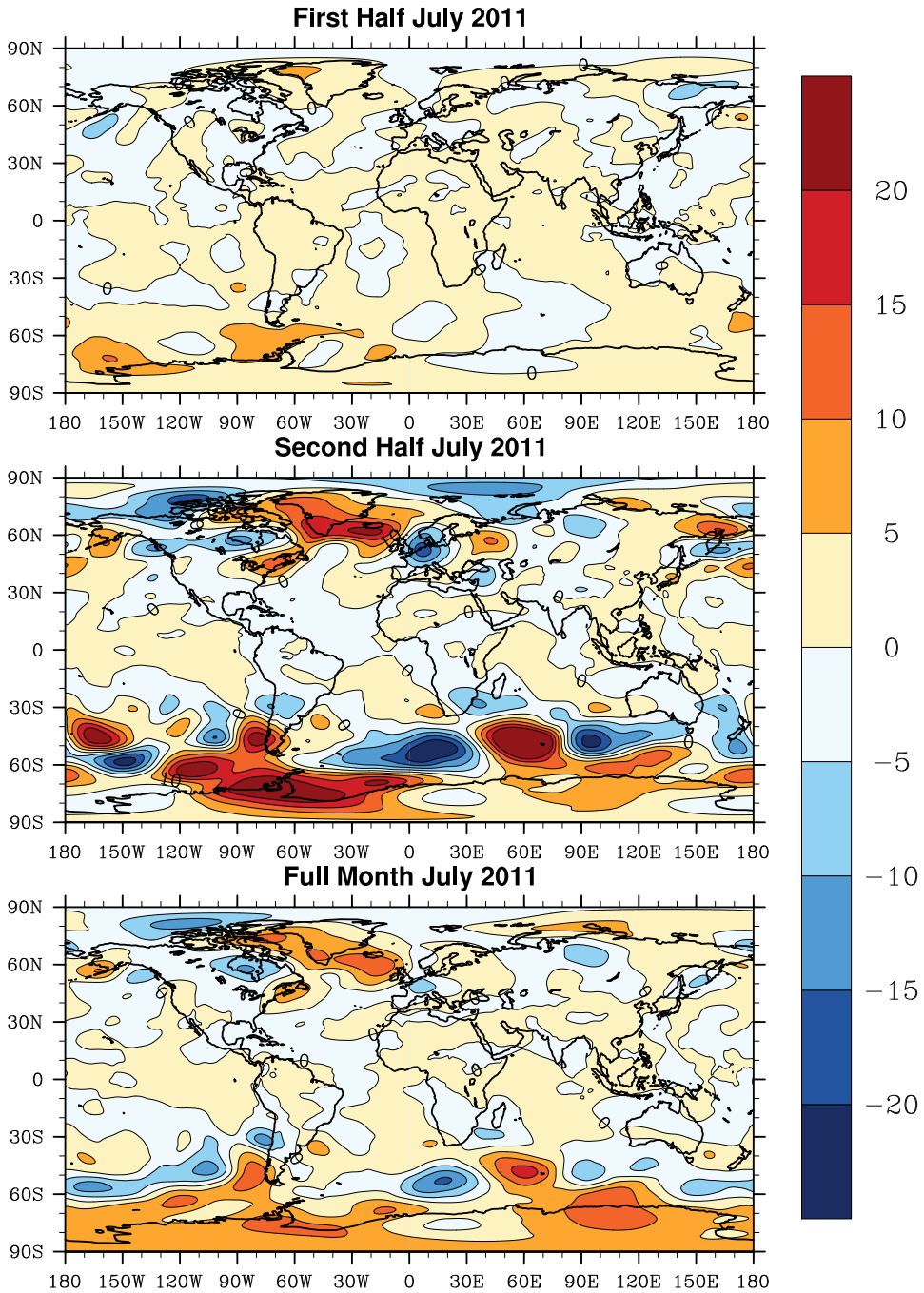

Figure 4.45: As in Fig. 4.44 but for July 2011.

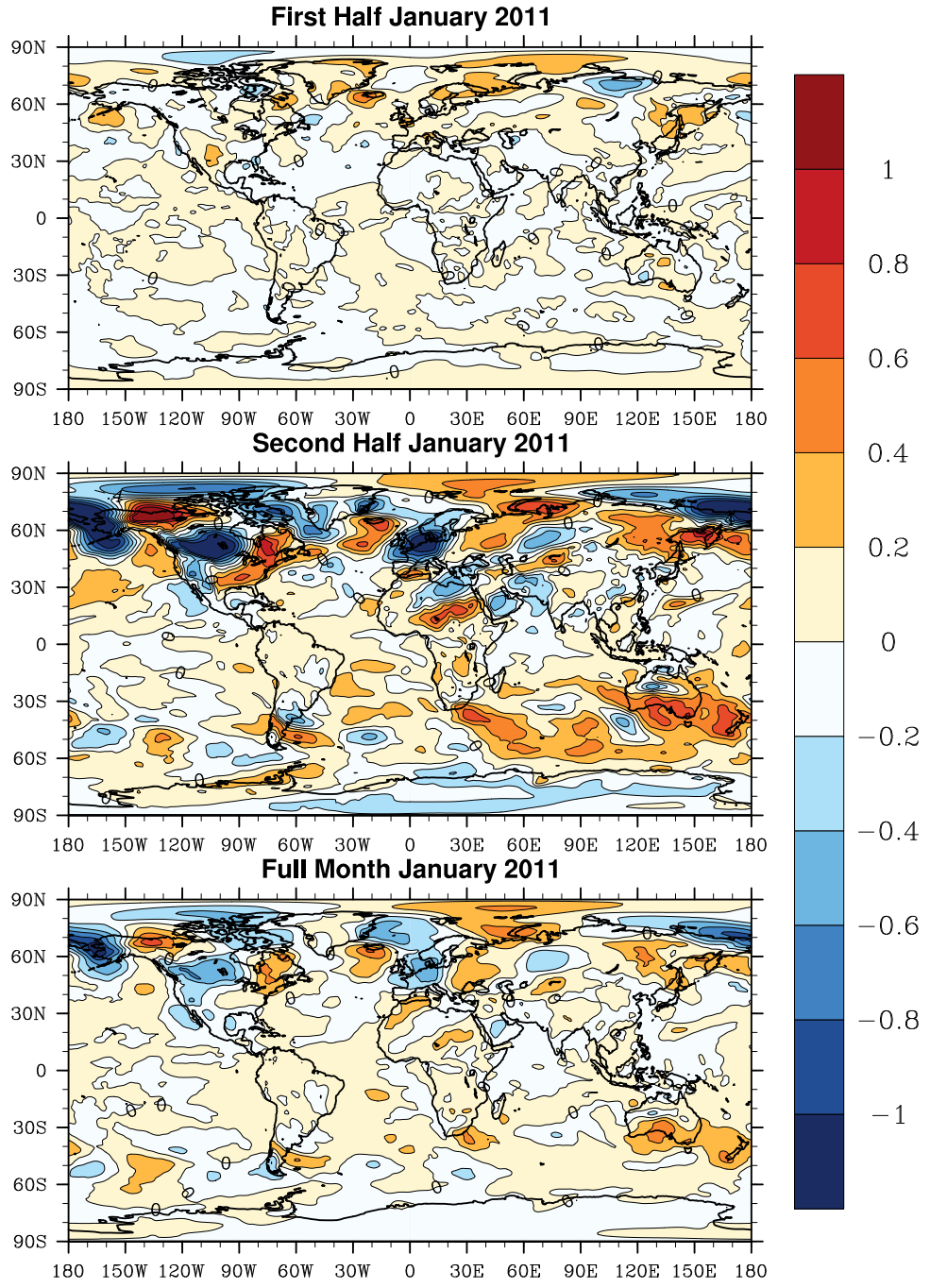

Figure 4.46: Global distribution of the differences in monthly forecast ensemble spread ($\sigma_{15,30}$) of temperature at 850 hPa in January 2011 between the two models (new minus operational). The top panel refers to the first fifteen days, the middle panel to the second fifteen days and the bottom panel to the full month. Values are in degrees Celsius.

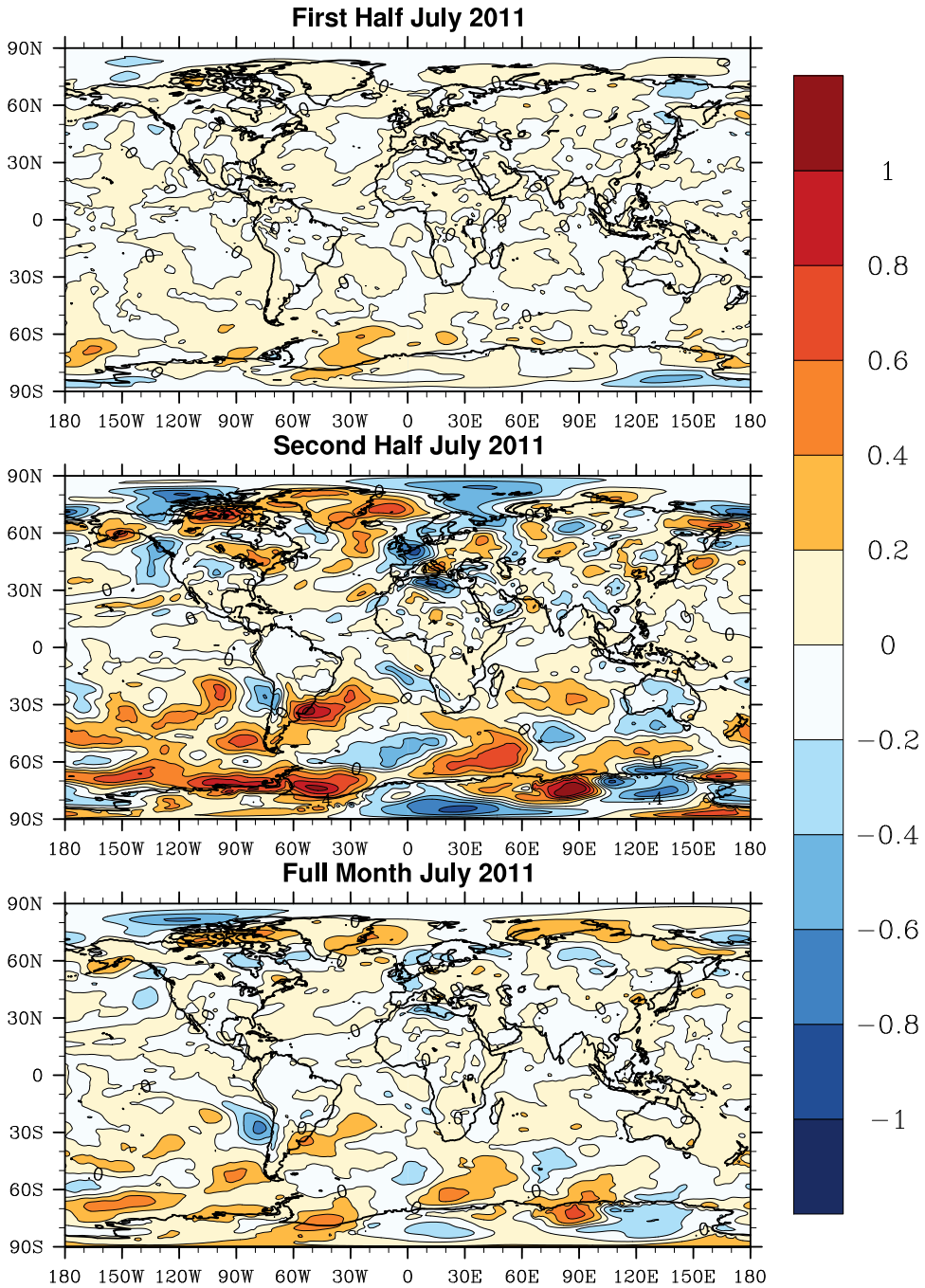

Figure 4.47: As in Fig. 4.46 but for July 2011.

$\sigma_{15,30}$ geopotential height at 500 hPa (m)						
Months	First Half		Second Half		Full Month	
	New	Op	New	Op	New	Op
January 2011	17.4	**17.6**	**31.6**	30.9	**19.0**	18.9
March 2011	16.4	**16.7**	**33.1**	32.3	**19.6**	19.3
April 2011	22.0	22.0	32.4	**32.6**	20.2	**20.7**
May 2011	**16.7**	16.6	33.1	**33.7**	19.1	**19.9**
June 2011	**17.7**	17.5	**32.3**	30.2	**19.2**	18.2
July 2011	**17.0**	16.6	**31.3**	30.7	**18.5**	18.1
August 2011	**16.2**	16.1	29.8	29.8	**18.0**	17.4

Table 4.1: Globally averaged geopotential height at 500 hPa spread for the three periods for all the month simulated

$\sigma_{15,30}$ temperature at 850 hPa (°C)						
Months	First Half		Second Half		Full Month	
	New	Op	New	Op	New	Op
January 2011	0.77	0.77	**1.05**	1.03	**0.81**	0.80
March 2011	0.74	0.74	1.06	1.06	0.81	0.81
April 2011	0.84	0.84	**1.05**	1.04	0.82	0.82
May 2011	0.75	0.75	1.04	1.04	0.79	**0.80**
June 2011	0.74	0.74	**0.99**	0.97	**0.76**	0.75
July 2011	0.72	0.72	**0.96**	0.94	**0.74**	0.73
August 2011	0.69	**0.70**	0.95	0.95	0.73	0.73

Table 4.2: As in table 4.1, but for temperature at 850 hPa

4.1.4 Additional sensitivity tests

A set of experiments have been carried out in which the γ parameter in equation (4.1) is modified in order to find the best model set up. In particular three different values have been tested:

$$\gamma = \begin{cases} 0, \\ 1/2.3 \quad days^{-1}, \\ 1/23 \quad days^{-1}. \end{cases}$$

Only the month of July 2011 has been simulated with these three different versions. The results show that if $\gamma = 0$ (corresponding to an infinite relaxation time scale) the largest spread in the SST ensemble is achieved, with the ensemble mean that is different from the ensemble mean of the SST obtained with the model version with $\gamma = 1/23\, days^{-1}$. However the monthly ensemble mean forecast error is larger than that obtained with the latter (not shown).

When $\gamma = 1/2.3\, days^{-1}$ the contribution of the residual fluxes vanishes and the SST simulated is very similar to that simulated by the operational model. In this case, there is no difference in using the flux correction. A relaxation time intermediate between 2.3 and 23 days could be the best set up, but the determination of a more precise value requires further exploration.

4.1.5 Anomaly forecast differences

In the section 4.1.3 we mentioned the similarity among the forecast difference patterns and the reforecast ones in the atmospheric fields. This means that when the anomaly forecast patterns are computed to issue the monthly forecasts, they are very similar comparing the new method with the operational one, especially in the first 15-days period. Some slightly more intense yet not significant differences are present in the second 15 days period. They do not modify much the final

anomalies in geopotential height and temperature. An exception is given by the second part of the month of March 2011, in which there are significant changes over Japan and over the North America sector. These changes are in the direction of the observed anomaly (fig. 4.48 – 4.49). In the operational model, large positive anomalies of geopotential height at 500 hPa and of temperature at 850 hPa are predicted over the Northern Pacific sector including Japan. On the other hand, with the new model the anomaly turns negative over Japan for both the variables as for the observations. Also the precipitation anomaly changes from wetter to drier over Japan. A change in precipitation anomaly quantity is near the west coast of USA and Canada. Hovewer, in the same area the anomaly change is less pronounced in geopotential height and in temperature.

In general, observing the other months, precipitation shows more significant differences in the second part with respect to geopotential height and temperature. This indicates a more important impact of the SST on precipitation as already found in section 4.1.3. This analysis exhibits some good indications about the use of this new ocean model, but a generalization is not applicable to the results.

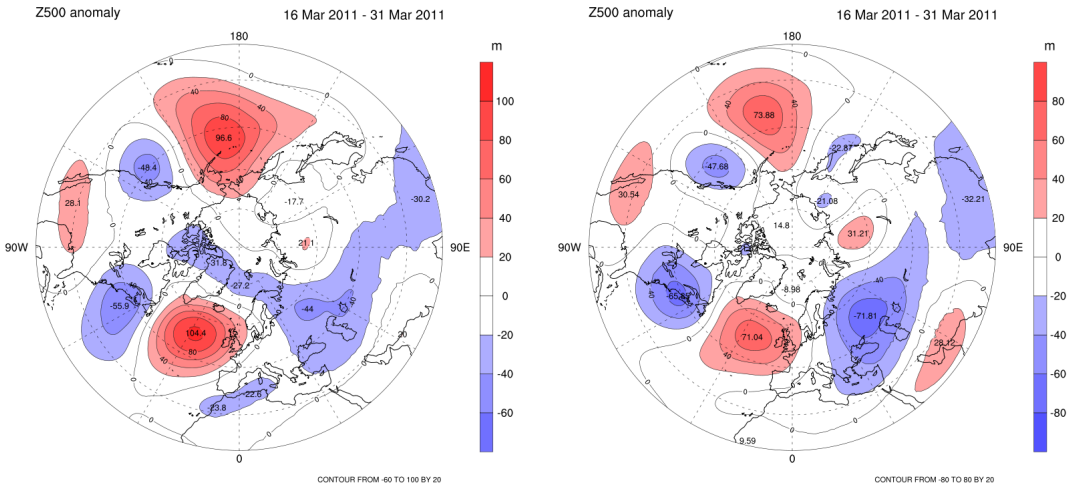

(a) Operational model

(b) New model

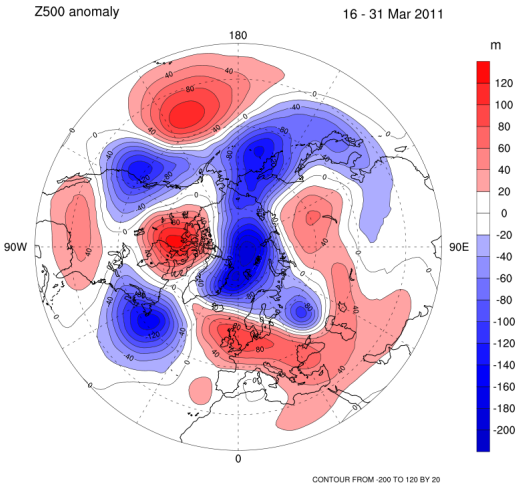

(c) Observed

Figure 4.48: Geopotential height anomaly forecast at 500 hPa for the period 16-31 of March 2011. a) From the operational model, b) from the new model, c) observed anomaly (from ERA-Interim dataset)

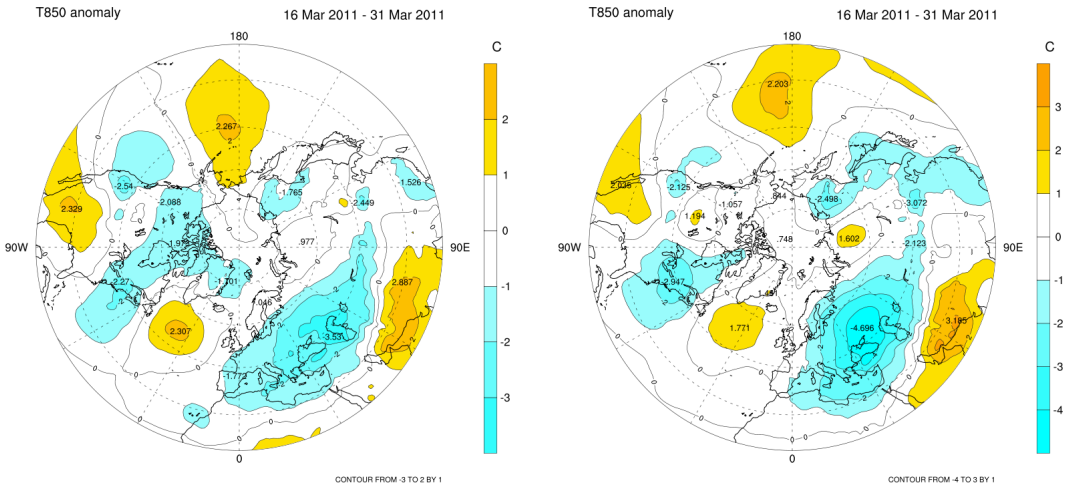

(a) Operational model

(b) New model

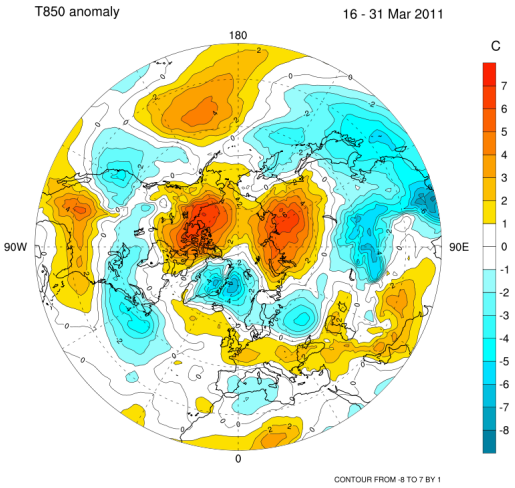

(c) Observed

Figure 4.49: Temperature anomaly forecast at 850 hPa for the period 16-31 of March 2011. a) From operational model, b) from new model, c) observed anomaly (from ERA-Interim dataset)

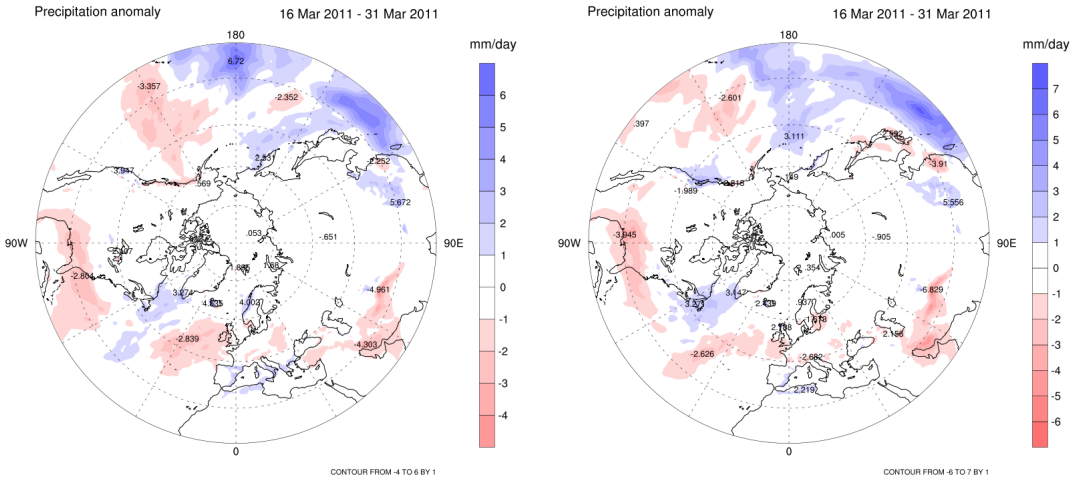

(a) Operational model

(b) New model

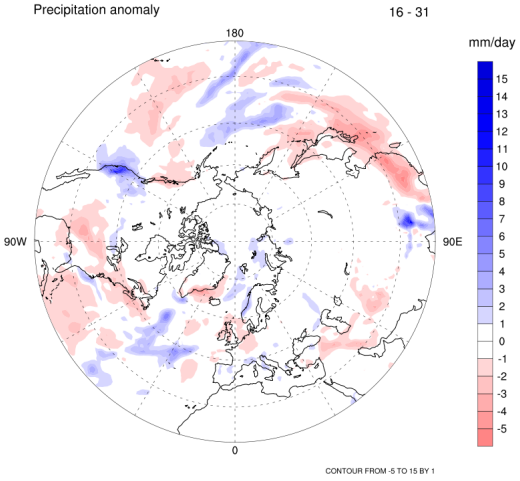

(c) Observed

Figure 4.50: Precipitation anomaly forecast for the period 16-31 of March 2011. a) From operational model, b) from new model, c) observed anomaly (from ERA-Interim dataset)

Conclusions

The present thesis deals with the extended-range atmospheric forecasts, and in particular with the implementation of a new simple slab mixed layer ocean model to simulate the evolution of sea surface temperature which is used to force the atmospheric global model GLOBO, with the aim of improving the quality of the monthly forecasts produced at ISAC-CNR.

SST modelling solutions

In the first part, the study is focused on evaluating the problems connected with the influence of SST on the time scale of one month. Some studies have found that a better simulation of the SST could improve the prediction skill of the MJO (Takaya et al., 2010), and that strong horizontal gradients of SST can affect the local trophosperic dynamics (Minobe et al., 2008).

We investigated the possible modelling solutions to simulate SST in a monthly forecasting system in relation to the available computing resources, starting from simple persistence, considering possible correlations with mixed layer depth and surface net heat fluxes and exploring the capabilities of statistical and dynamical models.

The analysis has brought to the conclusions that there is no preferable solution to represent the ocean. Persistence on the time scale of the order of one month has good potential skill in some areas like the Equatorial Pacific, but little skill in western boundary currents areas. The correlation of the SST with the mixed

layer depth and the contribution of surface net heat fluxes to the climatological SST tendency have shown large spatial and time variability.

Dynamical models (columnar or full 3D ocean models) have been analyzed only qualitatively. They can represent ocean dynamics like the SST diurnal cycle or upwelling effects, but they require reliable initial analysis (adding also the salinity) and more computational resource. Moreover they suffer of drift from climatology. After this examination, a modification in the existing simple ocean mixed layer model that is used in operational monthly forecasting system has been considered and applied using a flux correction term described in the last section.

Evaluation of the GLOBO model systematic errors and improvements

In the second part of the thesis, after describing the characteristics of the atmospheric global circulation model GLOBO, we made an analysis of the performance and systematic errors of the model in long term simulations. Ten years were simulated using a climatological boundary forcing of SST, sea ice cover, soil temperature and moisture, and compared with a similar time range of obervations from the ERA-Interim dataset. The first results showed that the annual mean patterns of some atmospheric horizontal fields (mean sea level pressure, geopotential heigth at 500 hPa, precipitation, temperature at 850, etc) were represented by the model with systematic errors comparable with those found in similar models (Gates et al., 1998; Jung and Tompinks, 2003; Martin et al., 2005). The same occured for the zonal means of zonal wind, temperature and relative humidity. These systematic errors indicated that the model atmosphere was about 1-2 °C colder and that suffered of a more zonal circulation than observed. Precipitation showed also a tendecy to be overestimated in the Tropics and in the Sahel, with a negative bias in the Indian Ocean, that is present, however, in many atmospheric models.

After this analysis, some sensitivity tests were made with the aim of reducing

systematic errors. This was obtained modifying the radiation, the convection scheme, the turbulence parameterization and adding a orographyc gravity wave drag parameterization scheme. Moreover an improvement in the numerical stability of the code and in the treatment of singularities at poles by means of a digital filter has been carried out (Malguzzi et al., 2011). After these changes, the model was considered suitable for producing extended range forecasts.

The new ocean model and the results of numerical experiments

In the last part of the thesis, after introducing the techniques adopted for the ensemble monthly forecasting system implemented at ISAC-CNR, we focused on the procedure that simulates the SST. A new version of the simple ocean mixed layer model used in the operational forecasts is presented. This new model uses a flux correction term and an increased relaxation time scale to climatology, with respect to the operational model. The flux correction term is introduced in the following way. The heating contribution from net surface heat fluxes forcing the atmospheric model in reforecast mode, with daily observed SST and sea ice cover, is computed. Then it is subtracted from climatological ocean heat changes computed from SST climatological tendency.

The results of numerical experiments, in which this new version of the ocean model has been used, have been presented and discussed. Seven months of 2011 were simulated and the results compared with those obtained through the operational forecasts. They show that a large increase in the spread of the ensemble forecast of the SST is obtained as a result of the new method. Moreover a more realistic evolution than the operational ocean model is observed. Considering the global oceans, the new model produces warmer (colder) SST in the winter (summer) hemisphere, and a persistent colder SST in the equatorial belt. A similar but less intense pattern is visible in the difference between the two reforecast datasets. A comparison with observations shows that the ensemble mean forecast error is

similar or slightly larger than the operational one, given the larger variability due to the larger spread of the simulated SST. The ensemble spread simulated by the new model, evaluated in terms of internal variability, is in general smaller than the observed one. However the differences are very small and the patterns match very well, in particular over the Northern Hemisphere.

Recently a new comparison made with observations obtained from Global Forecast System (GFS) analysis has shown that the new model has a better performance than operational model in every simulated month. This indicates that the results are too dependent from the reference analysis. A more reliable one would be necessary to verify a SST forecast with an accuracy required by the model error variability.

Regarding the atmospheric fields (geopotential height at 500 hPa, temperature at 850 hPa and precipitation), we note that the differences between the new and the operational forecasts increase during the integration period, with the largest differences observed in the second part of the month. In the first 15 days, the differences are negligible, except for precipitation in some cases. This could mean that a signal in the SST can influence the atmosphere after 15-20 days. The largest differences are present in the middle and high latitudes for the Z500 and T850, and in the tropical belt for precipitation. However similar patterns, even if less intense, appear in the differences between the two reforecast ensemble means. Thus, when we compute the predicted anomalies with the two forecasting methods, small differences in the anomaly patterns can be noticed, larger in the second part of the month, but still apparently not significant.

An additional analysis has been carried out regarding the differences in the atmospheric variables ensemble spread between the new and the operational model. The difference pattern is not uniform over the globe, but in global averages there is a little increase in the spread when the new model is used. Therefore a larger variability in the SST ensemble contributes to increasing atmospheric model

ensemble spread.

Finally, a series of sensitivity tests has been made to find the best model set up, as a function of the relaxation time. When the relaxation time scale is set to infinity (i.e. the relaxation term is not used), the SST ensemble spread is maximum, but the ensemble mean forecast error is worser than that obtained with a time scale of about 23 days. On the other hand, setting the relaxation time scale to the value of the operational model (about 2.3 days), the contribution of the residual fluxes vanishes and the SST simulated is very similar to the operational one. A relaxation time of about 10 days seems therefore to be the best compromise for obtaining a larger spread and, at the same time, a better forecast error. This should be verified extending the present study.

Further studies also should include the verification of the GLOBO ensemble simulations, targeted to specific low-frequency phenomena relevant for the monthly scale variability, as the MJO. This requires a large number of additional simulations. The coupling with oceans model of increasing complexity should be investigated as well, in order to evaluated possible "pros and cons" with respect to the simple ocean modelling approach considered in this thesis.

Bibliography

Anderson, J. L. and H. M. Van den Dool, 1994: Skill and return of skill in dynamic extended-range forecasts. *Mon. Wea. Rev.*, **122**, 507–516.

Baines, P. G., 1995: *Topographic Effects in Stratified Flows.*, Cambridge Monographs on Mechanics, Cambridge University Press, 482pp.

Baldwin, M. P., D. B. Stephenson, D. W. J. Thompson, T. J. Dunkerton, A. J. Charlton, and A. O'Neil, 2003: Stratospheric memory and extended-range weather forecast. *Science*, **301**, 317–318.

Balmaseda, M. A., O. J. Alves, A. Arribas, T. Awaji, D. W. Behringer, N. Ferry, Y. Fujii, T. Lee, M. Rienecker, T. Rosati, and D. stammer, 2009: Ocean initialization for seasonal forecasts. *Oceanography*, **22**, 154–159.

Behringer, D. W. and Y. Xue, 2004: Evaluation of the global ocean data assimilation system at NCEP: The Pacific Ocean., *Eight Symposium on Integrated Observing and Assimilation Systems for Atmosphere, Oceans, and Land Surface*, AMS 84th Annual Meeting, Washington State Convention and Trade Center, Seattle, Washington.

Beljaars, A. C. M. and M. Holtslag, 1991: On flux parameterization over land surface for atmospheric models. *J. Atmos. Sci.*, **30**, 327–341.

Berrisford, P., D. P. Dee, K. Fielding, M. Fuentes, P. Kå llberg, S. Kobayashi,

and S. M. Uppala, 2009: The ERA-Interim Archive, Tech. Rep. 1, ECMWF, Reading, UK.

Billet, S. and E. F. Toro, 1997: On WAF-type schemes for multidimensional hyperbolic conservation laws. *J. Comput. Phys.*, **130**, 1–24.

Blackadar, A. K., 1962: The vertical distribution pf wind and turbulent exchange in a neutral atmosphere. *J. Geophys. Res.*, **67**, 3095–3102.

Bougeault, P. and P. Lacarrere, 1989: Parameterization of orography-induced turbulence in a meso-betascale model. *Mon. Wea. Rev.*, **117**, 1872–1890.

Cassou, C., 2008: Intraseasonal interaction between the Madden-Julian Oscillation and the North Atlantic Oscillation. *Nature*, **455**, 523–527.

Corti, S., S. Gualdi, and A. Navarra, 2003: Analysis of the mid-latitude weather regimes in the 200-year control integration of the SINTEX model. *Ann. Geophys.*, **46**, 27–37.

Craddock, J. M., H. Flohn, and J. Namias, 1962: *The present status of long-range forecasting in the world*, no. 126, WMO.

Cuxart, A. A., M. Holtslag, R. J. Beare, E. Bazile, A. Beljaars, A. Cheng, L. Conangla, M. Ek, F. Frredman, R. Hamd, A. Kerstein, H. Kitagawa, G. Lenderink, D. Lewellen, J. Mailhot, T. Mauritsen, V. Perov, G. Shayes, G. J. Steeneveld, G. Svensson, P. Taylor, W. Weng, S. Wunsch, and K. M. Xu, 2006: Single Column Model Intercomparison for a Stably Stratified Atmospheric Boundarly Layer. *Boundary Layer Meteorology*, **118**, 273–303.

de Boyer Montegut, C., C. Madec, A. S. Fischer, A. Lazar, and D. Iudicone, 2004: Mixed layer depth over global ocean: An examination of profile data and a profile-based climatology. *J. Geophys. Res.*, **109**.

Epstein, E. S., 1969: stochastic dynamic prediction. *Tellus*, **21**, 739–759.

Feagle, G. and A. Businger, 1980: *An introduction to atmospheric physics.*, vol. 25 of *International Geophysics Series*, Academic Press, 432pp.

Ferranti, L., T. N. Palmer, F. Molteni, and E. Klinker, 1990: Tropical-extratropical interaction associated with the 30-60 day oscillation and its impact on medium and extended range prediction. *J. Atmos. Sci.*, **47**, 2177–2199.

Ferretti, R., T. Paolucci, W. Zheng, G. Visconti, and P. Bonelli, 2000: Analyses of the precipitation pattern on the Alpine region using different cumulus convection parameterizations. *J. Appl. Meteor.*, **39**, 182–200.

Gates, W. L., J. S. Boyle, C. C. Covey, C. G. Dease, C. M. Doutriaux, R. S. Drach, M. Fiorino, P. J. Gleckler, J. J. Hnilo, S. M. Marlais, T. J. Phillips, G. L. Potter, B. D. Santer, K. R. Sperber, K. E. Taylor, and D. N. Williams, 1998: An overview of the results of the Atmospheric Model Intercomparison Project AMIP I. *Bull. Amer. Meteorol. Soc.*, **80**, 29–55.

Giorgi, F., 2005: Climate Change Prediction. *Climatic Change*, **73**, 239–265, DOI: 10.1007/s10584-005-6857-4.

Hendon, H. H. and B. Liebmann, 1990: The intraseasonal (30 – 50 day) oscillation of the Australian summer monsoon. *J. Atmos. Sci.*, **47**, 2909–2923.

Hubbard, M. E. and N. Nikiforakis, 2003: A three-dimensional adaptive, Godunov-type model for global atmospheric flows. *Mon. Wea. Rev.*, **131**, 1848–1864.

Hudson, D., O. Alves, H. H. Hendon, and A. G. Marshall, 2011a: Bridging the gap between weather and seasonal forecasting: intraseasonal forecasting for Australia. *Q. J. R. Meteorol. Soc.*, **137**, 673–689.

Hudson, D., A. G. Marshall, and O. Alves, 2011b: Intraseasonal forecasting of the 2009 summer and winter Australian heat waves using POAMA. *Weather and Forecasting*, **26**, 257–279.

Jung, T. and J. Barkmeijer, 2006: Sensitivity of the tropospheric circulation to changes in the strength of the stratospheric polar vortex. *Mon. Wea. Rev.*, **134**, 2191–2207.

Jung, T. and A. Tompinks, 2003: Systematic errors in the ECMWF forecsting system., Tech. rep., ECMWF, Reading, UK.

Kain, J., 2004: The kain-fritsch convective parameterization: an update. *J. App. Meteorol.*, **43**, 170–181.

Kain, J. and J. Fritsch, 1990: A one-dimensional entraining/detraining plume model and its application in convective parameterization. *J. Atmos. Sci.*, **47**, 2784–2802.

Koster, R. D., S. P. P. Mahanama, T. J. Yamada, G. Balsamo, A. A. Berg, M. Boisserie, P. A. Dirmeyer, F. J. Doblas-Reyes, G. Drewitt, C. T. Gordon, Z. Guo, J.-H. Jeong, D. M. Lawrence, W.-S. Lee, Z. Li, L. Luo, S. Malyshew, W. J. Merryfield, S. I. Seneviratne, T. Stanelle, B. J. J. M. Van den Hurk, F. Vitart, and E. F. Wood, 2010: Contribution of land surface initialization to subseasonal forecast skill: First results from a multi-model experiment. *Geophys. Res. Lett.*, **37**, L02402, doi:10.1029/2009GL041677.

Kug, J.-S., J.-Y. Lee, and I.-S. Kang, 2007: Global sea surface temperature prediction using a multi-model ensemble. *Mon. Wea. Rev.*, **135**, 3239–3247.

Kuo, Y. H., R. J. Reed, and Y. Liu, 1996: The ERICA IOP5 storm. part III: Mesoscale cyclogenesis and precipitation parameterization. *Mon. Wea. Rev.*, **124**, 1409–1434.

Large, W. G., J. C. McWilliams, and S. C. Doney, 1994: Oceanic vertical mixing: A review and a model with nonlocal boundary layer parameterization. *Rev. Geophys.*, **32**, 363–403.

Large, W. G. and S. Pond, 1981: Open ocean momentum flux measurements in moderate to strong winds. *J. Phys. Oceanogr.*, **11**, 324–336.

Leith, C. E., 1974: Theoretical skill of Monte Carlo forecasts. *Mon. Wea. Rev.*, **101**, 701–721.

Lorenz, E. N., 1969: The predictability of a flow which possesses many scales of motion. *Tellus*, **11**, 290–307.

Lorenz, E. N., 1975: *Climate predictability: the physical basis of climate modeling.*, vol. 16 of *GARP Publ. Ser.*, WMO, pp. 132–136.

Madden, R. A. and P. R. Julian, 1971: Detection of a 40-50 day oscillation in the zonal wind in the tropical Pacific. *J. Atmos. Sci.*, **28**, 702–78.

Madden, R. A. and P. R. Julian, 1972: Description of global-scale circulation cells in the tropics with a 40 – 50 day period. *J. Atmos. Sci.*, **29**, 1109–1123.

Madden, R. A. and P. R. Julian, 1994: Observations of the 40 – 50 day tropical oscillation: A review. *Mon. Wea. Rev.*, **112**, 814–837.

Malguzzi, P., A. Buzzi, and O. Drofa, 2011: The Meteorological Global Model GLOBO at the ISAC-CNR of Italy Assessment of 1.5 yr of Experimental Use for Medium-Range Weather Forecasts. *Wea. and For.*, accepted, in press.

Malguzzi, P., O. Drofa, and A. Buzzi, 2007: Valutazione dell' errore di previsione della versione globale del modello BOLAM., *Convegno Nazionale di Fisica della Terra Fluida ed Affini, June 11th-15th, Ischia, Italy.*

Martin, G. M., M. A. Ringer, V. D. Pope, A. Jones, C. Dearden, and T. J. Hinton, 2005: The phisical properties of the atmosphere in the new Hadley Centre Global Environmental Model (HadGEM1). part I: Model description and global climatology. *J. Clim.*, **19**, 1274–1301.

Matthews, A. J., 2004: Intraseasonal variability over tropical Africa during northern summer. *J. Clim.*, **17**, 2427–2440.

Minobe, S., A. Kuwano-Yoshida, N. Komori, S.-P. Xie, and R. J. Small, 2008: Influence of the Gulf Stream on the troposphere. *Nature*, **452**, 206–209.

Miyakoda, K., T. Gordon, R. Caverly, W. Stern, J. Sirutis, and W. Bourke, 1983: Simulation of a blocking event in January 1977. *Mon. Wea. Rev.*, **111**, 846–869.

Miyakoda, K., J. Sirutis, and J. Ploshay, 1986: One month forecast experiment without anomaly boundary forcing. *Mon. Wea. Rev.*, **114**, 2363–2401.

Mlawer, E. J., S. J. Taubman, P. D. Brown, M. J. Iacono, and S. A. Clough, 1997: Radiative transfer for inhomogeneous atmospheres: RRTM, a validated correlated-k model for the long-wave. *J. Geophys. Res.*, **102D**, 16663–16682.

Molteni, F., U. Cubasch, and S. Tibaldi, 1986: 30- and 60-day forecast experiments with the ECMWF spectral models, *Proc. ECMWF Workshop on Predictability in the Medium and Extended Range*, ECMWF.

Monin, A. S. and A. Obukhov, 1955: Basic laws of turbulence mixing in the surface layer of the atmosphere. *Trudy Geophy. Inst.*, **24**, 163–187, aN SSSR.

Morcrette, J. J., 1991: Radiation and cloud radiative properties in the ECMWF operational weather forecast model. *J. Geophys. Res.*, **96D**, 9121–9132.

Neale, R. B., J. H. Richter, A. J. Conley, S. Park, P. H. Lauritzen, A. Gettelman, D. L. Williamson, P. J. Rasch, S. J. Vavrus, M. A. Taylor, W. D. Collins,

M. Zhang, and S.-J. Lin, 2010: Description of the NCAR Community Atmosphere Model (CAM 4.0)., Tech. rep., NCAR, nCAR Technical Note.

Newman, M., P. D. Sardeshmukh, C. R. Winkler, and J. S. Whitaker, 2003: A study of subseasonal predictability. *Mon. Wea. Rev.*, **131**, 1715–1732.

Palmer, T. N. and Z. Sun, 1985: A modelling and observational study of the relationship between sea surface temperature in the North-West atlantic and the atmospheric general circulation. *Q. J. R. Meteorol. Soc.*, **111**, 947–975.

Pasqui, M., L. Genesio, A. Crisci, J. Primicerio, R. Benedetti, and G. Maracchi, 2007: An adaptive multi-regressive method for summer seasonal forecast in the mediterranean area., Texas, 87th AMS Annual Meeting, 13–16 January 2007.

Reynolds, R. W., N. A. Rayner, T. M. Smith, M. Thomas, D. C. Stokes, and W. Wang, 2002: An improved in situ satellite SST analysis for climate. *J. Climate*, **15**, 73–87.

Ritter, B. and J. F. Geleyn, 1992: A comprehensive radiation scheme for numerical weather prediction models with potential applications in climate simulations. *Mon. Wea. Rev.*, **120**, 303–325.

Saha, S., S. Moorthi, X. Wu, J. Wang, N. S., P. Tripp, H.-L. Pan, D. Behringer, Y.-T. Hou, I. M. Chuang, H., M. Ek, J. Meng, R. Yang, H. van den Dool, Q. Zhang, W. Wang, and M. Chen, 2011: The NCEP Climate Forecast System version 2. *J. of Clim.*, to be submitted.

Schultz, P., 1995: An explicit cloud physics parameterization for operational numerical weather prediction. *Mon. Wea. Rev.*, **123**, 3331–3343.

Shapiro, R., 1970: Smoothing, filtering and boundary effects. *Rev. Geophys. Space Phys.*, **8**, 359–387.

Takaya, Y., F. Vitart, G. Balsamo, M. Balmaseda, M. Leutbecher, and F. Molteni, 2010: Implementation of an ocean mixed layer model in IFS, Tech. Rep. 622, ECMWF, Reading, UK.

Tegen, I., P. Hollrig, M. Chin, I. Fung, D. Jacob, and J. Penner, 1997: Contribution of different aerosol species to the global aerosol extinction optical thickness:Estimates from model results. *J. Geophys. Res.*, **102(D20)**, 23895–23915.

Tibaldi, S. and F. Molteni, 1990: On the operational predictability of blocking. *Tellus*, **42A**, 343–365.

Toth, Z. and E. Kalnay, 1997: Ensemble forecasting at NCEP and the breeding method. *Monthly Weather Rev.*, **125**, 3297–3319.

Vitart, F., 2004: Monthly forecasting at ECMWF. *Monthly Weather Rev.*, **132**, 2761–2779.

Vitart, F., R. Buizza, M. A. Balmaseda, G. Balsamo, J.-R. Bidlot, A. Bonet, M. Fuentes, A. Hofstadler, F. Molteni, and T. N. Palmer, 2008: The new VAREPS-monthly forecasting system: A first step towards seamless prediction. *Q. J. R. Meteorol. Soc.*, **134**, 1789–1799.

Vitart, F. and F. Molteni, 2010: Simulation of the Madden-Julian Oscillation and its teleconnection in the ECMWF forecast system. *Q. J. R. Meteorol. Soc.*, **136**, 842–855.

Wang, W. and N. L. Seaman, 1997: A comparison study of convective parameterization schemes in a mesoscale model. *Mon. Wea. Rev.*, **125**, 252–278.

Wilks, D. S., 2006: *Statistical methods in the atmospheric sciences*, Academic Press.

Woolnough, S. J., F. Vitart, and B. M. A., 2007: The role of the ocean in the Madden-Julian Oscillation: Implications for MJO prediction. *Q. J. R. Meteorol. Soc.*, **133**, 117–128.

Yao, W., H. Lin, and J. Derome, 2011: Submonthly forecasting of winter surface air temperature in North America based on organized tropical convection. *Atmosphere-Ocean*, **49**, 51–60.

Yasunari, T., 1979: Cloudiness fluctuations associated with the Northern Hemisphere summer monsoon. *J. Meteorol. Sci. Jpn.*, **57**, 227–242.

Yu, L., X. Jin, and R. A. Weller, 2008: Multidecade Global Flux Datasets from the Objectively Analyzed Air-sea Fluxes (OAFlux) Project latent and sensible heat fluxes, ocean evaporation, and related surface meteorological variables. *OAFlux Project Technical Report.*

Zampieri, M., P. Malguzzi, and A. Buzzi, 2005: Sensitivity of quantitative precipitation forecasts to boundary layer parameterization: a flash flood case study in the Western Mediterranean. *Natural Hazard Earth System Sci.*, **5**, 603–612.

Zhang, C., 2005: Madden-Julian Oscillation. *Rev. Geophys.*, **43**.